Dynamics of bacterial streamers and impact on biofouling of microfluidic filtration system

by

Ishita Biswas

A thesis submitted in partial fulfillment of the requirements for the degree of

Doctor of Philosophy

Department of Mechanical Engineering

University of Alberta

Abstract

Biofouling refers to the undesirable accumulation and growth of biological substances on a artificial surface with time. Biofilm on the surfaces occurs due to bacterial aggregation and extracellular polymeric substance (EPS) that acts as the construction material of biofilm. EPS consists of long-chain biomolecules such as polysaccharide, protein, and DNA. An interesting phenomenon in the observation that form filamentous bacterial aggregates in continuous flow regime that is called streamer. In this dissertation, two different modes of failure of bacterial streamers have been investigated and quantified in a microfluidic device in a creeping flow regime. In both analyses, the quantification of streamer deformation and failure behavior was performed by using 200 nm fluorescent polystyrene beads, which firmly embed in the EPS and act as tracers. In the first mode of failure, this bacterial streamers, which form soon after the commencement of flow begin to deviate from an apparently quiescent fully formed state in spite of steady background flow and limited mass accretion indicating significant mechanical nonlinearity. This nonlinear behavior shows distinct phases of deformation with mutually different

characteristic times and comes to an end with a distinct localized failure of the streamer. A simplified nonlinear analytical model has been developed to describe the experimentally observed instability phenomena assuming a necking route to instability. The model leads to a power law relation between the critical strain at failure and the fluid velocity scale exhibit excellent qualitative and quantitative agreement with the experimental rupture behavior. The second mode of failure has been investigated and quantified where streamers break due to the growth of voids and cracks in the biomass. This failure occurs in thick bacterial streamers in a microfluidic device with micro-pillars and stands in strong contrast to necking-type instability observed in the thin bacterial streamer. Void/crack growth time-scales could be characterized as short-time scales, and long time-scales and the void/crack propagation showed several instances of fracture-arrest ultimately leading to a catastrophic failure of the entire streamer structure. Amongst the different application domains that bacterial streamers can impact, is the domain of biofouling of membranes. The effect of biofouling in a microfluidic filtration system has been investigated by using a microfluidic filtration device consists of cylindrical microposts with a pore-spacing of 2 µm, thus mimicking a microfiltration membrane system operating in a dead-end mode. The existence

of a critical pressure difference above which pronounced streamer formation was observed, which eventually leads to rapid clogging of the device with an accompanying exponential decrease in permeate flow. Moreover, the de-clogging of pores also occurs intermittently, which leads to small time scale fluctuations ($\mathcal{O}(10^1$ seconds)) superimposed upon the large time-scale ($\mathcal{O}(10^2$ minutes)) clogging of the system. These de-clogging phenomena leads to a sharp increase in water permeation through the membrane, but deteriorates the water quality as biomass debris is transported in the permeate. It has also been observed that the pH of the feed solution strongly affects biofouling of the microfluidic filtration system.

Keywords: Biofouling, biofilm, bacterial streamer, extracellular polymeric substance, creeping flow, microfluidics, membrane mimic, microfluidic membrane, membrane filtration.

Preface

This thesis is the original work by Ishita Biswas. The majority of the context in chapter 1 has been submitted in following book chapter

1. Ishita Biswas, Aloke Kumar & Mohtada Sadrzadeh, Microfluidic membrane filtration system to study biofouling", in the book "Microfluidics and Nanofluidics", Intech open science. ISBN 987-953-51-5997-1 (in press).
   Author Contributions: All authors contributed to the writing of the book chapter.

The majority of the context in Chapter 2, 3, 4 and 5 are published/ submitted in the following journals:

2. Ishita Biswas, Ranajay Ghosh, Mohtada Sadrzadeh & Aloke Kumar, Nonlinear deformation and localized failure of bacterial streamers in creeping flows, Scientific Reports, 2016. 6: p. 32204.
   Author Contributions: Aloke Kumar conceived the experiment. Ishita Biswas and Aloke Kumar designed the experiments. Ishita Biswas conducted the experiments and collected data. Ranajay Ghosh with inputs from Aloke Kumar developed the theoretical model. Ishita Biswas, Ranajay Ghosh and Aloke Kumar analyzed

the data. Mohtada Sadrzadeh played an advisory role. All authors contributed to the writing of the manuscript.

3. Ishita Biswas, Ranajay Ghosh, Mohtada Sadrzadeh & Aloke Kumar, Near wall void growth leads to disintegration of colloidal bacterial streamer, Journal of Colloid and Interface Science, 2018. 522: p. 249-255

   Author Contributions: Aloke Kumar conceived the experiment. Ishita Biswas and Aloke Kumar designed the experiments. Ishita Biswas conducted the experiments and collected data. Ishita Biswas, Ranajay Ghosh and Aloke Kumar analyzed the data. Mohtada Sadrzadeh played an advisory role. All authors contributed to the writing of the manuscript.

4. Ishita Biswas, Mohtada Sadrzadeh & Aloke Kumar, Impact of bacterial streamers on biofouling of microfluidic filtration systems, Biomicrofluidics, 2018 (Under review).

   Author Contributions: Ishita Biswas conceived the experiment. Ishita Biswas, Mohtada Sadrzadeh and Aloke Kumar designed the experiments. Ishita Biswas conducted the experiments and collected data. Ishita Biswas, Mohtada Sadrzadeh and Aloke Kumar analyzed the data. All authors contributed to the writing of the manuscript.

Dedicated to my parents,

Shyamal Kanti Biswas and Mira Prova Biswas

and my niece and nephew,

Pream and Priyak

for their unconditional love and inspiring support

Acknowledgement

I would like to express my deepest respect and gratitude to my supervisors Dr. Mohtada Sadrzadeh and Dr. Aloke Kumar for their guidance, understanding, encouragement and numerous hours spent helping me complete the thesis. They were always available for discussion not only as my research supervisor but also as great life mentors. I am grateful and honoured to be their Ph.D. student. I would like to thank my committee member Dr. Brian Fleck for his continuous support and guidance. I would like to take the opportunity to thank Dr. Subir Bhattacharjee for being my supervisor in fall 2013.

I would like to express my sincere appreciation to Mr. Scott Munro for his help and discussion on my project. I would also like to thank Ms. Josie Nebo and Ms. Mona Pattison for their assistance.

I would like to thank all fellows of Kumar biomicrofluidics group: Dr. Tanushree Ghosh, Dr. Mahtab Hassanpourfard, Dr. Swayamdipta Bhaduri, Behnam Gheshlaghi, Rajorshi Paul and Nandini Debnath. I also express my sincere appreciation to all my friends in AWRL group: Dr. Hadi Nazaripoor, Dr. Behnam Khorshidi, Dr. Parmiss Mojir Shaibani, Dr. Amirreza Sohrabi, Dr. Muhammad Amirul Islam, Ali (Arash) Malekpourkoupaei, Md. Farhad Ismail, Amin Karkooti, Ali Mohammadtabar, Simin Shabani, Babak Soltania, Ayda Razi, Laleh Shmaei, Asad Asad, Farshad Mohammadtabar, Debanik Bhattacharjee, Adham Riad, Nusrat Helali, Zayed Almansoori, Babak Vajdi

Hokmabad, Roohi Shokri, Maryam Mohseni, Md. Omar Reza, Behnam Sadri, Mica Yousuf, Shahab Hajinasiri, and Jannat Fatema , thank you all.

I would like to thank Mr. Haider Alahi, Mrs. Mahmuda Begum, Dr. Shahnawaz Molla, Dr. Niaz Latif and Dr. Bazle Z. (Gama) Haque for their continuous support and guidance all through my Ph.D. study. My appreciation is also extended to Mohammad Ullah, Niema Afroze, Mohammad Abu Hasan Khondoker, Monisha Alam, Nitish Ranjan Sarker, Walid Bin Khaled, Mohib Khan, Md Ashker Ibney Rashid, Abrar Ahmed, Sourayon Chanda, Hafizur Rahman, Shabab Bin Karim and Muhammad Rizwanur Rahman.

I am grateful to my parents, Dr. Shyamal Kanti Biswas and Mira Prova Biswas, my siblings, Dr. Nandita Biswas and Shumiyo Biswas, my cousin, Trishita Biswas, my relatives, my friends, my teachers, for their company, understanding, continuous encouragement and support all the way. Without my family, these accomplishments would not have been possible.

Finally, I appreciate the financial support from the funding agencies that helped me to finish my Ph.D. research.

Contents

List of Tables

List of Figures

Chapter 1 †

Introduction

†The material of this chapter has been accepted as a book chapter, "Ishita Biswas, Aloke Kumar & Mohtada Sadrzadeh, *Microfluidic membrane filtration systems to study biofouling*", in the book "Microfluidics and Nanofluidics", Intech open science. ISBN 987-953-51-5997-1 (in press)

1.1 Biofouling

Biofouling occurs due to the adsorption of the biological cells on a surface [1]. Biological organisms are usually identified by their length scale. Microorganisms, which lie within microscopic length scales (1∼200 µm), include bacteria, fungi, and algae. Furthermore, organisms, whose length scale $>$ 200 µm, are referred to macro-organisms such as larvae, barnacles, hydroids, tubeworms, mussels, and bivalves [2]. They are prevalent in industrial and shipping environment, causing significant problems related to environmental impacts and health risks [3].

1.1.1 Bacterial communities and biofilm

Bacteria are common biofouling agents and are found extensively in nature. Bacteria are microscopic organisms that have a very rich lifestyle. They can live in a free-floating (planktonic) state or in a colony forms such as biofilms or flocs [4]. Bacterial fouling of a surface result from the development of a colony on an artificial surface and these colonies are known as biofilms [5]. Biofilm formation is an extremely complex process and usually several processes, which span a large range of length and time scales. Biofilms are typically extremely heterogeneous and are strongly viscoelastic thus exhibiting an interesting variety of responses to external forces (e.g. shear forces) [5, 6]. Several processes partake in biofilm formation. Biofilm formation typically is initiated by planktonic cells that are exposed to an interface (usually solid-liquid). After these initial attachment events, bacteria start secreting extra-cellular polymeric substances (EPS), which encases the biofilm. It is this matrix

encapsulated, surface associated bacteria communities that are referred to as biofilms [4, 7]. EPS, the binding material of biofilms, is composed of long-chain biomolecules such as polysaccharides, nucleic acids, protein, DNA and lipids. From the microbiology point of view cell to cell communication, quorum sensing, can affect the biofilm formation [5]. Our interest here is to investigate the effect of physical influences, specifically hydrodynamics, in the context of biofilm formation. It is also known that hydrodynamics can influence cell behaviour including quorum sensing.

1.1.2 Mechanical properties of biofilm

Biofilms are excellent examples of viscoelastic active colloids. As such, the response of biofilms to external forces is not a memory-less process. The viscoelastic response of biofilms is usually quantified using rheology. Several researchers have measured the rheological properties of biofilms. Shaw et al. [8] found out that many biofilms can differ in their elastic or storage modulus (G') and loss modulus (G'') values, but they have relaxation times (λ) that are approximately the same in all cases $\lambda \approx 18$ min. The viscosity (η) of biofilms is an important property that directly influences the nutrient supply [9] into the biofilms and ionic strength [10]. Table 1.1 shows the mechanical properties of different biofilms.

Table 1.1: Viscoelastic properties of different biofilms

Strain of bacteria	**Viscosity, η (Pa-s)**	**Elastic modulus G' (Pa)**	**Loss modulus G'' (Pa)**	**References**
P. aeruginosa	8.0×10^3	64.67 ± 21.03	–	[11]
S. aureus 815CT	$(1.9 \pm 1.2) \times 10^5$	$(1.5 \pm 1.1) \times 10^2$	(1.1 ± 9.9)	[12]
S. epidermidis ATCC 35984	$(46 \pm 5.0) \times 10^3$	$(4.5 \pm 4.4) \times 10^2$	(25 ± 23)	[12]
Streptococcus mutans	$256 - 2140$	$(0.73 - 8.56) \times 10^3$	$(5.03 - 10.4) \times 10^3$	[13]
Proteus mirabilis	50000	$900 - 1000$	$125 - 130$	[14]
P. aeruginosa	$(3.6 \pm 2.6) \times 10^5$	$1 - 280$	–	[15]

1.1.3 Biofouling in membranes

Membrane processes can be used to filter a wide range of small materials, ranging from ions and dissolved organic matter to biological substances. They have become very popular for desalination and industrial waste water treatment. However, they face the problem of fouling on a continuous basis. Fouling is the unwanted accumulation of substances on the membrane surface. There are five types of fouling including: scaling (by divalent ions), heavy metal fouling, organic fouling, colloidal fouling, and biofouling [2, 16] (Fig. 1.1).

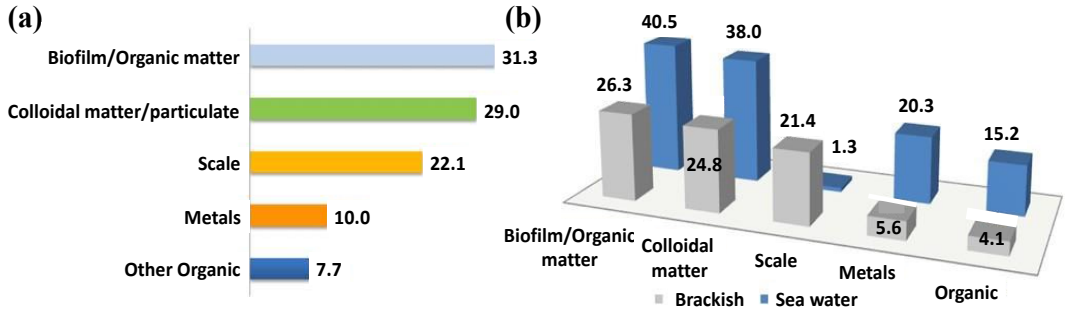

Figure 1.1: (a, b) Main fouling components in percentage on the membrane. Figures are reproduced from Ref. [16] with permission.

Among these fouling types, biofouling is the most severe since it is a dynamic process with at least 45% contribution [2]. Biofouling due to biofilm and colloidal matters act as the main components of membrane fouling [16]. Moreover, biofilms have a significant impact on the membranes used for different types of water filtration such as brackish and seawater. Once a cell is attached to the membrane surface, it decreases membrane permeability by forming a gel layer [17]. Biological substances always remain in the membrane. Even if pre-treatment removes 99.9% of these materials, the remaining 0.1% can grow exponentially by using the biodegradable substances in the feed (waste) water [18].

1.1.3.1 Adhesion of bacteria

Many biological substances can cause the biofouling on the membrane. Among all the substances, biofouling due to bacteria is the focus of this thesis, because of its pervasive nature. Literature suggests that the bacterial swimming motility increases the cell deposition on the surface [19]. Hydrophobic cells have

good adhesion capacity to the negatively charged surface as compared to the hydrophilic cells [20]. The properties of the aqueous solution where the bacteria are suspended also can influence the adhesion to the porous membrane. The bacterial collision efficiency decreases with the decrease of ionic strength and pH that are insufficient for cell attachment [21]. Biofouling due to bacteria retention on membrane surface also depends on solution chemistry, membrane pore structure and system hydrodynamics [22].

1.1.3.2 Biofilm formation

Biofilm formation is one of the most challenging issues in membrane technology [23-25]. The adsorption of bacteria cells on the membrane surface depends on membrane properties such as membrane materials, hydrophobicity, and roughness [26]. The adhesive nature of EPS is considered as the most severe problem in membrane biofouling [27, 28]. Biofilm on the membrane surface reduces the permeate flux and salt rejection [29-31]. In membrane technology, the permeate flux and salt rejection are the two primary criteria for characterizing of polymeric membrane performance. The membrane performs better when the flux and salt rejection are higher. The volume flux (J) of porous membrane is usually calculated by Hagen–Poiseuille equation where the pores are assumed to have the same radius,

$$J = \frac{\varepsilon r^2}{8\eta\tau}\frac{\Delta P}{\Delta x} \tag{1.1}$$

Where Δx is the membrane thickness, ΔP is pressure difference across the membrane, η is the viscosity, τ is tortuosity r is the radius of the pore and ε is the porosity of the membrane. Porosity can be calculated by,

$$\varepsilon = \frac{n_P \pi r^2}{A_m} \tag{1.2}$$

Where A_m is the area of membrane pore and n_P is the number of pores. Tortuosity is defined by:

$$\tau = \frac{(2-\varepsilon)^2}{\varepsilon} \tag{1.3}$$

Matin et al.[32] provided a list of some typical bacteria species that can cause biofilm formation on the membrane surface as well as a reduction in flux decline and salt rejection due to the formation of biofilm on the membranesurface. They observed that without bacterial adhesion, the membrane can reject (R) 98.2% salt. Fig 1.2 shows the reduction of flux and rejection because of the biofouling on the membrane.

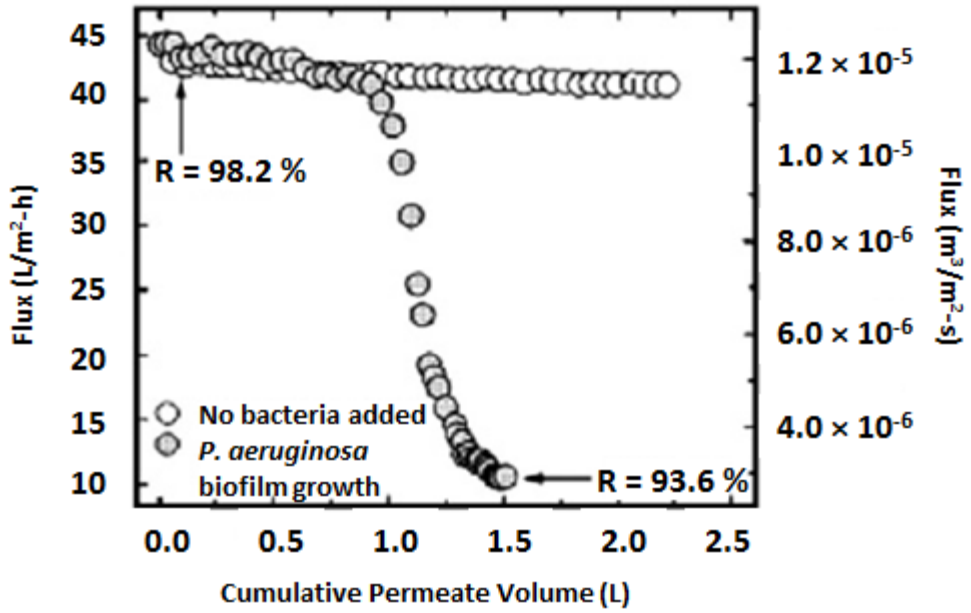

Figure 1.2 The flux and salt rejection due to biofilm on the membrane surface. R represent the rejection When there was no bacteria the flux was almost constant, 43 L/m^{2}h or 1.1 $\times 10^{-5}$m^3/m^2-s. The flux and rejection (R) decrease from 43 L/m^{2}h to 10 L/m^{2}h (1.1 $\times 10^{-5}$m^3/m^2-s to 2 $\times 10^{-5}$ m^3/m^2-s) and by 4.6% respectively with the growth of *P. aeruginosa* biofilm on the membrane surface. The figure is reproduced Ref [32] with permission.

1.1.3.3 Microfluidic approach

In wastewater treatment, microfiltration membranes with the pore sizes lying between 0.1 and 10 µm are used to remove bacteria. Membranes are usually part of an opaque setup, where only the input and the output can be measured. Advancements in micro/ nano technologies, e.g., microfluidic devices can be employed to study membrane processes at the pore-scale. An example of this is the use of microfluidic-based membrane mimics, which are being used to explore a wide variety of membrane related issues, including biofouling. An

essential advantage of microfluidic porous membrane mimics in studying biofouling is that they make real-time microscopy of biofouling possible. Figure 1.3 shows a fundamental schematic difference between membrane filtration mode and microfluidic approach. The pillars are shown in Fig. 1.3b are solid in structures and usually made of PDMS (polydimethylsiloxane). These structures can be altered as per requirement. The gap between the pillars is considered as the pore. The coverslip is used to seal the device. Design and fabrication are the initial steps to work with microfluidic devices. Different types of fabrication techniques include photolithography, electron lithography, hot embossing and injection moulding. Photolithography is a standard technique when feature sizes larger than 1 µm are desired. The nanoscale feature can also be fabricated by e-beam lithography where the minimum resolution could go down to 10 nm [33, 34].

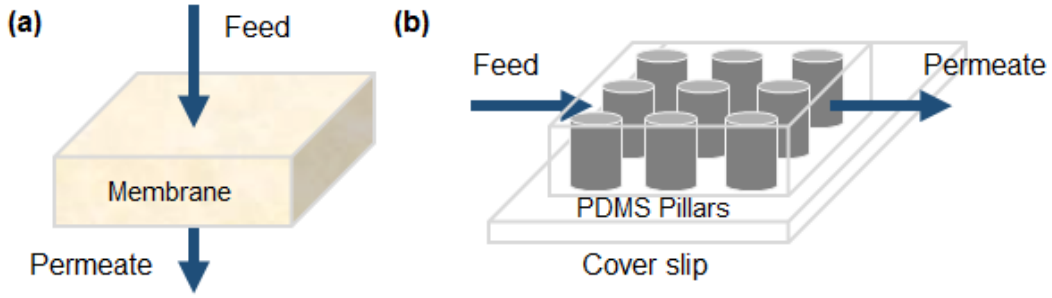

Figure 1.3: Schematics of (a) membrane filtration where feed is wastewater and permeate is the clean water and (b) microfluidic filtration mode

1.2 Bacterial streamer due to biofouling

The impact of hydrodynamic flow on biofilms is the large time-dependent deformations that can result in non-linear phenomena. An example of such phenomena is the bacterial streamer. Streamers form in flowing water and attach to the surface by the upstream "head" while the downstream “tail” can oscillate [35-37]. Streamers in a microfluidic system are typically tethered at one end to the pillar walls while the rest of the body is suspended in the downstream direction. Their filamentous structure can extend significantly with the flow [37-39]. Drescher et al. [40] revealed that streamers can cause a sudden and rapid clog in the fluid flow system in comparison with the biofilm attached to the surface. Surface hugging biofilms have a very modest effect on the flow rate whereas; streamers can drastically decrease the flow rate in a concise period [35]

Rusconi et al. [41] reported streamer formation in the microfluidic channel under laminar flow conditions. They observed formation of a single streamer in the middle of the channel connecting the inner corners of the channel. They also claimed that secondary flows in the curved edge of the channel were responsible for the location of the streamer, which was located at the mid-plane. They further investigated the streamer formation behaviour by changing the radius of the curvature of a zigzag microchannel and discovered that streamer formation depends on the geometric angle of microchannel [42]. A different mechanism of streamer formation called “sudden partial detachment” has been reported, which occurs due to biofilm thickening (increased viscosity) [43].

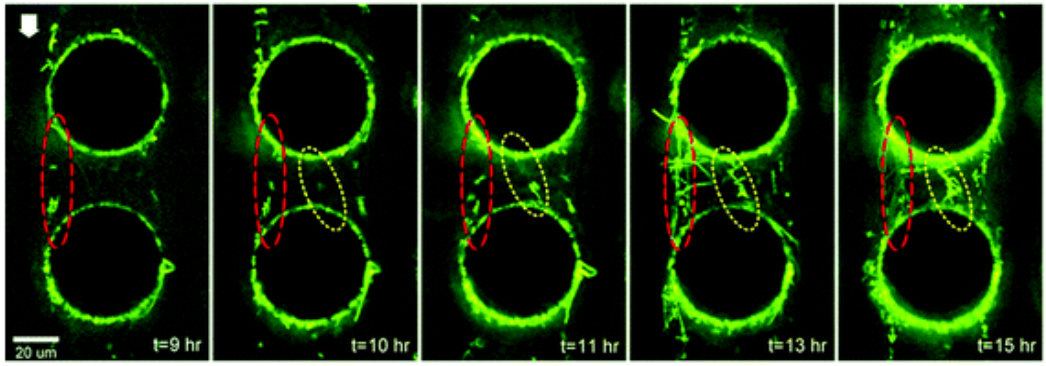

Figure 1.4: Streamer formation in a microfluidic channel. The white arrow indicates the flow direction, and the red and yellow ellipses show the formed streamers attached between two pillars. The green portion only represents the bacteria cells and the EPS appears black. Figures are reproduced from Ref [37] with permission.

Valiei et al.[37] observed streamers through the height of the channel with 50×8 array of micropillars and mentioned it as a 'web' of the streamers. They claimed that flow rate has a significant impact on the number of streamer formation. A large number of streamers formation was reported in the middle of channel height by using confocal microscopy images. Figure 1.4 shows the formation of bacterial streamers in a microfluidic device. As can be seen, the thickness of the streamers increased with the increase of time of the streamer. Fluorescence microscopy was used to capture the image where only bacteria cells are visible (green). The fluid media and the EPS appear dark. Marty et al.[38, 39] studied the effect of different pore sizes and filtration modes on the lengths of streamers that formed in a membrane mimic system. They fabricated a microfluidic device with 25 straight, interconnected and staggered PDMS pillars to observe the nature of biofouling in a membrane mimic. The width and height of pillars were 10 µm and 50 µm respectively, and the membrane mimic pore size was 10 µm or larger. The gap between the pillars in the

membrane mimic system was considered as the pore of the membrane mimic. They found that presence of tortuosity promotes the streamer formation in the microchannel.

1.3 Microfluidic filtration system

1.3.1. Basic overview of fabrication technique

1.3.1.1 Membrane fabrication

Membrane process is an emerging separation technology. The membrane itself is the heart of a membrane process. Membranes can be classified as polymeric and inorganic, porous and dense, isotropic and anisotropic, hydrophilic and hydrophobic. Figure 1.5 gives an overview of types and preparation process of the polymeric membranes. Phase inversion (phase separation) and track etching are the most widely used techniques for the preparation of porous membranes [44].

In phase inversion process method, the polymer is transformed in a controlled manner from liquid to solid state [44, 45]. Symmetric porous phase inversion membranes (uniform porosity) are made by using water vapor as the coagulant. For making asymmetric membranes (a thin layer of lower porosity over a symmetric membrane) by phase inversion temperature increase and a liquid nonsolvent is used to precipitate the polymer (Figure 1.5). In track etching method, a high energy particle is applied to the polymeric film, to

damage the polymeric matrix and create tracks. By etching, the polymeric material along the track uniform cylindrical pores can be obtained.

Dense membranes (symmetric and asymmetric) are mainly synthesized by solution casting and interfacial polymerization of two monomers on a substrate. A detailed explanation of membrane preparation techniques is available in the literature [44]. A summary of different types of pressure-driven membrane processes with their fabrication technique, separation principle, pore morphology, pressure and flux ranges are given in the Table 1.1. Scanning electron microscopy (SEM) images of different types of membranes are presented in Figure 1.6.

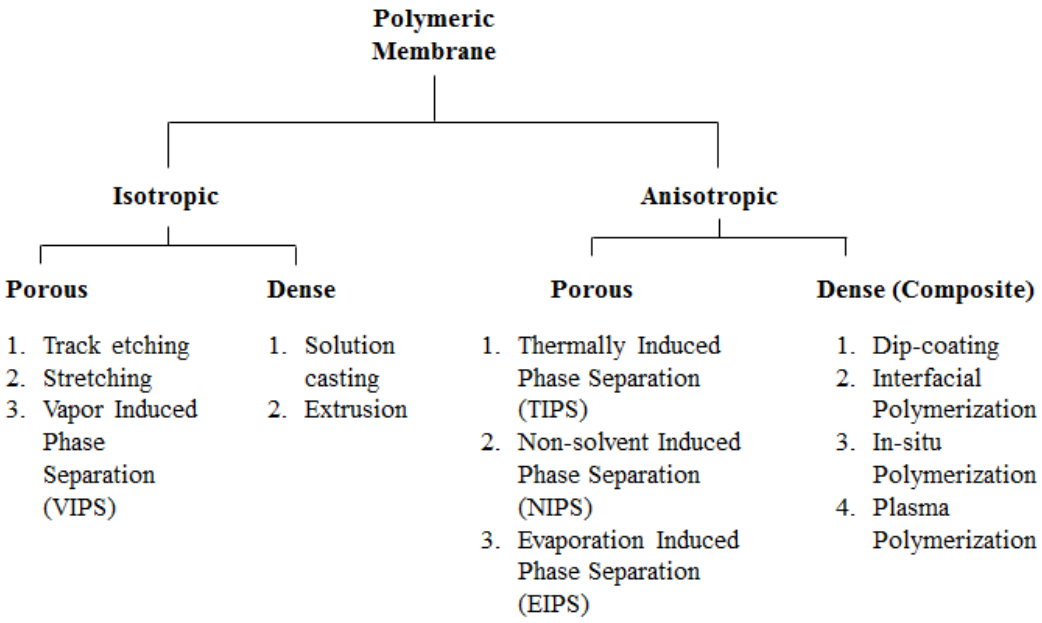

Figure 1.5: Preparation methods of polymeric membrane

Table 1.2: Summary of different types of pressure-driven membrane processes [44-47]

Membrane Process	**Polymer used in the Fabrication Process**	**Fabrication Technique**	**Pore size**	**Pressure Range (bar)**	**Flux range ($l.m^{-2}.h^{-1}.bar^{-1}$)**	**Application**
Microfiltration (MF)	Polyvinylidene fluoride (PVDF), Poly (tetraflurethylene) (PTFE), Polypropylene (PP), Polyethylene (PE), Polyethersulfone (PES)	Phase inversion Stretching, Track-etching	Porous: 10^{-1} – 10 µm	0.1 – 2.0	>50	Separation of macromolecular to cellular size particles (Bacteria/ fat and some proteins)
Ultrafiltration (UF)	Polyacrylonitrile (PAN), Polysulfone (PS), Poly (phthazine ether sulfone ketone) (PPESK), Poly (vinyl butyral), PVDF, PES	Phase Inversion, Solution wet-spinning	Porous: 10^{-2} – 10^{-1} µm	1.0 – 5.0	10 – 50	Separation of molecular to macromolecular size particles (all proteins)
Nanofiltration (NF)	Polyamides, Polysulfones, Polyols, Polyphenols	Interfacial polymerization, Layer-by-layer deposition, Phase inversion	Porous: 10^{-3} – 10^{-2} µm	5.0 – 20	1.4 – 12	Separation of Ionic molecular size particles (Lactose)
Reverse Osmosis (RO)	Cellulose acetate/ triacetate, Aromatic polyamide, Polypiperzine, Polybenziimidazoline	Phase inversion, Solution casting	Dense/ Porous: 10^{-4} – 10^{-3} µm	10 – 100	0.05 – 1.4	Separation of ions (all minerals)

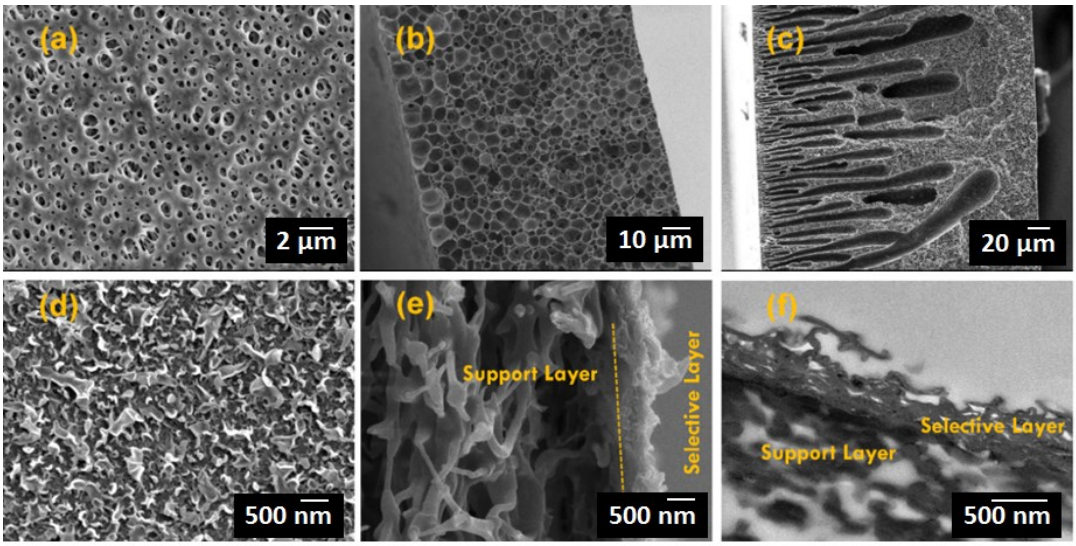

Figure 1.6: Surface SEM image of (a) a phase inversion porous membrane, (b) cross-sectional SEM image of an isotropic phase inversion membrane, (c) cross-sectional SEM image of an anisotropic phase inversion membrane, (d) surface SEM image of thin film composite (TFC) dense membranes, (e) cross-sectional SEM image of a TFC membrane, and (f) cross-sectional SEM image of a TFC membrane.

1.3.1.2 Microfluidic mold and device fabrication

There are many types of fabrication techniques available for making micro and/or nanodevices such as photolithography, etching, soft lithography, hot embossing, injection molding, e-beam lithography, and micro-stereolithography. Photolithography and etching are two popular fabrication techniques for making the microfluidic moulid. Soft lithography technique was used to make PDMS microfluidic system with 20 – 100 µm structure [48]. This technique has also worked well on hydrogel polymers (calcium alginate) to fabricate microfluidic network of 100 µm wide and 200 µm deep and 25µm ×

25µm cross-section [49]. The fabrication of 500 to 2000 µm diameters and 200 to 1000 µm height cylindrical columns [50] is possible by hot embossing technique. Smaller range of feature sizes can also be achievable by hot embossing and partial embossing [51, 52]. A schematic diagram of a microfluidic device is shown in Figure 1.7. This device is used to observe the biofilm behavior and the change of hydrodynamics of the fluid flow through the channel [37]. The chip has one inlet and one outlet and is made by traditional photolithography using PDMS.

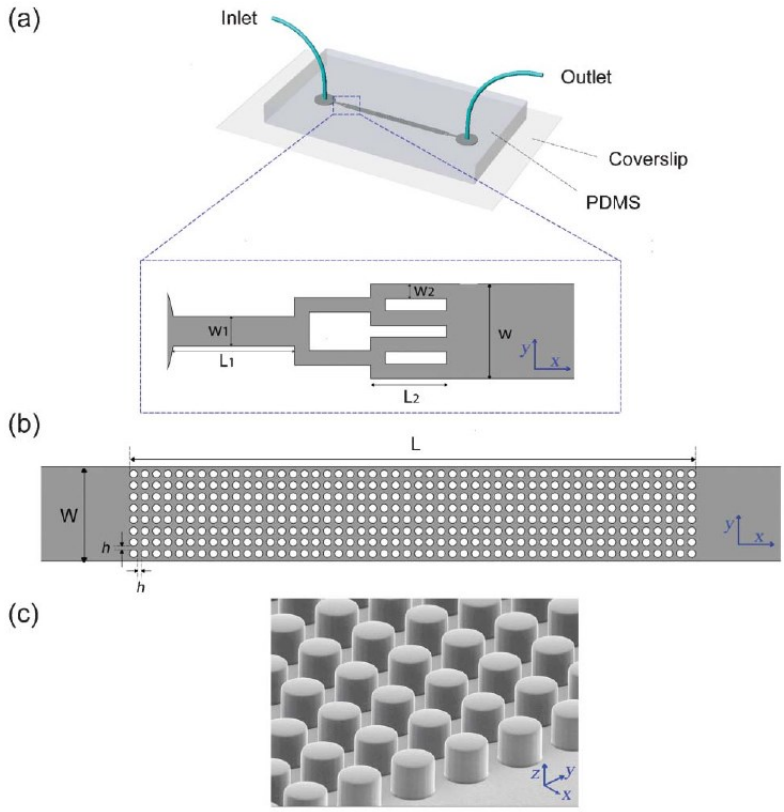

Figure 1.7: (a) Schematic microfluidic chip, (b) porous media, and (c) SEM image of micropillars of the equal diameter of 50 µm. Figures are reproduced from Ref. [37] with permission.

1.3.2. Membranes in microfluidic devices

1.3.2.1 Direct incorporation of membranes into microfluidic devices

Membrane can be incorporated into the microfluidic devices directly. The membrane can be fabricated as per the requirement by following the traditional membrane fabrication techniques described above (section 1. 3. 1 .1) and then bonded to the microfluidic chip. Russo et al. [53] directly incorporated polymeric membrane into silicon-based lab-on-chip device. Silicon substrate coated with a thin nitride film was used to serve as a support structure for the track-etched membrane. Patterning was conducted by UV exposure through chrome glass mask and CF_4 reactive ion etching to transfer the pattern to the nitride layer. The process was repeated on the other side of the wafer by using the second mask with pores on it. The membrane was finally incorporated into the PDMS device. The membrane can be placed between two microfluidic chips and make a sandwiched structure. This is also another way of using a membrane directly in the microfluidic devices. By using this technique, a three-dimensional microfluidic network was designed by Ismagilov et al. [54] investigated the interactions of chemical and biochemical reagents. They used a polycarbonate membrane between two PDMS microfluidic devices to make the sandwiched structure.

Membrane integrated with microfluidic device plays an essential role in the medical application [55-58]. Srigunapalan et al. [55] made a microfluidic device with membrane to mimic the Endothelium cells of the vascular

microenvironment to study the drug and macromolecular permeability and other proteins through the system. The device was used to study the important phenomena of the Endothelium cells. To study the complex phenomena inside the vascular system different types of membrane with the microfluidic devices are used. A microfluidic device was fabricated by sandwiching polyester membrane between microfluidic chips and used to study the interaction of cancer cells with a vascular endothelium and to prevent the metastatic disease [56]. A membrane with microfluidic device was also used to demonstrate the lungs injury [57] by toxic substances [58]. Huh et al. made a microfluidic airway system with an approximate diameter of respiratory bronchioles (narrowest airways of the lungs) to explore the cellular-level lung injury [57]. To make a sandwich structure of a membrane in a microfluidic device, bonding of the membrane and the device is a critical issue to deal with the leakage. PDMS mortar film, which is made by mixing PDMS and toluene, can be used to make the bond [59] effectively. Young et al. [60] fabricated such kind of devices to measure the biomolecule permeability across the porous membrane. PDMS prepolymer was cured, and 3 mm diameter holes were punched through the cured PDMS. PDMS mortar layer was then generated on a glass support, and the PDMS substrate was placed on the support so that the holes were not in contact with the mortar layer. On the other side, the membrane was pressed down into the mortar layer. Finally, the membrane was placed between two substrates and bonded with PDMS mortar layer. Using an additional PDMS separator with the membrane can be another way to prevent the leakage [61].

1.3.2.2 Membrane fabrication as a part of the microfluidic device fabrication

The membrane can be fabricated as a part of a microfabrication process instead of using the traditional membrane fabrication technique. Karnik et al. fabricated a composite membrane of copper, aluminum, spin-on-glass (SOG), and palladium for the water gas shift reaction experiment [62]. Silicon nitride was deposited on both sides of silicon wafers by chemical vapor deposition process. A thin layer of aluminum acted as an adhesive layer of the palladium. Photolithography and wet etching were used to pattern holes on the copper-aluminum layer and to obtain a microchannel. Ookawara et al.[63] fabricated a microchannel as a microseparator for oil and water separation. They made 10 mm curved radius and 112 microns width slits on 80 microns thick SUB308 plates by photolithography. A stack was made by putting the plates with and without slits in turn and diffusion bonded to make microchannel feature. Heyderman et al. [33] fabricated nanopore membrane chip by combining the techniques of hot embossing and photolithography (Figure 1.8). Silicon (Si) master mold with nanopore arrays was fabricated by using electron beam lithography, and the pores were replicated on PMMA by a hot embossing technique. Various etching processes were used to transfer the pores on Si_3N_4 to fabricate the final nanopore membrane. Though they used PMMA resist with chromium, Si, and silicon nitride (Si_3N_4), the final membrane they obtained was made of Si_3N_4. The pores diameter varied from 100 nm – 450 nm of Si_3N_4 nanopore membrane. To analyze and separate the biological cell Dong et al. fabricated micromachined separator with soft magnetic micro-pillar

arrays that could act as a membrane to observe the performance of the cell separation [64]. A membrane with embedded channel was used to study the hydrodynamic behavior and the fouling formation on the membrane during filtration of synthetic wastewater made of polystyrene particle [65]. They used square-shaped silica capillaries to template the membrane. Polyvinylpyrrolidone (PVP) and N-methylpyrrolidone (NMP) were used as polymer and solvent for membrane preparation, respectively. The silica capillaries were glued to a glass plate and the polymer solution was cast on the glass plate at room temperature. The structured membrane was then kept in a vapor bath and tap water bath for coagulation and phase separation. After making the final structured membrane, the silica capillary is placed in the channel of the membrane. The membrane was then placed between two lamination sheets to seal the chip.

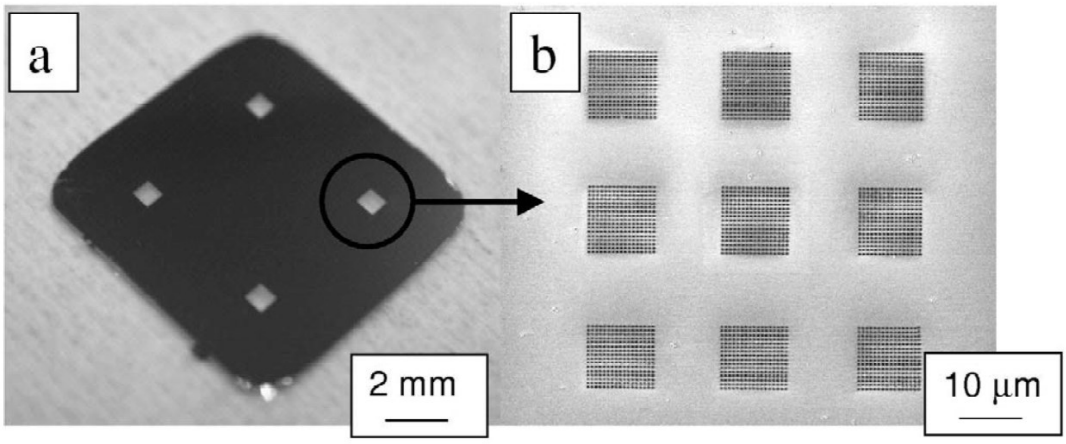

Figure 1.8: (a) Membrane chip with four membranes (10×10 mm^2), and (b) nanopore array (10×10 µm). Figures are taken from the Ref. [33] with permission.

1.3.2.3 Microfluidic membrane mimic

The microfluidic membrane mimic can be defined as a part of the device with pillars or curvature or any designed structured and the tiny gap between the structures that serve as a porous membrane. The design of the microseparator can be changed to mimic the different pore sizes and shapes for the membrane study in a microfluidic device. For instance, Hassanpourfard et al. [66] designed and developed a detailed fabrication protocol for making microfluidic device that mimics the porous media to study the biofilm formation. Bacchin et al.[67] used different shapes of PDMS microseparator to ensure the uniform flow of the suspension over the width of the filtering part and to study the fouling. Derekx et al. [68] investigated the fouling behavior in a PDMS microfluidic mimic membrane by the experiment and computer simulation. The research on microfluidic membrane mimic has been mainly focused on fouling phenomena in porous media. For instance, Marty et al. [39] fabricated microfluidic devices with straight, interconnected and staggered channels to observe the biofouling nature in the microfluidic device due to biofilm. Figure 1.9 shows the schematic of their microfluidic device with the mimic membrane structure. Transparent PDMS microsystem is used to mimic the membrane to study the bacteria transfer in the porous interface. The filtering part of the PDMS microseparator has a parallel arrangement of 25 microchannels. The width of the microchannels is 10 µm and the length is 200 µm or 170 µm. In z-direction, the depth is 50 µm. They studied the effect of different pore-sizes and dead-end and pseudo cross-flow filtration modes on the biofouling during filtration.

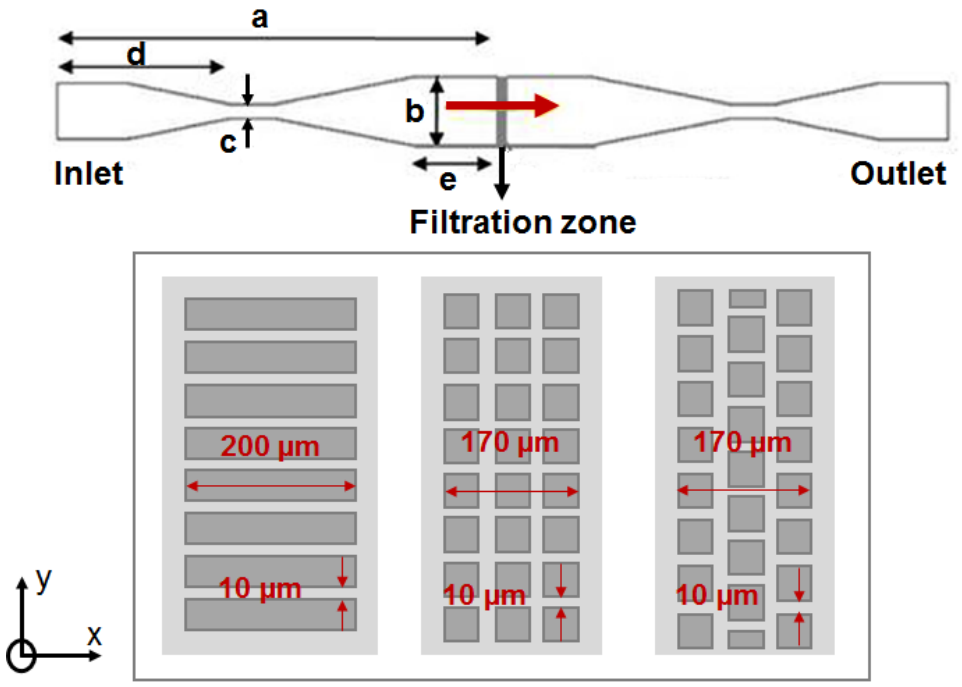

	a	b	c	d	e
Size (µm)	12900	1700	500	5000	4000

Figure 1.9: Microseparator system with dimensions for the mimic membrane. Figures are reproduced from Ref. [39] with permission.

In subsequent work, they also reported that pore tortuosity and secondary flows have a significant impact on biofouling formation in the mimic system [38]. In the pseudo filtration mode, they did not work on the effect of pressure difference on the biofouling formation during filtration. Table 1.2 shows a summary of different microfluidic membrane fabrication techniques with pore information and their application.

Table 1.3: Summary of different types of microfluidic membrane device fabrication

Different materials and Polymers used in the Fabrication Process	**Membrane pore size**	**Fabrication technique of membrane**	**Incorporate membrane in microfluidic device**	**Different types of Applications**
Cellulose acetate[53]	MWCO: 350 Da[53]	Casting	Direct casting & sandwich the membrane in between the microfluidic devices	1. Biological analysis 2. Investigate chemical or biochemical interaction 3. Medical Application 4. Fouling characterization
Polyetherimide (PEI), Polyvinylpyrrolidone (PVP), & N-methylpyrrolidone (NMP)[65]	3 - 8µm[65]			
Polycarbonate[54, 69]	0.1-1 µm vertical pore, 10 µm thick[54]	Commercial membrane		
Polyester[56, 57, 69]	400 nm[56, 57], 10 µm thick & 3 µm & 20 µm pore[69]			
Polyamide[61]	RO: MWCO: 200DA[61]			
Polyethylene terephthalate (PET)[55]	8µm[55]	Track etching		
Cyclopore polycarbonate regular & thin clear, Nuclepore polycarbonate[60]	1 µm[60]			

PDMS[58]	10 µm thick & 10 µm effective diameter[58]	Soft lithography		
copper, aluminum & palladium[62]	60nm, 200 nm & 500 nm[62]	Composite membrane & MEMS fabrication	Membrane fabrication as a part of microfluidics device fabrication	1. Oil-water separator 2. Magnetic micro separator 3. Fouling analysis 4. Biofouling Study
PMMA, Si_3N_4, Si, Si_3N_4 & Cr[33]*	Micro-slit, 112 µm[33]	Hot embossing & photolithography		
SUS304 Plate[63]	500nm, 330 nm, 140 nm[63]			
PDMS [38, 39, 67]	width: 10 µm, Length: 200 µm or 170 µm & Depth: 50 µm[38, 39], Constriction: 20 µm smallest width: 50 µm[67]	Soft lithography		
Cellulose ester[68]	5 µm[68]	Commercial membrane		

*Final membrane was produced in Si_3N_4

1.4 Research objective

Biofouling due to bacterial colonization on the membrane surface is the most severe fouling among all fouling phenomena. Bacterial streamer due to biofouling makes it more complicated because of its dynamic behaviour and viscoelastic nature. Hence, it is imperative to observe the real-time phenomenon that is occurring during biofouling process. Microfluidic devices have therefore become essential tools to study the bacterial growth and its post formation dynamics in a flow regime. Integrating membranes with microfluidic devices has become very popular over the past decade.

Concerning bacterial streamers unanswered questions are: (a) Are the streamers static structures or do they display time-dependent behaviour such as failure? (b) Do parameters like flow rate, pH, pressure, and geometry of the device play a crucial role in streamer formation dynamics? (c) How the streamer formation dynamics can be correlated to the membrane performance? The objectives of this work are:

1. To design microfluidic experimental set-up(s) to observe and understand the bacterial biofouling behaviour in a microfluidic membrane mimic subjected to a continuous flow. These mimics will be used to study time-dependent bacterial streamers, post-formation behaviour, and its relationship to hydrodynamics.
2. To conduct systematic studies on effect of influential parameters including pressure gradient and pH on the failure of streamers.

1.5 Thesis structure

The present dissertation is organized in a paper-based format. Chapter 1 is written based on a submitted book chapter. Chapters 3-5 are written based on submitted/published journal articles. Chapter 2 provides the material and methods that have been used in the Chapter 3, 4 and 5. This chapter contains the protocol of making microfluidic device, preparing biological substance and the design of microfluidic experiments.

Chapter 3 presents the nonlinear deformation of bacterial streamer in creeping flows and an analytical model to describe the experimental observation. This study shows that the instability in bacterial streamers can lead to a creep type deformation and catastrophic failure occurs with time. The failure occurs far from the wall, showing a necking type deformation in a thin bacterial streamer.

Chapter 4 presents the nonlinear deformation and failure through expanding voids in bacterial streamers. This mode of failure stands in contrast to necking type of instability. This breaking consists of two different time scales, short and long. The crack/ void propagation goes through several cycles of propagation and arrest. The failure occurs near the wall in a thick bacterial streamer.

Chapter 5 presents the impact of the breaking/ failure of bacterial streamer in a microfluidic membrane filtration system. The experimental set-up shows a dead-end filtration mode and a microfluidic device is designed to mimic the microfiltration membrane system. A parametric study shows the

effect of pressure difference and pH on the breaking of streams in this type of filtration system.

Chapter 6 summarizes the significant findings of all parts of this research work and provides concluding remarks.

1.6 Thesis contribution

Sustained hydrodynamic flows can elucidate viscoelastic responses from biofilm soft matter and one effect of such responses can be the formation of filamentous bacterial streamers [5]. Streamers contain bacteria cells embedded in the EPS matrix. Unlike biofilms, the slender body of streamer can extend significantly with the flow, are typically tethered at one end to the pore-walls, while the rest of the body is suspended in the downstream direction. Bacterial streamers can clog the closed channel significantly faster than the surface biofilm [70]. The time scale of streamer formation can vary significantly and can have different impact on the post-formation dynamics of streamers in the system [71]. The time-dependent deformation tendency of bacterial streamers in creeping flows (Reynolds number, $Re, << 1$) have remarkable implications for membrane systems [38, 39]. One of the most basic challenges arises during the visualization since the EPS matrix is transparent in nature and very difficult to image. Another challenge comes during material characterization as these streamers form in very small-scale devices accruing small amount of biomass, which is inadequate for ex-situ measurements. Unfortunately, literature on this subject is limited. Thus, a better understanding of deformation and failure of bacterial streamers is crucial in low Reynolds

number conditions from both physical and biological aspects. Due to these reasons, it becomes imperative to visualize bacterial colonization patterns in membrane type systems. Such visualization would significantly aid the understanding of novel phenomena such as streamers.

A microfluidic device has been proposed which by enabling real-time visualization of bacteria cells, biofilms and streamers in these devices allows us to answer the unanswered vital questions mentioned in the research objectives. Two different failure mechanisms of bacterial streamers have been identified. The first type of deformation and failure of bacterial streamer followed a "necking" route to instability that occurs far from the wall and in a thin streamer. However, the second type of failure in a thick streamer has been observed due to the crack propagation inside the streamer material, which occurred near the wall. These two different failure mechanisms have been analysed and quantified. These types of dynamic nature of bacterial streamer can have severe impact on biofouling that declines water quality during membrane filtration and clogs the system increasing potential health risk. A microfluidic filtration system that mimics a pressure-driven membrane filtration operates in a dead-end filtration mode has been established. A parametric study i.e., pH, flow rate, and pressure has been conducted, on the dynamic behaviour of the bacterial fouling.

1.7 Author's contribution

In this dissertation, two completely different failure mechanisms of bacterial streamers have been identified and quantified. The author established

a microfluidic filtration system that can mimic microfiltration membrane systems. The author directly contributed in the design and fabrication of microfluidic device and visualization of bacterial streamers' dynamics inside the device by using fluorescence and confocal microscopy, repeatability and parametric experiments that are reported in this thesis. The experimental uncertainty analysis was performed by the author. The author designed the photo mask and performed the photolithography, silicon wafer etching, PDMS casting on silicon mold and SEM imaging of the device by using the NanoFAB facilities at the University of Alberta. The author prepared the bacteria culture for individual experiments and performed the experiments by using the microfluidic device and the bacterial culture. The author performed the observation and tracking of the instabilities of bacterial streamers during experiments. The author identified, quantified and analyzed two instabilities in the bacterial streamer material that were observed during the experiments by using various image analysis softwares such as the NIS element AR software interface, Olympus cellsens software, MathWorks® image processing toolbox (MATLAB R2017a), ImageJ Fiji, ADOBE FIREWORKS CS6 and ADOBE AFTER EFFECTS CC. The theoretical analysis of streamer instability was successfully accomplished with the help of Dr. Ranajay Ghosh. The author would like to thank Scott Munro and Dr. Tanushree Ghosh for their valuable advice during the microfluidic chip fabrication and bacteria culture preparation for this study.

Chapter 2 ※

Materials and Methods

※This chapter is organized based on Chapter 3, 4 and 5

2.1 Design and fabrication of microfluidic membrane mimic device

The design of the microfluidic device was made using commercial L-edit software to mimic membrane type of porous media. The chrome photomask was used to print the final design. There were two types of designs of cylindrical pillars in staggered pattern: 14 pillars with 50 µm height and 17 pillars with 10 µm height. All pillars have 50 µm diameter. The minimum distance between pillars was fixed a either 10 µm and 2 µm. The fabrication procedure is described in the following section. The fabrication protocol is followed given by Hassanpourfard et al. [66]. Figure 2.1 shows the schematic diagram of fabrication process.

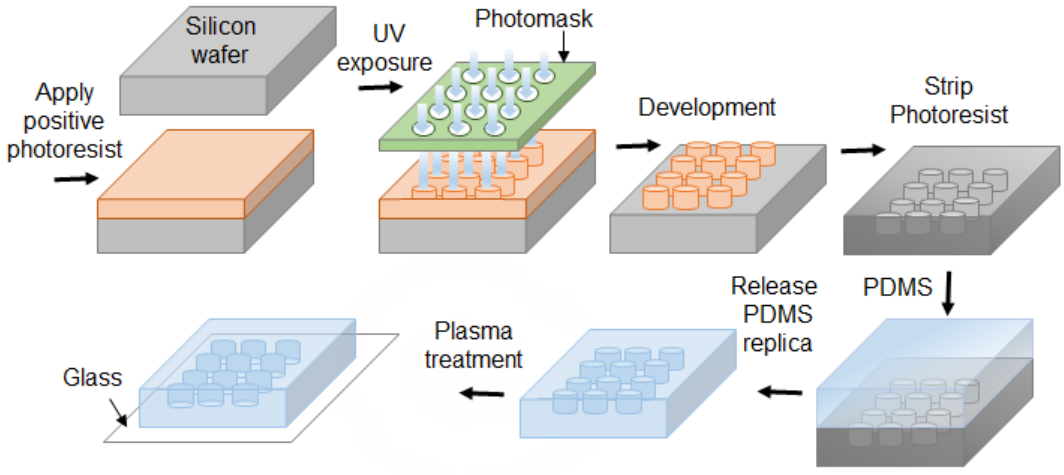

Figure 2.1: Schematic diagram of microfabrication process steps for making microfluidic membrane mimic device

2.1.1 Photolithography

A 4 in. Silicon wafer was cleaned in a piranha solution (H_2SO_4 and H_2O in 3:1 ratio) for 15 minutes. AZ4620 and HPR 504 positive photoresists were used to coat the wafer. 12.5 µL thick photoresist was applied on the silicon wafer by following two steps.

In the first step, spread step, the wafer was spun for 10 second at 500 rpm and in the second step, spun step, it was spun for 25 seconds at 2000 rpm. The wafer was then soft baked on a hot plate with nitrogen flow at 100 ℃ for 90 seconds and kept on vacuum at 100 ℃ for 60 seconds to evaporate the solvent. The wafer was exposed to UV light for 3 seconds to transfer the designed pattern from the photomask to the photoresist. The wafer was then immersed in AZ400K developer to dilute and remove the exposed photoresist. Finally, the wafer was rinsed with isopropyl alcohol and dried.

2.1.2 Deep reactive ion etching

Deep reactive ion etching (DRIE) was performed to get the final depths, 50 µm and 10 µm of the device (channel height in z-direction). The remaining photoresist was removed by using an etcher machine and the final silicon master mold was ready.

2.1.3 PDMS casting and glass bonding

In the casting process, silicon wafer was placed in a desiccator with a few drops of tri-chloro-methyl-silane (TCMS) in a vial. This salinization process was performed to form a monolayer salinization agent that prevented the silicon mold from sticking. PDMS (Polydimethylsiloxane) was prepared by mixing the Sylgard 184 (Dow Corning, NY, USA) and curing agent in a 10:1 ratio by weight. PDMS was degassed and then poured on the wafer. After 2 hours of curing at 80°C the PDMS was cooled down and peeled off from the silicon master mold. The inlet and outlet holes were drilled.

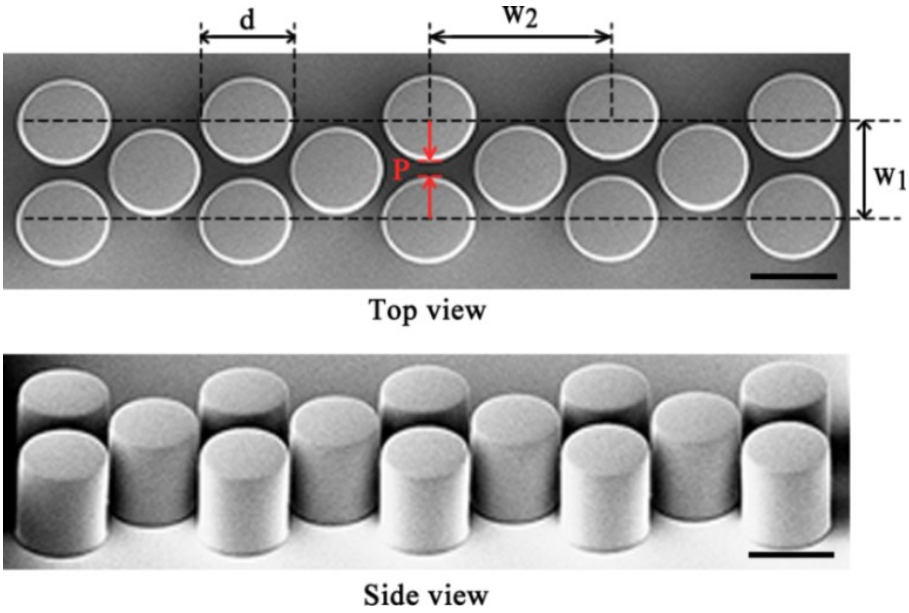

Figure 2.2: SEM image of the micropillars. The geometric dimensions are $d = 50\,\mu m$, $w_1 = 60\,\mu m$, $w_2 = 104\,\mu m$ $P = 10\,\mu m$ and the height of the pillars is $50\,\mu m$ (along z-axis).

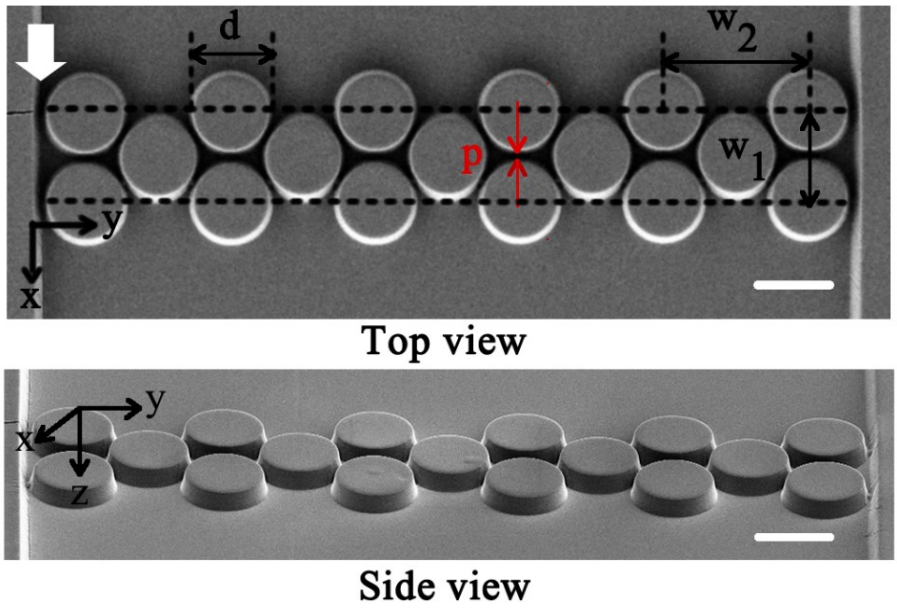

Figure 2.3: FESEM images of another design of the micropillars. The geometric dimensions are: $d = 50\ \mu m$, $w_1 = 52\ \mu m$,$w_2 = 95\ \mu m$, $p = 2\ \mu m$ and, height of the pillars is $10\ \mu m$ (along z-axis).

The PDMS was then bonded to a glass coverslip (thickness 0.13 to 0.17mm) (Fisher Scientific, ON, Canada) by exposing to oxygen plasma for 30 seconds. The device was annealed at 70℃ for 10 minutes to seal the PDMS and glass. The Scanning electron microscopy (SEM) and Field emission scanning electron microscopy (FESEM) images of two different sets of micropillars inside the microfluidic channel are shown in Fig. 2.2 and Fig 2.3 where the heights are 50 µm and 10µm respectively. The flow is along the x-axis as indicated by the arrow. The scale bar is 50 µm. The length of the channel, L, was 11.5 mm and its width, W, was 0.436 mm. In the central section of the channel, 14 to 17 cylindrical micropillars of 50 µm diameter are placed in a staggered pattern at a distance of 6.6 mm from the inlet. PDMS was considered because of its optically transparency, electrically and thermally

insulating, mechanically elastomeric (Young's modulus ~ 750 kPa), low surface free energy ~ 20 erg/ cm^2, impermeability to liquid water, permeability to gas and nonpolar organic solvents, reactivity to oxygen plasma, nontoxic nature and easy to make smooth and nonpolar surface [72]. PDMS has been widely used as a microfluidic membrane material for modelling the transport phenomena at pore scale [38, 39, 67, 73].

2.2 Bacterial solution preparation

2.2.1 LB agar plate preparation

20 grams of Luria – Bertani (LB) agar was mixed with 500 ml DI water in a 1 L conical flask. The flask with the liquid was sterilized by autoclaving for 15 minutes at 121 ℃ and 15 psi. After sterilizing the flask was placed in a biosafety hood and the liquid agar was poured in petri dishes.

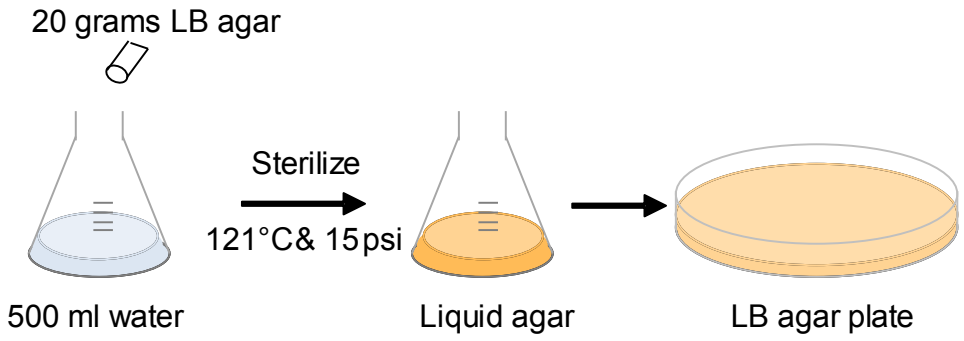

Figure 2.4: Schematic diagram of LB agar plate preparation

Each plates contains approximately 20 ml of liquid agar solution. The plates were then kept in the biosafety hood for 24 hours to cool down at room temperature. Figure 2.4 shows the schematic diagram of LB agar plate preparation.

2.2.2 LB broth preparation

15.5 grams of Luria–Bertani (LB) broth was mixed with 1 L of DI water in a 2 L conical flask. The flask was sterilized by autoclaving at 121 ℃ and 15 psi for 15 minutes. After sterilizing the LB broth was left in the biosafety hood for 24 hours to cool down to room temperature. Figure 2.5 shows the schematic diagram of liquid LB broth preparation.

2.2.3 Bacteria solution preparation

Pseudomonas fluorescens CHA0 (wild type) [74] and *Pseudomonas aeruginosa* MPAO1 (wild type) (P. aeruginosa Mutant Library - University of Washington) bacteria were used. *P. fluorescens* are gram-negative aerobic bacteria can be found in soil and water and play an essential role in plant health [75]. The strain of bacteria is green fluorescent as they express green fluorescent protein (GFP) constitutively. Both strains were taken from a −80 ℃ freezer and streaked at a zigzag pattern on two different LB agar plates in the biosafety hood.

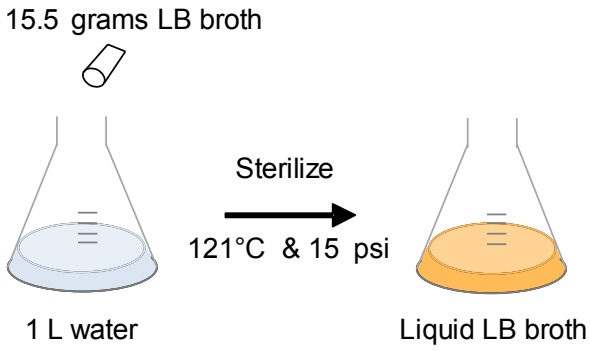

Figure 2.5: Schematic diagram of LB broth preparation

The plates were incubated for 24 hours at 30 ℃ and 37 ℃ for bacteria growing. A single colony was taken from each plates and poured into conical flasks contains 30 ml LB broth. *P. fluorescens* was incubated for 14 to 26 hours in a shaking incubator (Fisher Scientific/ VWR, PA, USA) at 30 ℃ and 100 rpm to 150 rpm. *P. aeruginosa* was incubated for 2.5 to 6 hours in shaking incubator at 37 ℃ and 100 rpm to 150 rpm.

2.2.3.1 pH control

All the bacteria culture were prepared at pH = 7 condition. 5 ml of this bacterial culture (pH = 7) was mixed with 5 ml LB broth (pH = 3 to 12) so that the pH of the solution lay between 5 and 10 (pH was measured by using pH paper strips). The optical density at 600 nm (OD_{600}) was measured by with a Spectrophotometer (Novaspec II, MA, USA). Figure 2.6 shows the schematic diagram of the procedure of bacteria culture preparation.

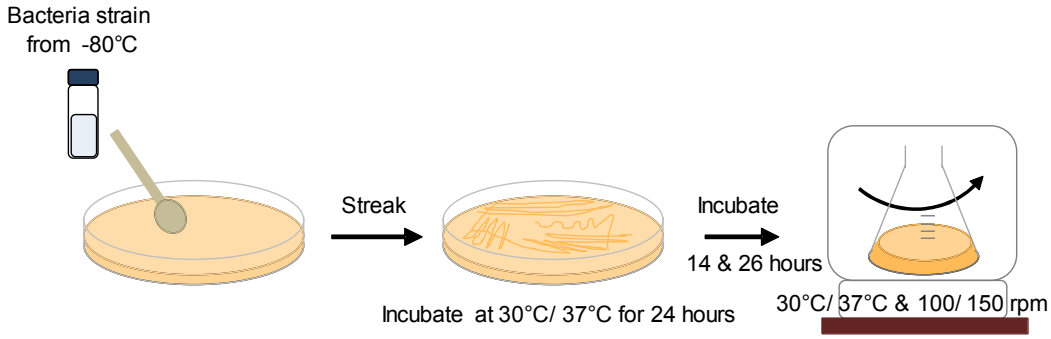

Figure 2.6: Schematic diagram of the preparation of Bacteria solution

2.2.3.2 *Bacterial floc measurement*

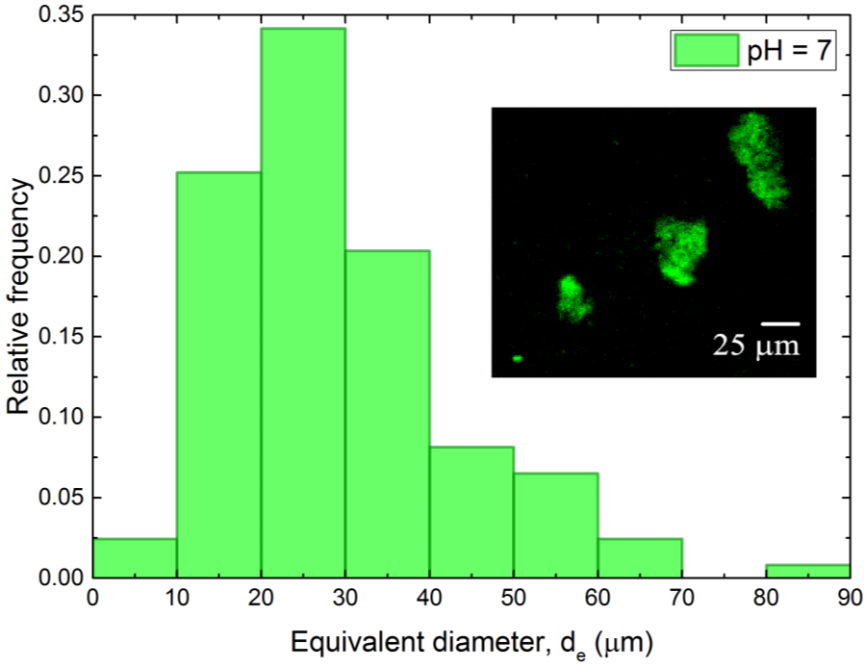

Figure 2.7: The relative frequency histogram of the *P. fluorescens* bacterial flocs at pH = 7. The total number of flocs imaged were 123 and the median of the equivalent diameters (d_e) of flocs is 26 µm. The inset image shows typical flocs.

The incubation time-period was carefully chosen so that flocculation of the bacteria occurred during this period. Longer incubation time was employed so that bacterial flocs formed. Flocs consist of bacteria encased in EPS and are considered an aggregative form of bacterial growth. For imaging of bacterial flocs in quiescent conditions, the bacterial solution was poured into an imaging chamber (Lab-Tek® chambers, Fisher Scientific, ON, Canada), which was then placed on an inverted optical microscope (Nikon Eclipse Ti). Fluorescence imaging was performed with a GFP Long-pass green filter cube. The equivalent diameter (d_e) of flocs was measured through image processing by using the NIS-Element AR software interface (Nikon). Equivalent diameter is defined as, $d_e = \sqrt{\frac{4A}{\pi}}$ where, A is the area of a floc. Figure 2.7 shows the image of *P. fluorescens* bacterial floc and relative frequency histogram. The bacteria culture was mixed with 200 nm red fluorescent amine-coated polystyrene (PS) microspheres (Thermo Fisher Scientific, MA, USA) to track the bacterial streamer.

2.3 Experimental setup

2.3.1 Volumetric flow-driven microfluidic experimental set-up

Plastic tubes were connected at inlet and outlet ports of the microfluidic device. Bacteria solution was taken in a 1 ml syringe. The tubing that goes to

the inlet port was connected with the syringe needle. The syringe was placed on the syringe pump (Harvard Apparatus, ON, Canada).

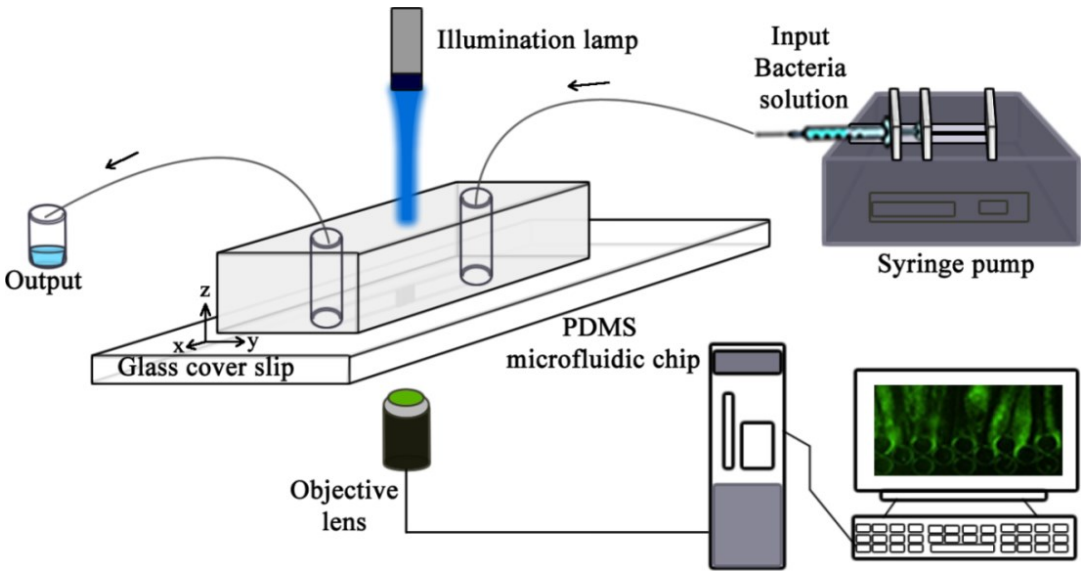

Figure 2.8: Schematic diagram of experimental set-up under flow-driven flow.

The outlet tube was placed in a beaker. The bacterial solution was injected to the microfluidic chip by using the syringe pump. The microfluidic chip was placed under inverted fluorescence microscopy system to observe the bacterial behaviour during the experiment. Confocal images were captured using an inverted spinning-disk confocal microscope (Olympus IX83). For epi-fluorescence imaging, GFP Long-pass green filter cube (Nikon and Olympus) and Texas red filter cube (Nikon and Olympus) were used. Image processing was performed by using NIS-Element AR software interface (Nikon). A schematic diagram of experimental setup is shown in Fig. 2.8.

2.3.2 Pressure-driven microfluidic experimental set-up

Pressure-driven flow was created in the microfluidic channel with a pump (Model: MFCS-EZ channel, 0-2 bar, Fluigent, MA, USA) as shown in Fig. 2.9. P_1 and P_2 denote the air pressures in the feed that was controlled by the pump and normal atmospheric pressure in chambers, respectively. For each experiment, the pressure difference ($\Delta P = P_1 - P_2$) was maintained at a constant value. The volumetric flow rate (Q) was measured directly using the flow unit (Model: Flow Unit M, 0-80 uL/min for water, Fluigent, MA, USA) and the corresponding values are obtained from the flow-rate-control-module software (Fluigent, MA, USA). The sensor inside the flow unit measured the spread of heat that is related to Q and provided the information of Q inside the unit. All experiments were performed at room temperature.

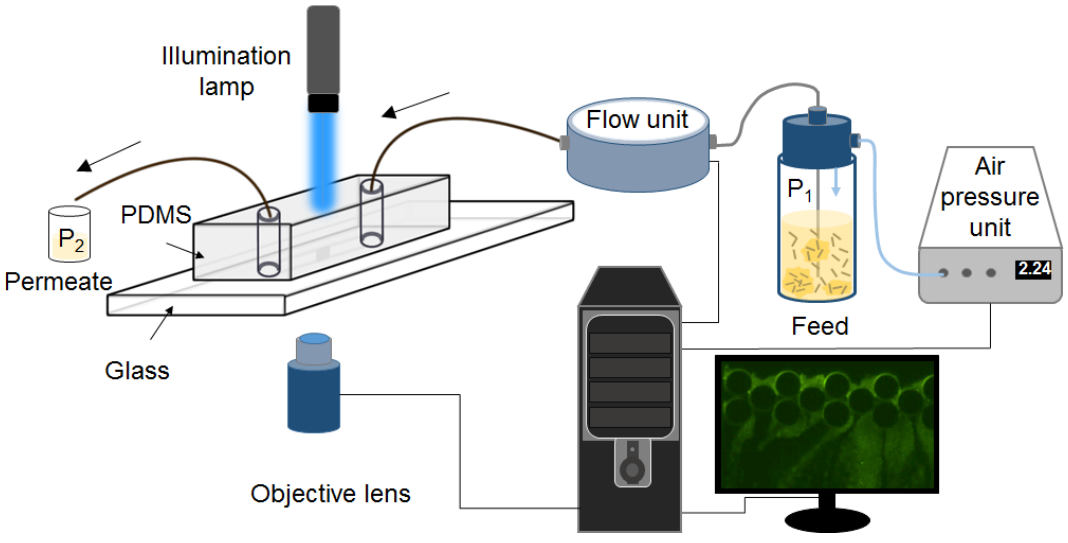

Figure 2.9: Schematic diagram of experimental set-up under pressure driven flow.

Chapter 3 [§]

Nonlinear deformation and localized failure of bacterial streamers in creeping flows

[§]Material of this chapter has been published in "Ishita Biswas, Ranajay Ghosh, Mohtada Sadrzadeh & Aloke Kumar, *Nonlinear deformation and localized failure of bacterial streamers in creeping flows*. Scientific Reports, 2016. **6**: p. 32204."

3.1 Introduction

Bacterial streamers, which are microscopically slender filamentous aggregates primarily comprising of bacterial cells encased in matrix of self-secreted extra-cellular polymeric substances (EPS) [5] and formed typically under sustained hydrodynamic flow. Bacterial streamers have been found to form in both turbulent flow conditions [59, 76] and even creeping flow conditions (Reynolds number (Re) $<< 1$) [70, 77]. Streamer formation under low Reynolds number ($Re < 1$) conditions has recently attracted attention as they can have significant impact on the performance of filtration units [39, 78] and biomedical devices [70, 79, 80]. More importantly, their filamentous structure can extend significantly with flow [6, 38, 77], thereby spanning several disconnected surfaces otherwise not easily possible for other similar aggregative modes of bacterial life such as flocs, pellicles or biofilms. This can make colonization rapid, pervasive and resistant to erosion with flow [70, 71]. Therefore, a better understanding of deformation, failure and, disintegration of streamers forming in low Reynolds number conditions is crucial from both physical and biological perspectives. Unfortunately, the literature on this subject is sparse and often lacks a deeper mechanistic exploration. For instance, Valiei et al.[6] had reported observing failure of streamers in their experiments on a microfluidic device with micro-pillars. However, since the primary focus was formation of streamers, failure was not discussed in detail. Das and Kumar [81] carried out a theoretical investigation on the formation and disintegration of biofilm streamers treating them as liquid jets in their terminal configuration.

This assumption, while suitable for streamer formation time-scales (t_s of several hours, seems to be too restrictive in light of the subsequent and current experiments [71] which indicate that streamers can also form at very short time-scales ($t_s \sim seconds$) with significant initial and residual elasticity. The overall complexity of the material behavior of the streamers is due to the EPS which contains biological macromolecules whose unfolding and 'flow' can introduce highly nonlinear stress-strain relationships [82, 83], and the embedded, significantly stiffer biological cells [84] forming a multiphase composite soft media. Thus, studying deformation and failure of streamers can be especially challenging since the complexity of the material constitution and formation process itself can be significantly reflected and amplified. Another challenge that plagues such studies is that as these streamers form in very small scale devices, and thus they do not accrue enough biomass to be subjected to *ex-situ* material characterization tests. Moreover, *ex-situ* measurements are usually very invasive for the delicate biomass. Hence, *in-situ* measurements and/or characterization methods must be developed.

In this chapter, we report a quantitative study and *in-situ* observation of the ultimate failure and instability of bacterial streamers formed from bacterial flocs[71] for two separate bacterial strains using a microfluidic platform. We observe explicitly that although the streamer material is a complex composite soft material and remains tightly influenced by the nature and dynamics of the immersed fluid, a highly localized failure via necking is common and widespread in this type of system. This may be contrasted to the global nature of hydrodynamic instabilities which thus indicates that even up until the terminal stages, the streamers retains significant distinctions from

purely viscous jets [81]. We also carry out analytical instability analysis assuming a localized failure on a simplified system incorporating mechanical nonlinearity, surface tension and fluidic loading which provides a power law scaling between the strain at failure and background flow which shows excellent qualitative and quantitative agreement with our experimental observations. Interestingly, this highly localized failure also ensures that a significant portion of the streamer, attached to the wall, is still preserved unlike global instability or shear failure at the wall. Thus, we find that streamer failure may not coincide with actual annihilation or erosion of streamers. To the best of our knowledge, this is the first study that reports a quantitative in-situ observation of the failure along with a continuum mechanics model for the same.

3.2 Results

3.2.1 Experimental results

Our microfluidic device (Fig. 2.2) consisted of an array of PDMS micropillars in a staggered grid pattern. The micropillars had a diameter of (d) of $50\ \mu m$ and were spaced $10\ \mu m$ apart (P). Bacterial flocs laden fluid was injected in the device using a syringe pump and the fluid flow rate (Q) was maintained at a level such that the resultant flow in the device was in the creeping flow regime ($Re << 1$). The velocity scale (U) in the device is defined by the relationship $U = Q/(W \times h_c)$. Bacterial flocs laden flow in the device led to the rapid formation of bacterial streamers.

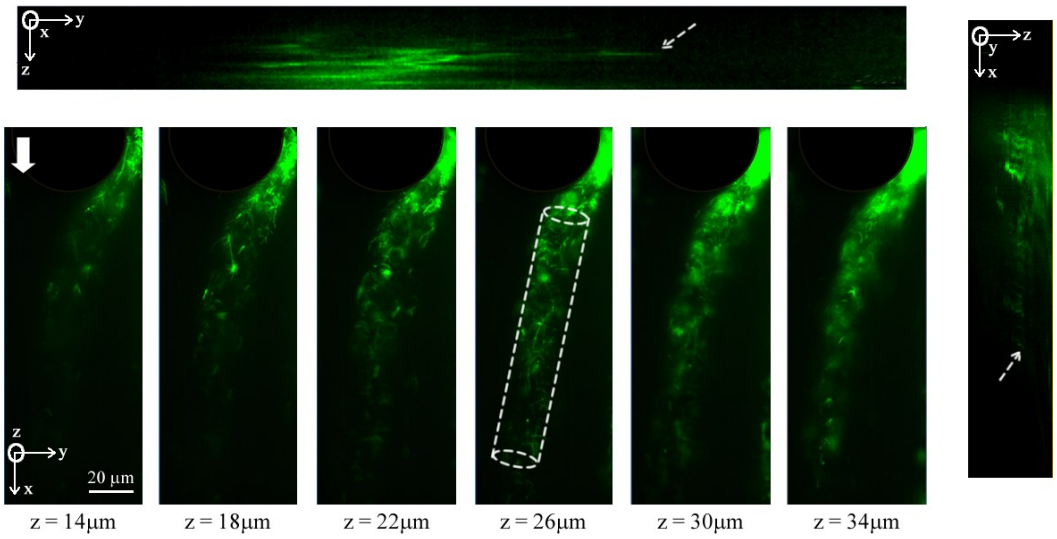

Figure 3.1: The geometry of one *P. fluorescens* streamer. Confocal sidebars shows y-z plane (top) and z-x plane (right) the thickness of one streamer through the height of the pillar. The approximate length of the streamer is 190 µm, width and thickness are 20 µm. White arrow shows the flow direction in the chip. The dashed white lines show the cross-section of the streamer in the x-y plane. The relatively similar cross sectional span and their uniformity through the depth of the streamer confirm a relatively cylindrical profile of the streamer away from the wall. The dashed arrows on the confocal sidebars show that the streamer does not come in contact with either the ceiling/floor of the device.

Such a mode of streamer formation has already been studied by Hassanpourfard et al. [71], which showed that bacterial flocs could adhere to micropillar walls and get rapidly sheared by background flow to form streamers. In an earlier publication, Hassanpourfard et al. [71] had studied the inception of streamers from flocs and found nucleating streamers to be dominated by large recoverable strains indicating significant elasticity.

In our work we employed this floc-mediated route to create streamers for two separate bacterial strains – (i) a green fluorescent protein (GFP) expressing *Pseudomonas fluorescens* strain and (ii) *Pseudomonas aeruginosa*. These streamers typically have a cylindrical geometry with large aspect ratio.

This can be seen in Figure 3.1, which shows a *P. fluorescens* streamer imaged using fluorescence microscopy. The confocal sidebars in Figure 3.1 also show that the section of interest of the streamer does not come in contact with either the ceiling/floor of the device. In the current experiments our focus is on observing nonlinear behavior including instabilities and failure of streamers. Figure 3.2 depicts failure in a streamer for a *P. fluorescens* streamer formed in our device after approximately 20 minutes of starting the experiment. The corresponding velocity scale and Reynolds number for the experiments were $U = 8.92 \times 10^{-4}\mathrm{m/s}$ and $Re \sim 10^{-3}$.

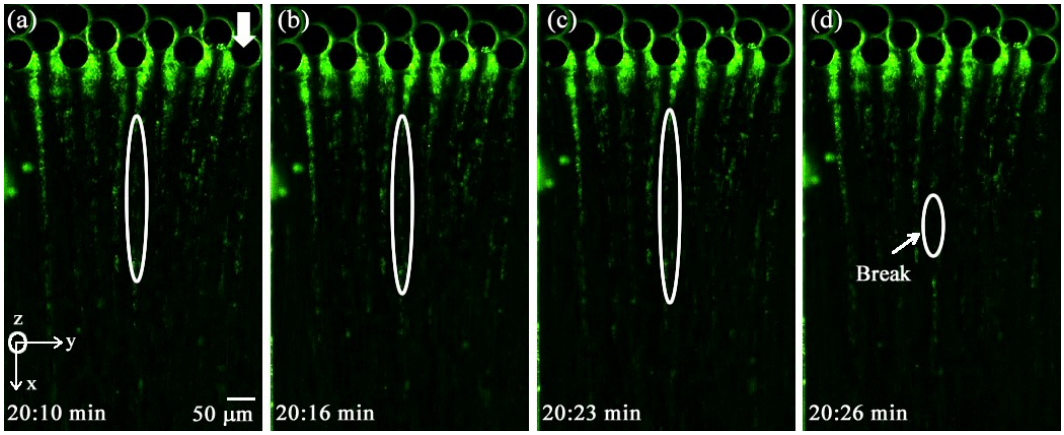

Figure 3.2: Observation of instability and failure in *P. fluorescens* streamers under fluorescence imaging using Green filter cube at $U = 8.92 \times 10^{-4}\, m/s$. (a)-(c) shows the stretching of one streamer with time and final breaking point shows in (d). The arrow showing flow is aligned to the x-direction of the chip.

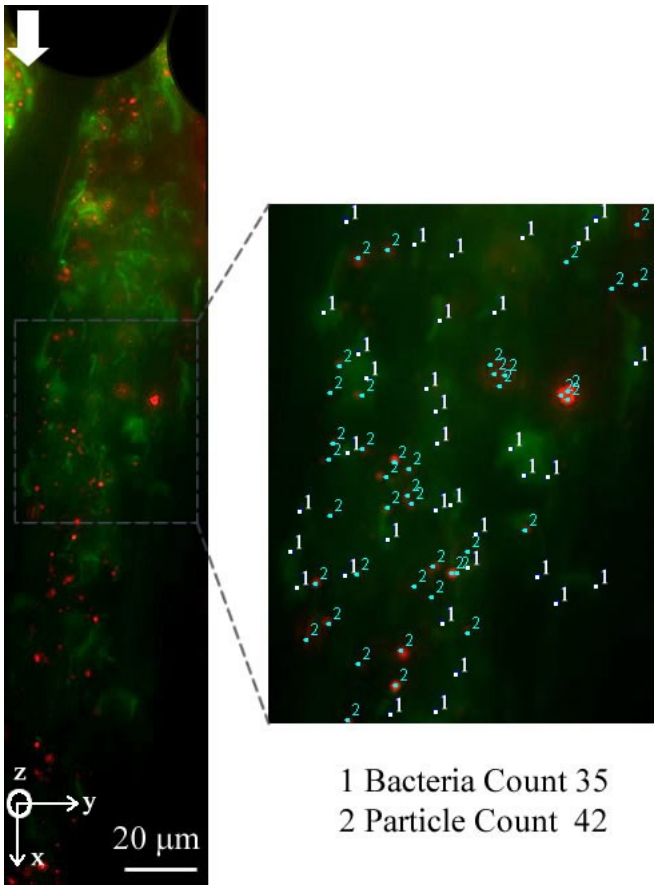

Figure 3.3: Bacteria and particle count in one *P. fluorescens* streamer's failure zone (dotted box). The volume of zoomed picture is calculated by multiplying the area of the picture with depth of field and is approximately $2000\ \mu m^3$. Bacteria cell is cylindrical and particles are spherical in geometry. Diameter of bacteria and particle are $0.2\ \mu m$ and the height/ length of one bacteria is $8\ \mu m$. Volume of one bacteria is $0.25\ \mu m^3$ and one particle is $4.19 \times 10^{-3}\ \mu m^3$.

A similar behaviour is observed for *P. aeruginosa*. These experiments which clearly show the evidence of far from wall failure and instability are nevertheless less useful in quantifying the failure process due to the invisibility of the EPS. The bacteria themselves although clearly visible are a poor proxy for quantification due to their relatively non-uniform and sparse distribution in the EPS. In order to alleviate this problem, we repeat these experiments

with 200 nm red fluorescent amine-coated polystyrene micro-spheres, which are of different color, much smaller and numerous thereby making quantification and visualization of instability much easier and more accurate. We found relatively dilute concentration of approximately 0.009% (v/v) of nanoparticles compared to bacteria which was about 0.4% (v/v). The volume fraction calculations is shown in Fig. 3.3.

Since the Young's modulus of bacterial cells ($\sim O(10^2$ MPa))[85] and polystyrene microspheres ($\sim O(10^3$ MPa))[86] are comparable, and they themselves undergo no noticeable deformation, this ensures little contribution of beads to the overall mechanical behavior of the streamer biomass itself. Utilizing this technique, we depict the visualization and quantification of a *P. fluorescens* streamer undergoing axial failure in Fig. 3.4, where embedded particles are used to illuminate the EPS. The background velocity scale for the experiment was kept constant at $U = 8.92 \times 10^{-4}\mathrm{m/s}$ during this experiment.

These observations indicated that the streamer deformation clearly occurs in three distinct phases. The first - formation stage occurs almost as soon (t_{form}) as the flow stabilizes, which is typically in seconds and in agreement with earlier streamer formation experiments on similar systems [71]. The streamers thus formed continue to retain their shape and size, remaining apparently static against a steady background flow till about time $t_0 \gg t_{form}$when deformation begins again. The time between t_{form} and t_0 where the streamer formation is complete but the next stage of deformation is not yet perceptible can last for several minutes.

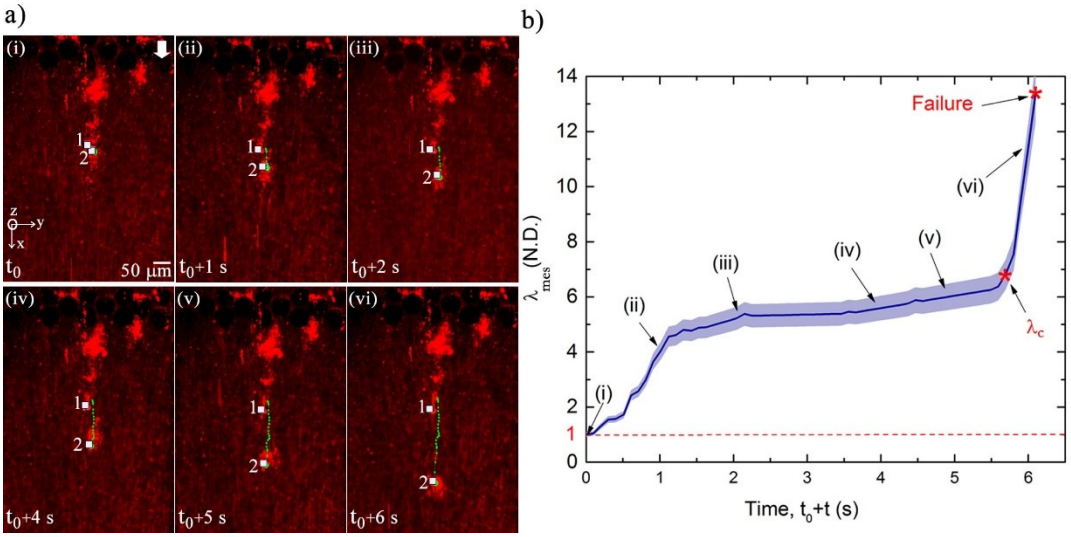

Figure 3.4: (a) Temporal behavior of two Lagrangian points ('1' & '2'), which lie inside a *P. fluorescens* streamer, culminating in the failure of streamer. Other pertinent parameters are $U = 8.92 \times 10^{-4}\, m/s$ and $t_0 = 30.34$ minute. (b) Stretch ratio for the same streamer as a function of time. The blue shaded region denotes the estimated error envelope. Data points corresponding to the experimental conditions ((i)-(vi)) are depicted on the curve. Stretch ratio is not computed once failure occurs in the streamer. Note that the blue shaded region denotes the estimated 4% tracking error envelope applicable for any observed streamer.

The nature of this quiescence is as of yet unclear and may simply be another creep stage with extremely small strain rate or a period of microstructural rearrangement before perceptible creep sets in. In any case, we are interested in quantifying the deformation which was observed only after t_0. After t_0, which can last for several minutes after the initiation of the experiment, streamers begin to deform perceptibly, resembling a creep type deformation over a much larger time scale ($t_{cr} \gg t_{form}$) . This creep stage ends rather abruptly through a short region of increasing deformation culminating in a distinct sharply defined instability after which the streamer suffers

terminal failure through a final catastrophic large deformation stage occurring over a much smaller time scale $(t_{fail} \ll t_{cr})$.

The different space-time scales of the observed deformation regimes, which are of the same order for both bacterial strains, are schematically illustrated in Fig. 3.5. A better quantification of this phenomenon is possible due to the embedded particles mentioned earlier. Two such particles which lay on either side of the localized failure zone were specifically tracked in the video from the beginning of the creep phase (time t_0) to measure the temporal evolution of deformation (Fig. 3.4 a). The deformation is quantified using a non-dimensional measured 'stretch ratio' defined as $\lambda_{mes} = |dx|/|dX|$, where $|dX|$ is the distance between the two points at time t_0 and $|dx|$ is the distance between the two points at any given time t $(t > t_0)$.

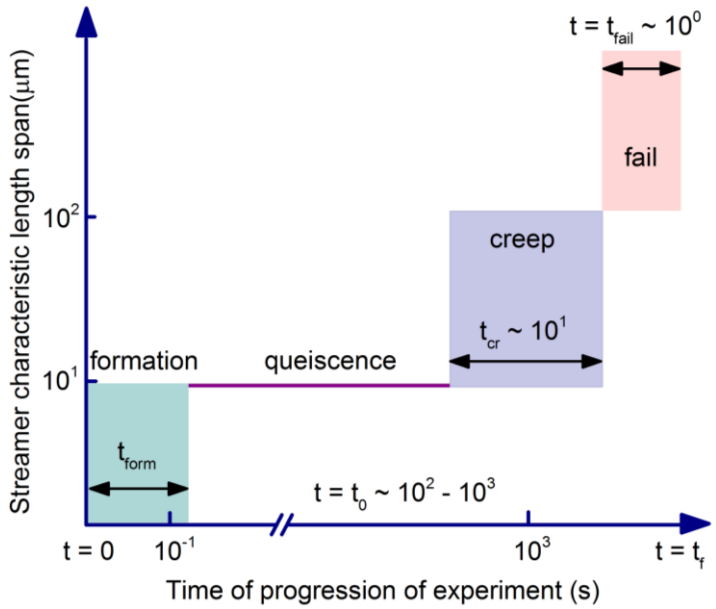

Figure 3.5: Schematic illustration of space-time scales corresponding to regimes observed in the experiments.

In this context, it is useful to recall that there are several ways to quantify deformation. Any general deformation can be decomposed into a rotation and a stretch (Polar decomposition theorem [87]). Thus stretch is a primitive form of deformation quantification.

Strains are functions of stretches and can be of many different types (e.g. Engineering, Cauchy-Green, Green-Lagrange, Hencky etc.) depending on the choice of the problem. Therefore, we have used stretch as a fundamental and intuitive measure of deformation for this problem. Figure 3.4 b depicts the time-evolution of λ_{mes} for a couplet on a particular *P. fluorescens* streamer. It is important to recall that $\lambda_{mes} = 1$ corresponds to the time when the streamer formation and initial deformation in response to the fluidic loading is complete and thus the beginning of the creep stage. In this regards, observing that the background flow is steady with little mass addition in this phase, Fig. 3.4 a, and the fact that creep is seen to occur over a much shorter time scale than typical bacterial reproduction time-scale $t_{bio} \gg t_{cr}$ (~20 min) [88], we conclude that the creep type deformation has origins in the material constitution. Within the creep stage, we find three distinct deformation regimes beginning first with a rather rapid strain rate regime, which then decreases significantly indicating substantial hardening of the material, stabilizing to almost a constant strain rate. This continues for some time until the strain rate begins to increase again and the streamer deformation accelerates, transitioning after a critical stretch ratio λ_c into the terminal failure stage, mentioned earlier. The ultimate failure process observed through microscope shows significant localization, with the streamer structure left almost entirely intact at either side of instability resembling a necking route to failure of solids under axial loading.

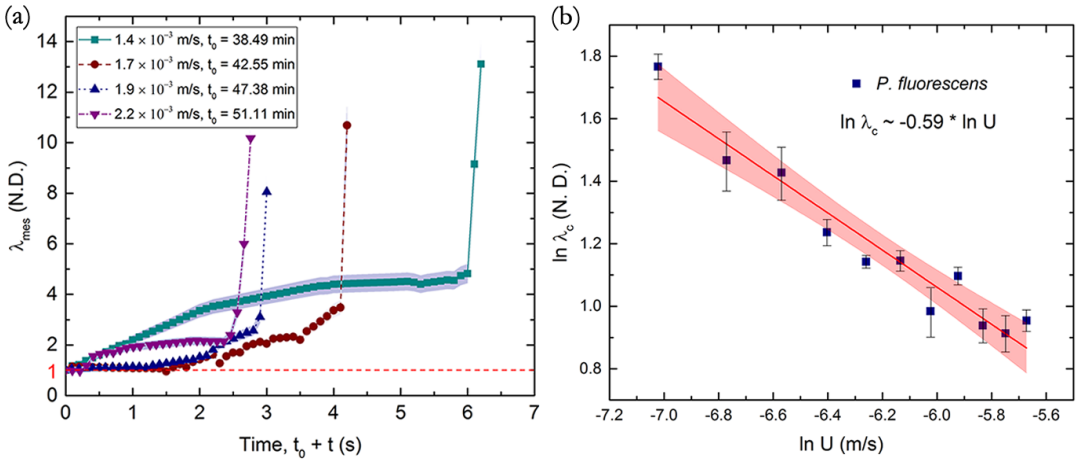

Figure 3.6: (a) Stretching of *P. fluorescens* streamers with time at different background flow velocity scale (U) and t_0. Note that the blue shaded region denotes the estimated 4% tracking error envelope applicable for any observed streamer. (b) $\ln \lambda_C$ for different flow rates, shows a linear behavior with $\ln U$. The blue squares represent experimental data and the red line represents a linear regression fit. The R^2 value corresponding to the regression fit is greater than 0.9. The red envelope depicts the 95% confidence interval for linear regression.

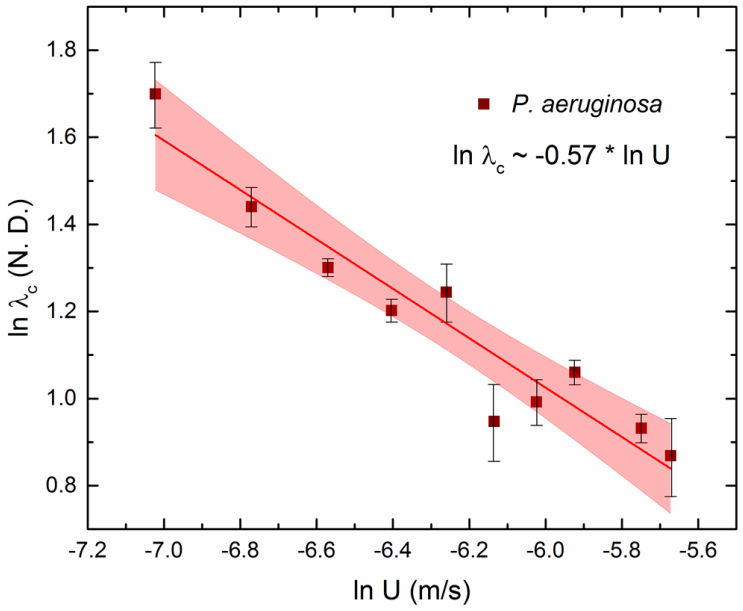

Figure 3.7: $\ln \lambda_C$ for different flow rates for *P. aeruginosa* streamers show a similar scaling with $\ln U$. The brown squares represent experimental data and the red line represents a linear regression fit.

This failure behaviour is observed in both bacterial strains suggesting a mechanistic origin of the instability. Note that within these broad stages of deformation, some irregularities are possible for some streamers such as temporary secession of creep and then sudden resumption due to local rearrangement of the micro or meso-structure of the highly complex streamer constitution. We also note that the setup used in these experiments can result in multiple streamers being formed at various locations and at different times.

However, when the temporal origins are normalized and each streamer tracked with particle couplets using the method described earlier, we observe broadly similar distinctive creep regimes which lasted for similar time scales (although with different deformation magnitudes for a given regime) and ended with similar critical stretch ratios across streamers considering the enormous variation possible in their material composition and shape. Figure 3. 6 a where we plot the creep response of *P. fluorescens* streamers under different flow velocities and notice again very similar deformation regimes. However, the duration of the regimes vary considerably with the flow velocity.

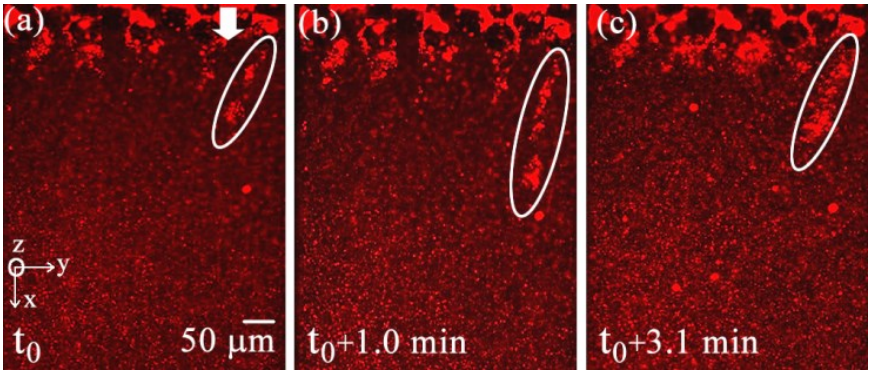

Figure 3.8: Stretching and relaxation of a *P. fluorescens* streamer as flow rate is increased ($a \rightarrow b$) and subsequently decreased ($b \rightarrow c$).

More interestingly, we find that the critical axial stretch ratio at failure steadily decreases with increasing flow, Fig. 3. 6 b, defining thereby a clear monotonic decreasing rupture envelope. This is in clear contrast to liquid jet breakup which indicates a monotonic increasing envelope [81, 89]. More interestingly, we find a clear power law scaling of the failure stretch rate with flow, $\lambda_c \sim U^{\alpha}$ where $\alpha = -0.59 \pm 0.052$, Fig. 6b. When these experiments were repeated for *P. aeruginosa* we were able to recover a very similar power law with $\alpha = -0.57 \pm 0.060$ (Fig. 3.7). Thus, we see that the scaling relationship $\lambda_c \sim U^{\alpha}$ appears to be a general biophysical phenomena with an average exponent $\alpha \approx -0.58$. A phase change into a liquid phase is also ruled out through direct observation of elastic recoil even after the onset of terminal instability using a separate quenching experiment where the flow was suddenly stopped thus removing external loading on the streamer, Fig. 3.8.

3.2.2 Experimental uncertainty

Two separate sources of experimental uncertainty were identified. The first is the repeatability error accounting for the heterogeneity of the biomass itself. Due to the very nature of this error, it has to be evaluated by statistical means (i.e. from a number of repeated observations). For each of two cases, the experiments were repeated 2-4 times for all flow rates to yield relative uncertainty estimates. Figure 3.9 shows a sample set of streamers. For example, for the *P. fluorescens* for the flow velocity ($U = 8.92 \times 10^{-4}$ m/s), the experiment was repeated three times thus yielding relative uncertainty for each U (Fig. 3.9). Table 3.1 provides the complete list of repetitions for each case.

Let this uncertainty be denoted by δ_{repeat}. The second source of uncertainty resulted from an error in the tracking process itself. This error could be estimated by visually determining the uncertainty in tracking the Lagrangian points and the maximum error was estimated to be approximately 4%. This determines the error envelope for a single tracking of couplets. Let this uncertainty be denoted by $\delta_{tracking}$. The final error envelope (δ) for critical stretch ratio is given by: $\delta = \sqrt{\delta_{repeat}^2 + \delta_{tracking}^2}$. Error bars in Figs. 3.6 b and 3.7 represent δ.

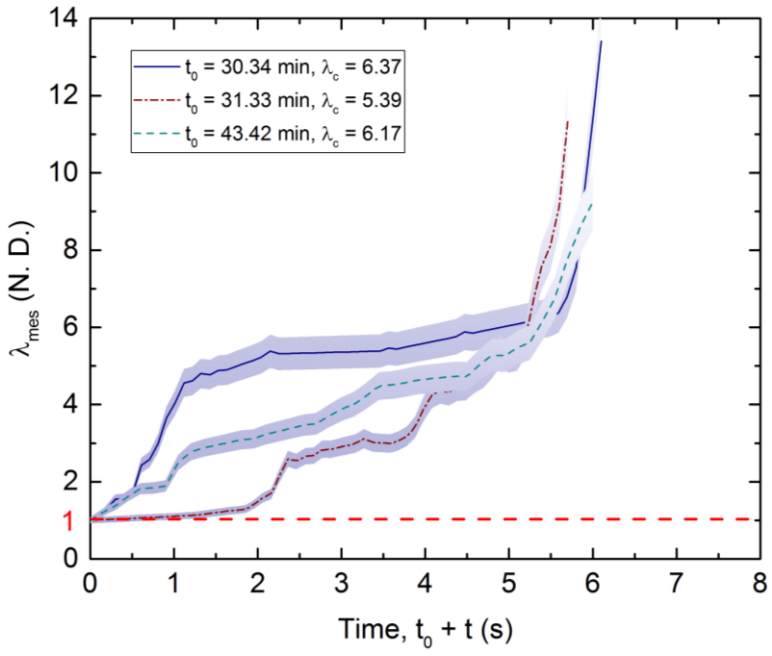

Figure 3.9: Stretch ratio for three different failure events of *P. fluorescens* streamers at a constant background velocity of $U = 8.92 \times 10^{-4}\, m/s$. Legend shows the t_0 and critical stretch ratio for the three different cases.

Table 3.1: Repeatability data for finding different λ_c for different Q for the two cases.

Parameters	**λ_C (N. D.)**		**Parameters**	**λ_C (N. D.)**	
Velocity, U, m/s	***P. fluorescens***	***P. aeruginosa***	**Velocity, U, m/s**	***P. fluorescens***	***P. aeruginosa***
8.92×10^{-04}	6.00	5.83	**2.17×10^{-03}**	3.29	3.09
	5.39	5.74		2.97	2.33
	6.17	4.29		3.17	2.31
	-	6.03	**2.42×10^{-03}**	3.09	2.88
1.15×10^{-03}	3.35	3.95		2.67	2.51
	4.87	4.11		2.27	-
	4.04	4.60	**2.68×10^{-03}**	3.02	2.76
	5.10	-		2.85	2.93
1.40×10^{-03}	4.82	3.66		3.14	2.83
	4.23	3.69		2.98	3.02
	3.46	-	**2.93×10^{-03}**	2.82	-
1.66×10^{-03}	3.48	3.35		2.30	
	3.54	3.25		2.55	
	3.09	3.23	**3.19×10^{-03}**	2.68	2.40
	3.67	3.47		2.61	2.57
1.91×10^{-03}	3.11	3.16		2.18	2.65
	3.14	3.78	**3.44×10^{-03}**	2.40	1.99
	3.16	-		2.67	2.82
				2.70	2.34

3.2.3 Streamer instability calculations

In order to extract further insights from these experimental observations, we take recourse to an analytical stability analysis of a simplified version of this structure.

3.2.3.1 Kinematics

To this end, we first recall that the measurements of axial stretch ratios were taken by tracing the tracking couplets back in time till a creeping type deformation begins. It is typical to assume that the total stretch λ can be multiplicatively decomposed into elastic λ_ϵ and a creep component λ_{cr} [90]. Furthermore, we assume that in light of extreme deformation suffered by the initial floc which precipitates the streamer formation [71], the limiting chain length extension [91-93] of the polymeric material dominating the streamer is reached at the end of the elastic phase. This behaviour is consistent with preliminary characterization of biofilm materials which show pronounced strain stiffening [84]. With this simplification, we can assume that the experimentally reported stretch ratios in this paper are purely due to creep with elasticity preceding the origin of the plots. This split in the regimes would mean that the experimentally reported stretch ratios in Fig. 3.4 b and 3.6 a are essentially $\lambda_{cr} = \lambda/\lambda_e \approx \lambda_{mes}$ and that the incremental deformation measured are entirely due to creep.

The streamer is assumed to be slender cylindrical body (long wavelength defect approximation) throughout till the onset of instability. In the reference and current configuration, the radius of the cylinder are R, r and length L, l respectively. We also assume the streamer to have uniform behavior throughout its material volume except at the far field boundaries before the onset of instability.

We also assume that streamer deformation is purely inelastic after the elastic limit is reached and to remain in this state till the onset of instability.

We assume that inelastic deformation is isochoric and describe the geometry of the current streamer (right cylinder) with radius r and length l. Thus, in the rate form we arrive at the following relationship:

$$2\frac{\dot{r}}{r}+\frac{\dot{l}}{l}=0 \tag{3.1}$$

Now assuming uniform conditions inside the streamer. Since the deformation after elastic limit is purely inelastic, we define the axial creep strain as $\delta\epsilon_{cr}=\delta l/l$. Integrating it from the elastic limit where the dimensions of the cylinder are assumed to be $R\times L$ to current configuration gives us the following logarithmic inelastic strain:

$$\epsilon_{cr}=\int_{L}^{l}\frac{dl'}{l'}=ln\frac{l}{L}=ln\,\lambda_{cr} \tag{3.2}$$

$$\dot{\epsilon}_{cr}=\dot{l}/l \tag{3.3}$$

Where, λ_{cr} is the creep stretch. Imposing isochoric deformation in inelastic regime and assuming a cylindrical geometry of the specimen throughout deformation (akin to long wavelength defect approximation for axial tensile stability analysis [94, 95]), we relate the current geometry to the reference geometry corresponding to the end of formation stage. To this end if the reference cylinder had a radius R (and length L) which is deformed in the inelastic regime into another cylinder of radius r (and length l), the reference

slenderness ratio $\Omega = L/R$ can be related to the current slenderness ratio $\omega = l/r$ as:

$$\omega = \Omega \left(\frac{l}{L}\right)^{3/2} = \Omega\, e^{\frac{3}{2}\epsilon_{cr}} \tag{3.4}$$

Thus this also shows that $l = \omega^{2/3}\Omega^{-2/3}\, L$ and $r = R\Omega^{1/3}\omega^{-1/3}$. In the rate form Eq. (3.4) becomes

$$\dot{\omega} = \frac{3}{2}\omega\, \dot{\epsilon}_{cr} \tag{3.5}$$

Note that for a linear elastic isotropic solid, a total of two independent material constant are needed for complete characterization. These are the Young's modulus (E) and Poisson's ratio (ν). The Poisson's ratio is the ratio of the strains in the lateral to longitudinal direction. If the constraint of isochoric deformation (sometimes called incompressibility) is imposed on the system, one can obtain $\nu = 0.5$ [96]. On the other hand, the inelastic regime is often assumed isochoric independently from the elastic case for a large number of materials and the physical origin of this assumption can be found in classical treatises in plasticity [97, 98]. Thus, in this case, in the inelastic regime the constraint of isochoric deformation and shape preservation dictates the evolution of the slenderness ratio.

3.2.3.2 Mechanics

Using confocal microscopy we confirm a reasonably cylindrical geometry of the specimen away from the walls along with a high slenderness ratio (length

to radius ratio ≈ 10), Fig. 3.1, which is imaged using only green fluorescence where only *P. fluorescens* bacterial cells are visible with both the encapsulating EPS and liquid media appearing dark. Now, if we assume that the surrounding fluid only exerts traction and does not lead to significant mass addition, the streamer and the force field can thus be assumed to be a closed system exchanging only heat with a thermal reservoir to maintain isothermal conditions. Using the internal variable framework incorporating internal dissipation [99, 100], instability is then said to occur when perturbation to neighbouring states can result in decrease in total free energy G. In other words, for instability:

$$\Delta G = G_1 - G_0 = \dot{G_0}\Delta t + \frac{1}{2!}\ddot{G}_0\Delta t^2 + \cdots < 0 \tag{3.6}$$

Where Δt is the perturbation time of interest. Now note that due to the stationary nature of equilibrium, $\dot{G_0} = 0$ and thus it is the sign of the second derivative, which will determine the stability of equilibrium. Specifically, the instability conditions can be obtained through the equation $\ddot{G_0} = 0$, which denotes the point of transition from stability to instability. To evaluate the condition of instability we first write the free energy rate for this system in the current configuration:

$$\dot{G} = \dot{\phi}(\epsilon_{cr}, \dot{\epsilon}_{cr})\pi r^2 l + \gamma_S \dot{A_S} - \Delta\dot{W}_P - F_{fl}\dot{l} \tag{3.7}$$

Where, ϕ is the dissipation density function which can in general depend on the strain and strain rate, γ_S is the surface tension (assumed uniform and without any Marangoni effects), $\dot{A_S}$ is the rate of change of surface area, $\Delta\dot{W}_P$

is the rate of work done by the pressure difference between the inside and outside of the streamer and F_{fl} is axial the fluidic traction force. We can write the rate of change of surface area as:

$$\dot{A}_S = \frac{d}{dt}(2\pi rl + \pi r^2) = 2\pi rl\left(\frac{\dot{r}}{r} + \frac{\dot{l}}{l} + \frac{\dot{r}}{l}\right) \approx \pi r\dot{l} = \pi rl\dot{\epsilon}_{cr}, \;\; \omega \gg 1 \tag{3.8}$$

For the rate of pressure work, we have:

$$\dot{W}^{pr} = \Delta p 2\pi rl\,\dot{r} - \Delta p\pi r^2\dot{l} = \Delta p\pi r^2 l\left(\frac{2\dot{r}}{r} - \frac{\dot{l}}{l}\right) = -2\Delta p\pi r^2 l\,\dot{\epsilon}_{cr} \tag{3.9}$$

where $\Delta p = p_0^{ex} - p_0^{in}$ is the pressure differential between outside p_0^{ex} and inside pressure p_0^{in}. In subsequent calculations, we will neglect end area of the cylinder in our energy calculations due to the observed high slenderness ratio $(\Omega, \omega \gg 1)$. The high slenderness ratio when combined with the low Reynolds number flow also allows us to use the slender body approximation for our fluidic force on the cylinder leading to [101] $F_{fl} = C\pi\mu U/\ln\omega$ where μ is the viscosity of the fluid, U is the fluid velocity scale and C is an appropriate scaling constant. Thus, we get for the fluidic work rate, $F_{fl}\dot{l} = \frac{C\pi Ul}{\ln l/r}\,\dot{l} = \frac{C\pi Ul^2}{\ln\omega}\,\dot{\epsilon}_{cr}$.

Using these expressions and then dividing Eq. (3.1) by the current volume $\pi r^2 l$ we have:

$$\dot{g} = \dot{\phi}_d(\epsilon_{cr}, \dot{\epsilon}_{cr}) + \frac{\gamma_S}{r}\dot{\epsilon}_{cr} - 2\Delta p\dot{\epsilon}_{cr} - C\pi\mu U\,\frac{\omega^2}{\ln\omega}\frac{1}{l}\dot{\epsilon}_{cr} \tag{3.10}$$

where V_0 is the constant reference volume. Before evaluating second derivative, we first note from Fig. 3.4b that in our problem the strain rate variation before the onset of instability has a much higher Deobrah number $\left(De_{\dot{\epsilon}_{cr}} \gg 1\right)$ with respect to the time scale of instability precipitation and can thus be assumed to be frozen[99] for our current calculation. On the other hand, the pressure differential has a much lower Deborah number $\left(De_{\Delta p} \ll 1\right)$ due to relatively free passage of water throughout the streamer and thus assumed to be nearly equilibrated [99] for the time scale of our calculation. The second time derivative of Eq. (3.10) leads to

$$\ddot{g} = \ddot{\phi}_d(\epsilon_{cr}, \dot{\epsilon}_{cr}) - \frac{\gamma_S}{r^2}\,\dot{r}\dot{\epsilon}_{cr} - C\mu U \frac{d}{dt}\left(\frac{\omega^2}{\ln\omega}\frac{1}{l}\right)\dot{\epsilon}_{cr}$$

$$= \ddot{\phi}_d(\epsilon_{cr}, \dot{\epsilon}_{cr}) + \frac{1}{2}R^{-1}\Omega^{-\frac{1}{3}}\omega^{\frac{1}{3}}\gamma_S\,\dot{\epsilon}_{cr}\dot{\epsilon}_{cr} - C\mu U \frac{d}{dt}\left(\frac{\omega^2}{\ln\omega}\,\omega^{-\frac{2}{3}}\Omega^{\frac{2}{3}}L^{-1}\right)\dot{\epsilon}_{cr}$$

$$= \ddot{\phi}_d(\epsilon_{cr}, \dot{\epsilon}_{cr}) + \frac{1}{2}R^{-1}\Omega^{-\frac{1}{3}}\omega^{\frac{1}{3}}\gamma_S\,\dot{\epsilon}_{cr}\dot{\epsilon}_{cr} - C\mu U\,\frac{d}{dt}\left(\frac{\omega^{\frac{4}{3}}}{ln\,\omega}\,\Omega^{\frac{2}{3}}L^{-1}\right)\dot{\epsilon}_{cr}$$

$$= \ddot{\phi}_d(\epsilon_{cr}, \dot{\epsilon}_{cr}) + \frac{1}{2}R^{-1}\Omega^{-\frac{1}{3}}\omega^{\frac{1}{3}}\gamma_S\;\dot{\epsilon}_{cr}\dot{\epsilon}_{cr} - C\mu U\Omega^{\frac{2}{3}}L^{-1}\left\{\frac{\frac{4}{3}ln\,\omega\,\omega^{\frac{1}{3}} - \omega^{\frac{1}{3}}}{(ln\,\omega)^2}\right\}\dot{\omega}\dot{\epsilon}_{cr}$$

$$= \ddot{\phi}_d(\epsilon_{cr}, \dot{\epsilon}_{cr}) + \frac{1}{2} R^{-1} \Omega^{-\frac{1}{3}} \omega^{\frac{1}{3}} \gamma_S \, \dot{\epsilon}_{cr} \dot{\epsilon}_{cr} - C\mu \, U \Omega^{\frac{2}{3}} L^{-1} \left\{ \frac{\frac{4}{3} ln\, \omega \, \omega^{\frac{1}{3}} - \omega^{\frac{1}{3}}}{(ln\, \omega)^2} \right\} \frac{3}{2} \omega \dot{\epsilon}_{cr} \dot{\epsilon}_{cr}$$

$$= \ddot{\phi}_d(\epsilon_{cr}, \dot{\epsilon}_{cr}) + \frac{1}{2} R^{-1} \Omega^{-\frac{1}{3}} \omega^{\frac{1}{3}} \gamma_S \, \dot{\epsilon}_{cr} \dot{\epsilon}_{cr} - 2C\mu U \Omega^{\frac{2}{3}} L^{-1} \frac{\omega^{\frac{4}{3}}}{\ln \omega} \dot{\epsilon}_{cr} \dot{\epsilon}_{cr} \tag{3.11}$$

Now multiplying throughout by $\Omega^{\frac{1}{3}} \omega^{-\frac{1}{3}}$ and expanding the dissipation function using Taylor series in ϵ_{cr} we get:

$$\ddot{g} = \left\{ \frac{\partial^2 \phi_d(\dot{\bar{\epsilon}}_{cr}, \epsilon_{cr})}{\partial \epsilon_{cr}^2} \, \Omega^{\frac{1}{3}} \omega^{-\frac{1}{3}} + \frac{\gamma_S}{2R} - \frac{C' \mu U}{L} \, \Omega \frac{\omega}{\ln \omega} \right\} \dot{\epsilon}_{cr} \dot{\epsilon}_{cr} \tag{3.12}$$

Now recalling that $\omega, \Omega \gg 1$ and from Eq. 3.4 the vanishing second derivative gives us the following condition for instability at critical point:

$$\left(\frac{\partial^2 \phi_d(\dot{\bar{\epsilon}}_{cr}, \epsilon_{cr})}{\partial \epsilon_{cr}^2} \right)_c e^{-\frac{\epsilon_{cr,c}}{2}} + \frac{1}{2} \frac{\gamma_S}{R} - \frac{C' \mu U}{L} \, \frac{\Omega^2}{\ln \Omega} e^{\frac{3\epsilon_{cr,c}}{2}} = 0 \tag{3.13}$$

Where, $\dot{\bar{\epsilon}}_{cr}$ denotes the frozen strain rate for our calculation, C' is a positive dimensionless constant and subscript c indicates the state at the point of instability. Next, we develop a simple model to quantify the dissipation potential, which should be consistent with the observed strain hardening of the streamer material. To this end, we neglect poroelasticity as a source of creep since we already assumed that fluid can flow in and out of the streamer creating

a drained condition in the time scale of interest. The creep dissipation behaviour for the streamer material is currently unquantified. However, for this work, analogous to hyperelastic strain energy density functions, we would assume that the dissipation density function depends on the invariants of the left Cauchy-Green creep strain tensor[102]. For simplicity we postulate a linear dependence of the dissipation potential ϕ_d on the first invariant again drawing analogy from simple hyperelastic strain energy density functionals giving us the following functional form:

$$\phi_d = \phi_d(I_1) \approx HI_1 \tag{3.14}$$

where H is the hardening constant which can in general depend on stain rate and I_1 is the first invariant of the strain . Note that $I_1 = \lambda_1^2 + \lambda_2^2 + \lambda_3^2$ where $\lambda_1, \lambda_2, \lambda_3$ are three principal stretches of the streamer. Note that our previous study[71] on the subject highlighted both the strain rate dependence as well as significant elastic component of deformation in streamers under uniaxial loading even in large deformation. In this problem we assume that the significant inelastic deformation is perceptible (yield) after the streamers have exhausted their elastic limit of deformation. Thus any more deformation would arise from purely inelastic sources. In other words, further work done on the system would no longer be stored as elastic energy but need to be dissipated, quantified by the dissipation potential. The strain rate effects (viscous effects), on the other hand, which were present even in the pre-yield phase would still be perceptible in the dissipation regime since their origin is distinct from the purely elastic component. However, in the plateau region (see Fig. 3.4 b), the

strain rate is roughly constant till the instability begins to precipitate. Thus the strain rate components in the material models would simply be constants, which have been absorbed in the dissipation potential postulated in the problem. Assuming uniaxial tensile stretching for the streamer in the creep regime, with axisymmetry and incompressibility, we get the three principal stretches as $\lambda_1 = \lambda_{cr}, \lambda_2 = \lambda_3 = 1/\sqrt{\lambda_{cr}}$. Thus the dissipation potential becomes from Eq. (3.14) , $\phi_d = H\left(\lambda_{cr}^2 + \frac{2}{\lambda_{cr}}\right) = e^{2\epsilon_{cr}} + 2e^{-\epsilon_{cr}}$. Now neglecting the negative exponential in ϕ_d we have $\phi_d = He^{2\epsilon_{cr}}$ which when plugged into Eq. (3.13) gives us:

$$4He^{\frac{3\epsilon_{cr,c}}{2}} + \frac{1}{2}\frac{\gamma_S}{R} - \frac{C'\mu U}{L}\frac{\Omega^2}{\ln\Omega}e^{\frac{3\epsilon_{cr,c}}{2}} = 0 \tag{3.15}$$

Now note that due the limiting chain extensibility argument in the elastic regime, Ω, L are determined by the limiting chain behaviour of the streamer material. In general, the limiting chain extensibility is not a material constant but depends on the type of loading [91], however since the loading can be assumed to be more or less similar in the current experiment, it becomes a de facto material constant. Moreover, since the streamers have been shown to originate from the deformation of flocs, whose dimensions are roughly similar [71], we will assume that the dimension of the streamer at the end of elastic deformation remains fairly constant irrespective of the flow rate. If we denote the limiting chain material constant as J_m such as the one used in the widely employed Gent hyperelastic [103] or a similar constant from the Van der Waals polymer model [104], we can rewrite Eq. (3.15) as:

$$(\Upsilon - 1)e^{\frac{3\epsilon_{cr,c}}{2}} = \Gamma, \quad \Upsilon = \frac{\mu U}{H L_m}, \quad \Gamma = \frac{\gamma_S}{8HR}, \qquad L_m = \frac{L(J_m)\, ln\, \Omega(J_m)}{4C'\Omega^2(J_m)}, \qquad R = L(J_m)/\Omega(J_m) \tag{3.16}$$

Now let us assume that $\Upsilon \gg 1$, in other words, hardening is sufficiently small or limiting chain extensibility is sufficiently large. With these assumptions, taking logarithms both sides yields $\epsilon_{cr,c} \sim -(2/3)\ln U$. This scaling in excellent agreement with our experimental observations described earlier which indicate $\ln \lambda_c = \epsilon_{cr,c} \sim -0.6 \ln U$ where λ_c is the measured stretch ratio at instability, Fig. 6b and Fig 7. Note that in the high Υ limit, the actual value of H does not come in the final scaling since it cancels on both sides of Eq. (3.16), leaving only the elastic and surface tension properties along with fluid viscosity, i.e., $e^{\frac{3\epsilon_{cr,c}}{2}} \approx \frac{\Omega_m}{Ca}$, $Ca = \frac{\mu U}{\gamma_S}$ is the capillary number and $\Omega_m = \frac{L_m}{R}$. This relatively weak dependence on inelastic parameter somewhat narrows down the bandwidth of variation of this mode of streamer instability at a given flow and along with the inherent slender geometry may contribute to the observed generality of instability behaviour across streamers in spite of numerous well known complexities and variations in the streamer constitution.

3.3 Discussion

In this Chapter, we studied the deformation and failure behaviour of bacterial streamers for two separate bacterial strains by passing a floc laden flow through a specially designed microfluidic device. The flow corresponded

to very low Reynolds numbers and was sufficient to germinate streamers over timescales and configuration in agreement with prior experiments on streamer formation. However, we found that the apparent stability of the formed streamers transitioned slowly into complex creep like deformation regimes with their own characteristic time scales in spite of stable background flow conditions. The final stages of deformation were characterized by high strains over relatively small time scales leading to failure of the streamers. However, unlike previously believed fluid like models which could account for the creep as well as terminal failure of the streamers through a global hydrodynamic instability, we discovered highly localized failure of the streamers in our current experiments. Significant streamer recoil observed after the flow was stopped at the onset of instability confirmed residual elasticity. More interestingly, the distinct deformation regimes and the failure behaviour of the streamers were broadly exhibited by different streamers at different flow conditions in spite of the highly complex and heterogeneous nature of the streamers themselves. That this behaviour was common between streamers of two separate bacterial strains indicated a mechanistic route despite the system being biophysical in origin. We developed a simplified but nonlinear mechanical model incorporating inelasticity and surface tension to account for the failure behaviour assuming necking failure of the streamers. Our model based on these assumptions faired remarkably well against the rupture scaling obtained from our experiments. Interestingly, this mode of failure was found to be entirely different from shear failure at wall or global hydrodynamic instability. Last but not the least, since this mode of failure does not lead to a global disintegration of the streamer, its effect on biofouling could be different from other modes of failure.

Chapter 4 ‡

Near wall void growth leads to disintegration of colloidal bacterial streamers

‡The material of this chapter has been published in "Ishita Biswas, Ranajay Ghosh, Mohtada Sadrzadeh & Aloke Kumar, *Near wall void growth leads to disintegration of colloidal bacterial streamer*, Journal of Colloid and Interface Science, 2018. 522: p. 249-255"

4.1 Introduction

Bacterial streamers are filamentous biofilm-like structures that are usually known to form under sustained hydrodynamic flows [5]. Like biofilms, streamers consist of bacterial cells embedded in a matrix of self-secreted extracellular polymeric substances (EPS) and are excellent examples of soft materials of biological origin. Due to their morphology, streamers can colonize closed channels significantly faster than surface-hugging biofilms; recently streamers forming in very low Reynolds number conditions ($Re \lesssim 1$) have been implicated for their role in rapid fouling of biomedical devices [70, 79, 80], filtration units [39, 105] and even colonization of porous media [5, 6, 71]. In many of these applications, a better understanding of deformation, fracture and failure of streamers is crucial [105]. Valiei et al. [6] had reported failure and disintegration of streamers in microfluidic device, but this phenomenon was not discussed in detail. Das and Kumar [81] had investigated instabilities and break-up of streamers when they were idealized as highly viscous liquid jets. In a later work, Biswas et al. [105] utilized a microfluidic device with micro-pillars to investigate far-from-wall failures of streamers. They focused exclusively on 'thin' streamers, i.e. streamers whose aspect ratio (η), i.e. ratio of longitudinal to transverse characteristic length, is typically >10, and found that these streamers could fail through a necking like failure mode in steady flow typical of ductile materials under creep. They also found a power law relationship between the critical strain (strain at instability) and fluid velocity scale, which yielded valuable insights into material behavior. Recently, Hassanpourfard et

al. [106] showed that failure of streamers is not limited to the earlier stages but can also be found in the final clogged state of the device where localized failures lead to intricate water-channels coursing through the clogged biomass. Despite these studies, it is almost certain that more failure modes exist. This is because streamers like other biofilms represent a composite and extremely heterogeneous, active soft material. However, reporting and quantification of these phenomena is sparse.

One of the most fundamental challenges stems from the visualization issues since the EPS matrix embedding the microbe is very difficult to image due to its transparent nature. Furthermore, the nature of this type of set up results in several overlapping sources of nonlinearity in addition to failure and instability. These include creep behaviour of the polymeric EPS, fluid-structure interaction, moving interfaces and life processes, all of which cannot be independently controlled easily. In addition, timescale of streamer formation can vary considerably [6, 70, 71, 107] and very long-time scales can let significant changes in the background conditions affecting these nonlinear behaviours.

In this chapter, we report an entirely new type of streamer failure mechanism not observed before. This type of failure originates near the micropillar wall, rather than further downstream as previously noted, and yet distinct from shear failure at the micropillar wall typically seen at higher flow rates [105]. We use floc-mediated [71, 105, 106] rather than biofilm mediated [6, 70] streamer formation, where either of these refer to the mode of inception of the streamers [5]. Floc mediation allows for rapid streamer formation which helps us isolate mechanical factors and reduce streamer formation time thus

reducing biophysical complications such as cell division [71]. A microfluidic device was specially fabricated so as to allow streamers to freely form from micropillars into the downstream flow without any more attaching surfaces on the free side. Our imaging clearly showed that the inception of failure occurs with a pronounced void almost with the geometry of a small coin shaped crack near the point of attachment and only after the streamer structure was already well formed (i.e., when streamer length is several times the pillar characteristic length). Once this 'crack' was observed, it was found to rapidly extend resembling crack propagation quickly rupturing the streamer. We found this behaviour repeatedly, always originating near the pillars and only for some but not all streamers. This failure mode did not occur anywhere farther down the streamer length. The flow rate was kept constant for individual experiments. To the best of our knowledge, this is first report on this type of failure mode in streamers formed in microfluidic environments.

4.2 Results

When the *P. fluorescens* bacteria solution was injected through the microfluidic channel, streamers form downstream of the micro-pillars with a characteristic streamer formation timescale, t_{form}.

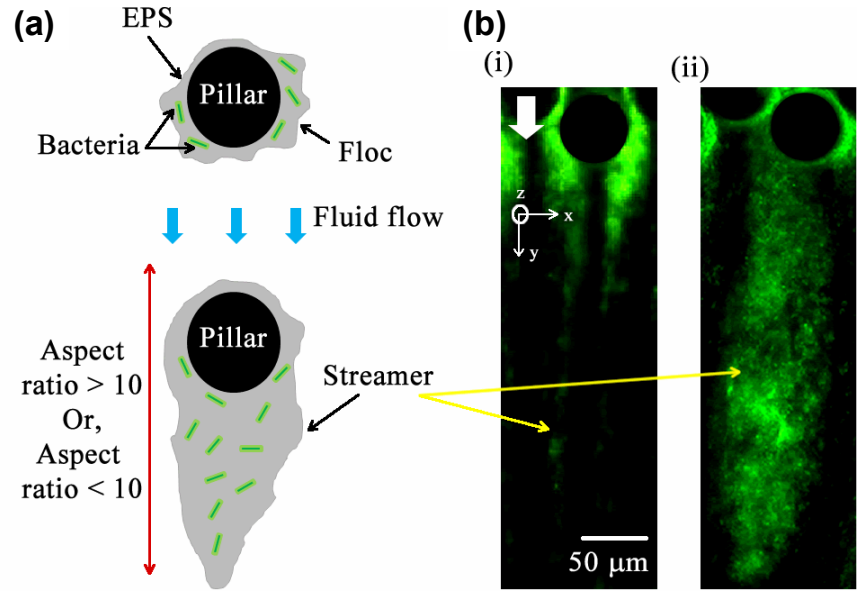

Figure 4.1: (a) Schematic of streamer formation. Bacterial flocs attach to the micropillars. Fluid flow generates traction forces that causes the biomass to extrude out in the form of filamentous structures i.e. streamers. In our chip design, one end of the streamer is attached to the pillar wall, while the other end extends downstream. (b) Green fluorescent microscopy images of i) thin streamer, aspect ratio > 10 and ii) thick streamer, aspect ratio < 10. The downward flow of fluid is indicated by the white arrow.

For a floc laden bacteria solution, as in this experiment, $t_{form} \sim O(10^{-1} - 10^{0}\ s)$. Streamer formation in these cases occurs because the flocs adhere to the micro-pillar walls and are rapidly sheared into the form of streamers by traction forces generated by the flow (Fig. 4.1 a). This mode of streamer formation has been investigated and characterized previously [71, 105]. Figure 4.1 b shows two different streamers formed in the device, when the bacteria solution was injected through the chip a constant volumetric flow rate (Q) by using a syringe pump. The corresponding global velocity scale, $U = \frac{Q}{(h \times W)}$, and Reynolds number, Re, were 3.75×10^{-3} m/s and $\sim 10^{-3}$

respectively. The two streamers differ in their morphology. The streamer marked '(i)' is an example of thin streamers, whose aspect ratio (ratio of longitudinal to transverse length) $\eta > 10$. The longitudinal and transverse length of a streamer is measured along the y-axis and x-axis respectively as shown in Fig. 4.1 b. The streamer marked '(ii)' is an example of a 'thick' streamer, $\eta < 10$. A constant flow rate is maintained for the entire duration of an experiment. After the streamers form, a quiescent period, t_0, is usually observed, where no significant deformation of streamers is observed. At the end of this time period, $t_0 \sim O(10^2 - 10^3\ s)$, subsequently noticeable deformation in the streamer mass can be observed often leading to the disintegration of streamer structure. One mode of failure is the already reported necking type failure prevalent far from the pillar wall [105]. However, yet another mode of failure was discovered in these experiments which occurred near the micro pillar wall, discussed below. Figure 4.2a depicts a composite confocal microscopy image of the void in streamer mass. This composite image was created by overlaying the image obtained using the two different filter cubes, and thus both bacteria (green) and PS beads (red) can be seen. As the time resolution of confocal microscopy imaging is comparable to the streamer deformation, Fig. 4.2 a can only yield qualitative insight into the geometry of the void. As we can see the void spans the entirety of the *z*-axis depth of the streamer and thus 'open' to the background flow.

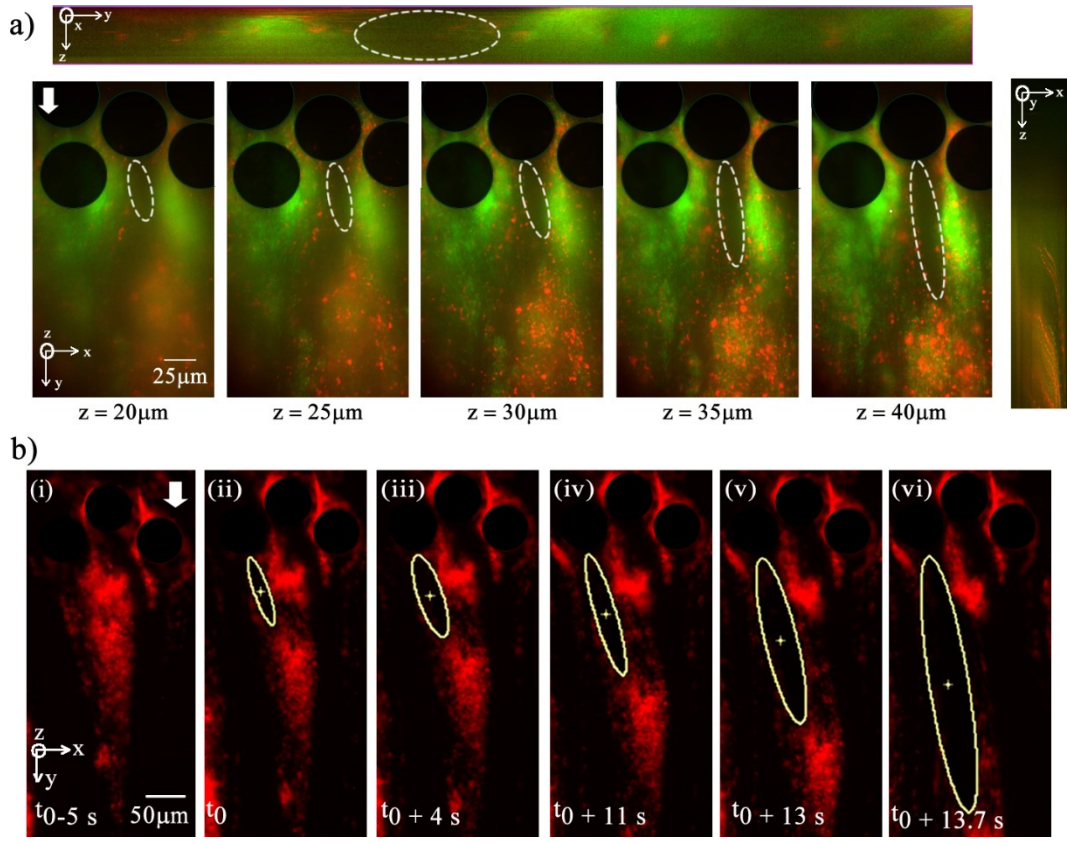

Figure 4.2: Fracture progression in a streamer a) Composite confocal slices of a void, showing that the void spans the height of the microchannel. Confocal sidebars show the *y*-*z* plane (top) and *z*-*x* plane (right). b) At mid-height a growing void is tracked by fitting ellipses. (i-vi) show progression of cavity. The global flow velocity is $U = 8.92 \times 10^{-3}$ m/s and t_0= 1 hour 11 minute.

Figure 4.2a also shows that the void geometry can be better approximated when imaging using the Texas Red filter cube is performed. The amine-coated PS beads being significantly smaller than the bacterium easily embed themselves in the EPS matrix, thus serving as useful markers [71, 105]. Since confocal microscopy does not allow us to investigate the shape of the void, for the rest of the investigation epi-fluorescence optical microscopy was utilized. In Fig. 4.2b, we show the moment of onset of a void in the streamer mass after approximately 71 minutes of initiation of the experiment. To ensure

that the proper void boundary is tracked by image processing algorithms, imaging was performed using the Texas red filter so that the 200 nm PS beads embedded within the EPS matrix are illuminated. Within the limits of optical microscopy and the microscale environment of the microfluidic channel, this allows for the best estimate of the boundary of the growing void. After the onset, the void grows rapidly with time both transversely and longitudinally although the latter being much more pronounced. Figure 4.2 b shows that the void grows with time eventually culminating its progress to the extremities of streamer leading to breakage.

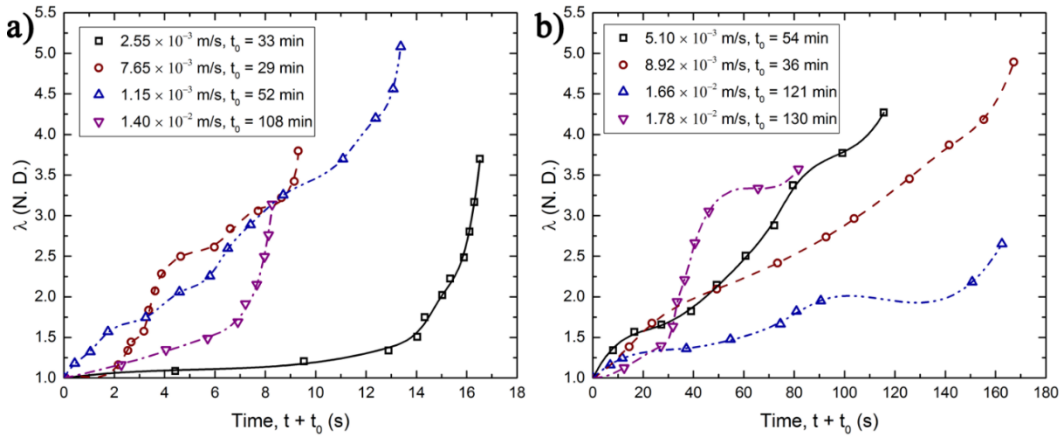

Figure 4.3: (a) λ versus time plot for short time scale fractures. Legend shows the velocity scale (U) and t_0 for the different cases. Markers indicate measured data and the lines represent B-spline fits. (c) λ versus time plot for long time scale fractures. Legend shows the velocity scale (U) and t_0 for the different cases.

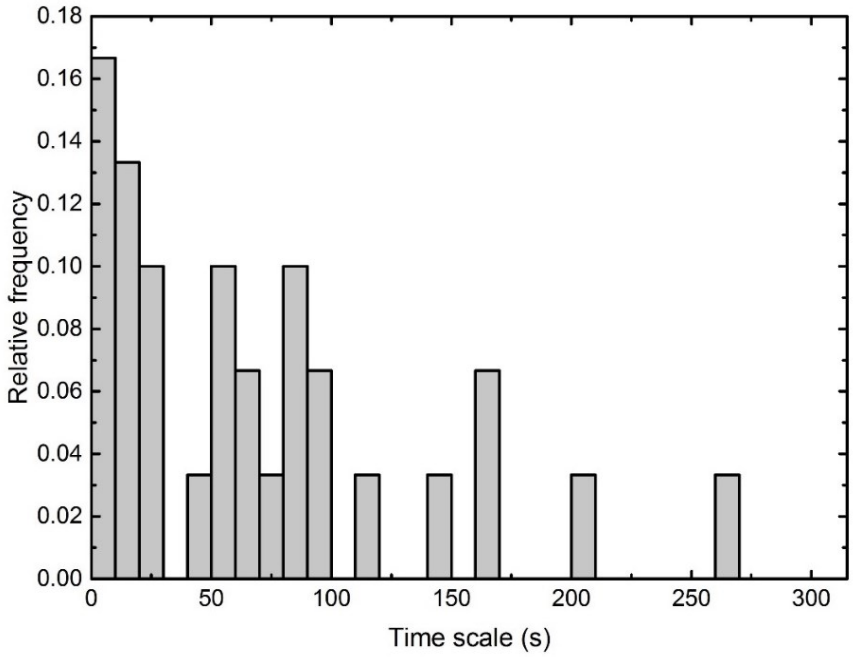

Figure 4.4: Relative frequency histogram of fracture time scales ($t_{fracture}$) observed in different experiments. A total of 31 different experimental data points are represented here.

To further quantify the breaking phenomena, we tracked the temporal growth the void. Figure 4.2 b also tracks the void and quantifies its deformation by fitting an ellipse to the growing cavity. To quantify the void we define, normalized crack length $\lambda = a/a_0$ where a_0 is the initial crack length and a is the current crack length (both measured along the ellipse's longitudinal axis). It is possible to associate with every failure event a fracture time scale ($t_{fracture}$). Although, there was a spread in $t_{fracture}$, it was possible to bin many of the events in two distinct sets. – one which occurs rather early in the life of streamer (small time-scale fracture-STF) and the other that is observed much later (long time-scale fracture - LTF). The relevant histogram is shown in Fig. 4.4.

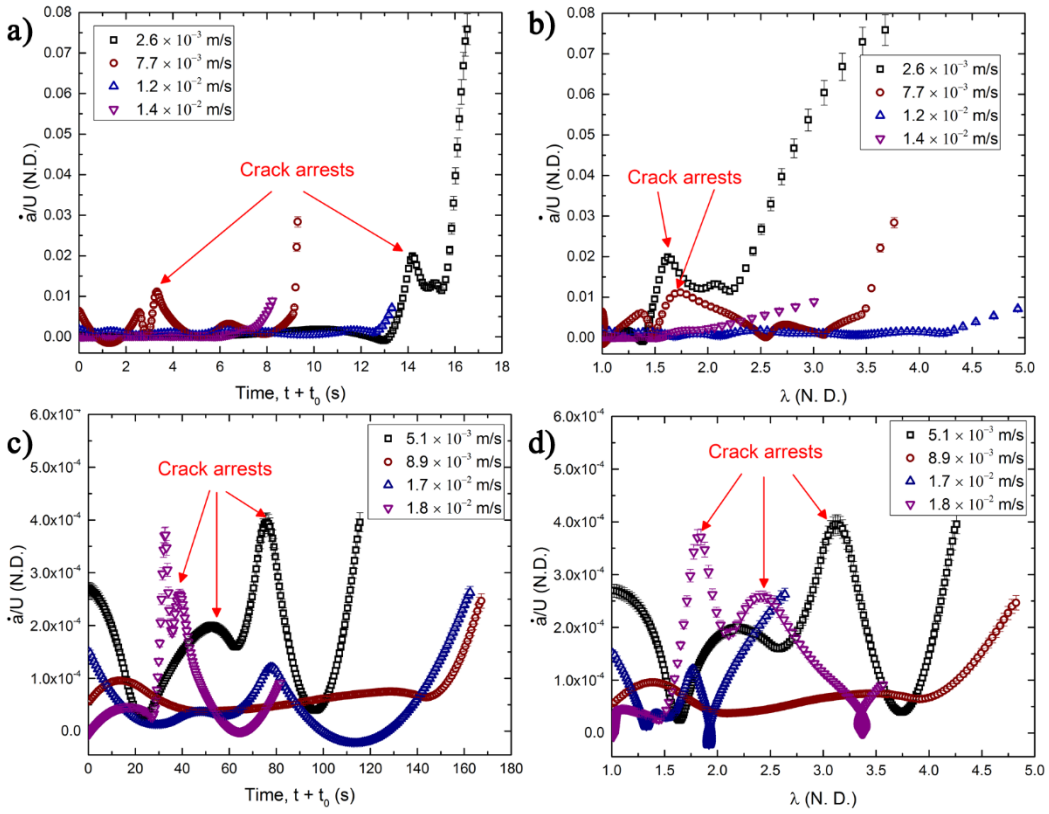

Figure 4.5: (a) Temporal variation of the normalized crack velocity ($\dot{a}/U$) for STF events. The legend indicates the value of U at which the (respective) experiment was conducted. (b) Variation of $\dot{a}/U$ versus λ for STF events. (c) Temporal variation of the normalized crack velocity ($\dot{a}/U$) for LTF events. (d) Variation of $\dot{a}/U$ versus λ for LTF events.

The STF events that occurred such that $t_{fracture} \sim O(10^1\ s)$ and their crack propagation dynamics is depicted in Fig 4.3 a. The LTF events occurred such that the set of fracture events occurred slower and for these events $t_{fracture} \sim O(10^2\ s)$ (Fig. 4.3 b). Fracture time-scales that lie in-between these two extremes were also observed, and similar crack-propagation behaviour was observed (data not shown). In addition to crack extension with time, we also plot crack propagation velocity normalized with background flow with time and crack length for both LTF and STF events. This is depicted in Fig. 4.5.

4.3 Discussion

This work highlights a hitherto unreported route of streamer disintegration – one starting right at the base of streamer near the pillar. It is interesting to note that the background fluid flow in the current problem would lead to a traction field in the crack propagation direction, which is not a very favourable crack opening force field. Therefore, by itself it is not the immediate cause of the instability. However, as the void is 'open', fluid can enter the void causing the crack propagation to occur. This explains why this form of instability is not found far from the wall since a steady source of fluid ingress is necessary. It also explains why this form of failure does not preclude the possibility of other types of far from wall failure modes since they are entirely independent modes of failure. At the same time, the success of crack propagation would also depend critically on the geometry of the initial void since it not only controls the tip stress conditions which can drive the crack but also the fluid variables inside the initial void. Therefore, the role of geometry of the initial flaw is even more important than traditional fracture propagation experiments. This double sensitivity to imperfections explains the relatively wide scatter in overall crack extension-time and crack velocity-time behaviour when flow conditions are changed even slightly even though the resulting traction filed may not be the immediate cause of instability as explained earlier. However, in spite of this difference, the crack propagation characteristics have some broadly similarities. For instance, from Fig. 4. 3(a) and (b), crack extension with time for both STF and LTF show similar nonlinear regimes of propagation for most of the observation– initial linear

part, followed by a plateau and thereafter a final catastrophic instability leading to complete disintegration of the streamer. This behaviour can be further analysed using crack propagation velocity plots, Fig. 4.5 a-d, which show an arresting behaviour after initial instability. For STF events, crack arrest events are evidenced in both crack length vs. time (Fig. 4.5), as well as, crack velocity vs. the normalized crack length (Fig. 4.5 b). Both of these figures show clearly marked peaks in velocity indicating crack arrest at an intermediate time. For LTF events, the crack arrest events become more frequent as multiple peaks in velocity (Fig. 4.5 c, d) are visible indicating repeated crack arrest after initial propagation. We describe these zones below.

The first zone is the initial crack propagation zone which marks the beginning of the instability and lengthening of the initial flaw. However, as soon as the instability begins likely due to accumulation of damage due to creep at the fracture tip, there is a decrease in crack propagation velocity with time leading to a plateau zone. Note that this plateau is more pronounced for the LTF than the STF. After some time, the plateau zone gives way to a final monotonic increase in crack length for both types of fractures leading to the final disintegration of the streamer. These plots clearly show that as the crack length increases, there is an initial resistance to the crack propagation. This behavior is also seen in many materials which is often a clear indication of nonlinear behavior at the crack tip [108-110]. This figure also shows that within these broad three-zone behaviors there are further intricacies such as multiple micro-regions of crack growth resistance in the plateau zone. However, in all cases, these resistance mechanisms finally fail to stop the crack, which then

transitions into the final runaway instability zone from which there is no recovery. The streamers ultimately disintegrate.

The broad reason for initial resistance to crack growth likely shares its physical origin to polymeric composite materials which results in overall similar behavior between LTF and STF behavior [111-113]. However, lack of clear trends in STF may indicate that these streamers may have much higher heterogeneity in their structure leading to more flaws, which precipitate the fracture early in their life. This would also explain why the initial crack propagation velocity is much higher for STF, Fig. 4.3 a, b which can be attributed to much weaker interfaces and flaws.

We refrain from developing a complete multiphysics model for this system in this communication since its validation would require more precise measurements of flow, material, and diffusive parameters.

4.4 Conclusion

In this chapter, we discovered a yet unreported failure mode of streamer disintegration which originated near the micro-pillar walls and is yet distinct from simple shear failure or tearing. This failure was observed to co-exist with other previously reported failure modes in streamers. This further supports the notion that this mode of failure is completely independent from previously reported data. We quantify the void/crack extension behavior using PS microbeads as tracers to aid microscopy and conclude that the crack is through the thickness of the streamer and its propagation is marked by very well defined three different zones of propagation. Breaking events occurred at various times

after the experiments began but two high-frequency zones characterized by a short time scale and another by longer time scales were clearly observed. It is unclear why failure inception is suppressed in the intermediate time scales. The crack/void propagation went through several cycles of propagation and arrest ultimately leading to a catastrophic disintegration/splitting of the entire streamer structure. This mode of streamer disintegration which occurs near the wall can have important implications in spreading of biomass downstream in filtration systems, porous media and biomedical devices.

Chapter 5 [?]

Impact of bacterial streamers on biofouling of microfluidic filtration systems

[?]The material in this chapter has been submitted to, "Ishita Biswas, Mohtada Sadrzadeh & Aloke Kumar, *Impact of bacterial streamers on biofouling of microfluidic filtration systems*, Biomicrofluidics, 2018 (Under review)".

5.1 Introduction

Membranes that are utilized in various filtration processes often face the problem of fouling, which is the unwanted accumulation of colloidal particles, organic matter, and biological substances on the membrane surface and/or within the membrane pores. Amongst the most common types of fouling is the biofouling, which occurs due to biofilm formation [27, 114-116]. Biofilms are matrix-encapsulated thin films of micro-organisms, where the matrix is usually formed by bacterial-secreted extracellular polymeric substances (EPS) [5, 117, 118]. Being a dynamic process, biofouling is indeed the most detrimental form of fouling and can contribute to as much as 45% of entire fouling process [114, 116]. Biofilm formation on membranes can lead to a host of issues including reduced membrane performance and longevity, as well as, low permeate flux and water quality, and subsequently increases operating costs [32, 119]. However, biofilm formation itself is also affected by the feed water properties (e.g., pH and ionic strength) [5, 10], the physicochemical properties of the surface (e.g., hydrophilicity and charge) [32, 120] and hydrodynamic variables (e.g., flow rate) [5]. Sustained hydrodynamic flows over biofilm can elucidate the complex and time-dependent viscoelastic responses from the biofilm soft matter, and one such response is the formation of filamentous structures called 'streamers'[5, 71, 105, 106]. Unlike regular biofilms, streamers have a string-like morphology, which are tethered at one or both ends to walls, while the rest of the structure can extend significantly with the flow [5]. This feature allows wide-spread colonization, decreasing the membrane's performance as a result.

Microfluidic membrane-mimics [38, 39, 105] are natural platforms for investigating the effect bacterial streamer formation in low Reynolds number conditions. Membranes in microfluidic systems have been a growing area of research interest [121, 122] as microfluidic systems can capture the various length scales that occur in biofouling and filtration membranes and are also amenable to real-time optical microscopy as well as other analytical techniques [5]. For instance, Marty et al. [39] designed a microfluidic device to mimic a membrane system and showed that significant bacteria cell accumulation and streamer formation in the downstream area occur during filtration. They studied the effect of different pore-sizes and filtration modes, (dead-end and pseudo cross flow) on the lengths of streamers and reported that smaller pore-sizes and low flow rates promoted streamer formation in the microfluidic membrane-mimic system. The formation of streamers in the downstream section of the filtration unit stands in contrast to some reports of mass accumulation in inorganic fouling [67]. In another study, they reported the effects of pore tortuosity and secondary flows on streamer formation as well [38]. Biswas et al. [105] studied the deformation and failure behavior of bacterial streamer in a membrane-type porous system. They discovered instability in the streamers, like deformation regimes, as they transitioned slowly through complex creep, and ultimately underwent failure. The studies related to the microfluidic membrane-mimics would have been more interesting if the connection between the dynamics of streamer formation and the transport through membrane pores had been explored. Recent investigations, particularly those utilizing the porous microfluidic mimic platforms [6, 71, 105, 106], indicate that, during experiments, there are at least two distinct time phases

of streamer formation: the initial phase when the streamer forms and second phase that occurs after the initial streamers have formed. The dynamics of streamers post formation are important because, upon completion of the initial formation, the streamers undergo a rapid mass accrual mainly due to their 'web' like structures. During this phase, they can completely clog the system [6, 71], undergo a catastrophic nonlinear deformation [105], or suffer localized failure leading to an extended water channel throughout the system [106]. Despite these studies, both the formation and impact of biofilm streamers in natural habitats and artificial environments remain sparsely investigated[5]. Significantly, the time-dependent deformation tendency of bacterial streamers in creeping flows (Reynolds number, $Re << 1$) can have important implications for filtration systems and yet only few studies till date have focused on this issue.

In this chapter, we report an *in-situ* observation of post formation dynamics of bacterial streamers by using a pressure-driven microfluidic platform that is designed to operate in the dead-end filtration mode [116]. The device has a 2 µm pore size to mimic the microfiltration membranes that are most commonly used for filtering out biological substances [116]. Bacterial streamers were formed in the channel by using a solution laden with bacterial flocs – a previously studied and characterized mode of streamer formation [71, 105, 106]. In our work, we focused on the post-formation dynamics of streamer formation, i.e. the time period following the formation of the streamer, and observe rapid clogging of the system because of streamer formation. This clogging results in an exponential decrease in flow-rate through the device. We find that superimposed on this exponential decrease are smaller time-scale

fluctuations in flow rate, which coincide with deformation/breaking of streamers. Moreover, de-clogging of pores, deformation and breaking of the streamer occurred, leading to the transport of bacterial biomass into the permeate. We also found that there exists a lower bound on the applied pressure difference below which streamer based clogging is not dominant. We further investigated the effect of pH on the filtration system.

5.2 Results and discussion

Our microfluidic filtration system was designed to operate in the dead-end mode (Fig. 2.9). In this filtration mode, a pressure difference across the membrane causes the feed to flow through the filtration zone and the foulant materials thus accumulate around the pore-walls. As discussed earlier, the pitch length (p) or the pore-length scale of the filtration zone was 2 µm. Figure 5.1 (Also Fig 2.3) shows the minimum gap among the PDMS micropillars. A small aspect ratio of $5:1$ for the pillar height and pore-size was considered to avoid collapse of PDMS pillars [123-125]

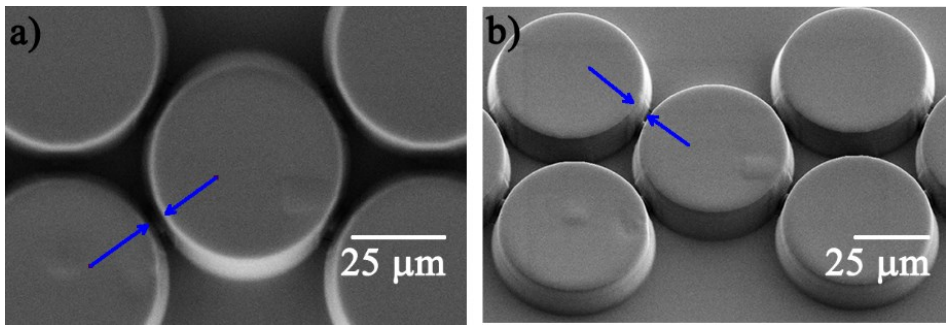

Figure 5.1: FESEM image of PDMS chip (a) top view and (b) side view of the gap between pillars. The indicated gap is approximately 2 µm.

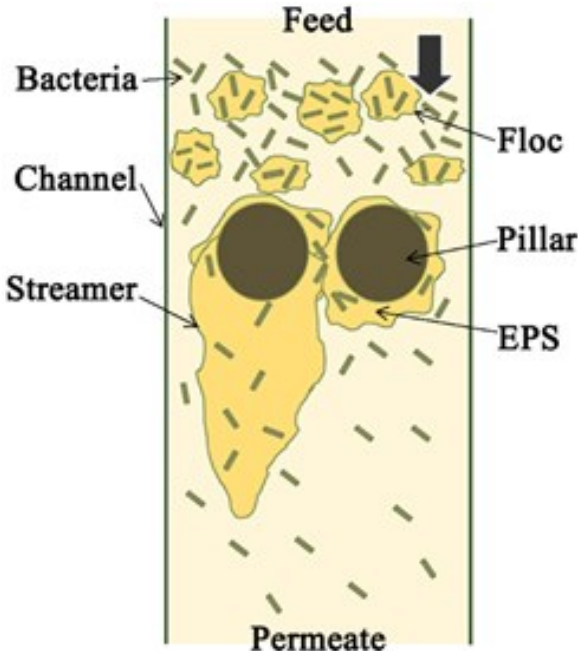

Figure 5.2: Schematic of the biofouling process and streamer formation around the micro-pillars.

This pore size is in the range of a typical microfiltration membrane, where the pore length scale lies between 10^{-1} µm and 10 µm. Microfiltration membranes are widely used to remove biological matter from contaminated water [116, 126, 127]. In the work discussed here, all experiments were performed under constant applied pressure through the microfluidic membrane-mimic system. To conduct a parametric study on the influence of the applied pressure difference (ΔP), the pressure difference was varied from 5 psi to 25 psi. For each experiment, a diluted solution of bacterial flocs was used as feed (Fig. 5.2). The clean fluid that passes through the membrane because of the pressure gradient across the pillar array is referred to as the permeate. The streamers form on the downstream side of the device, which also represents the permeate side. Previous reports have established that bacterial flocs lead to

rapid-streamer formation in the microfluidic systems, thus providing a suitable experimental method to evaluate the impact of streamers on various systems [71, 105, 106].

The flocs in the feed attached to the pillar walls inside the device causing biofouling and the fluidic loading caused them to stretch out in the form of the thin filaments viz., streamers. Figure 5.3 shows the impact of biofouling and streamer formation in the filtration zone of the microfluidic device. Initially, we performed a control experiment where PBS, without any bacterial cells, was used as a feed liquid and a constant pressure of 20 psi was applied across the microfluidic channel. The resulting temporal variation of the flow rate (Q) is shown in Fig. 5.3 a.

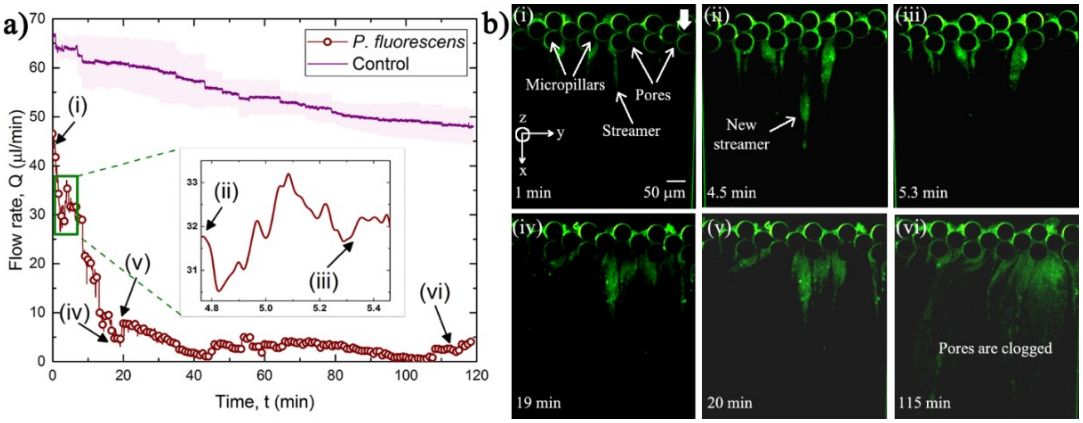

Figure 5.3: a) The variation of flow rate (Q) with time (t) at constant pressure difference, $\Delta P = 20$ psi. The control experiment with PBS is also plotted and shaded portion shows the error during experiment. Q decreases due to rapid pore-blockage by streamers. (Inset) Short time-scale (~O (10^0 seconds)) fluctuations can also be seen, which occur due to de-clogging of the pores. b) Optical microscopy images of entire width on the channel along with the pore-scale phenomena corresponding to the time-points delineated by roman numerals in '(a)'.

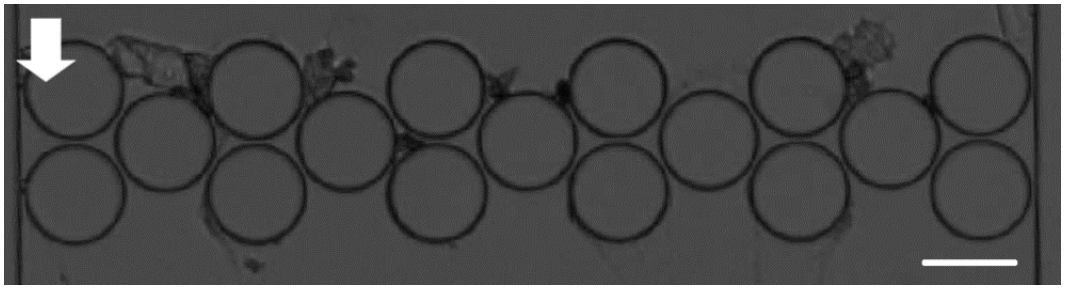

Figure 5.4: Optical microscopy image (brightfield) of the chip after 2 hours completion of the control experiments with PBS. White arrow shows the flow direction. The scale bar is 50 µm.

Although no bacterial cell was present in the PBS fluid, some debris would inevitably accumulate at the pore-space during the experiment (Fig. 5.4) leading to a decrease in flow rate. When the bacterial solution is used as feed, bacterial biomass causes clogging of the pore-spaces in the filtration zone. In the case of 20 psi pressure difference, the resulting flow causes streamer formation in the device and in such situations Q decreases sharply with time; a representative graph is shown in Fig. 5.3 a. The initial flow rate of 46 µl/min decreases to almost 0 µl/min after approximately 100 minutes of the experiment. Florescent microscopy images corresponding to certain temporal points (marked in roman numerals) are shown in Fig. 5.3 b. It must be noted that only visible biomass corresponds to fluorescing bacteria and EPS is not visible under fluorescent imaging.

As the flow is initiated, biofouling of the filtration zone and streamer formation occurs almost immediately (~1 minute). After several minutes, streamers become thicker, i.e., their y-axis span increases, and they extend for ~ 200 µm from the micro-pillar posts. Streamers are formed from strongly viscoelastic biomass and can undergo phenomena such as creep and failure.

Failures and breakage of streamers was observed to cause short-time scale ($\sim 10^1$ seconds) fluctuations in the flow rate. The inset of Fig. 5.3 a captures such an instance when Q increases sharply because of partial de-clogging of the pore-space. Such fluctuations coincide with de-clogging of pore-space when some biomass detaches fully or partially from the filtration zone. Partially detached biomass is stretched by shear forces leading to streamer formation, while complete detachments lead to biomass entering the post-filtration zone into the permeate. Biswas et al. [105] have shown that bacterial biomass show strong material non-linearity and a complex creep response; these responses likely contribute to this phenomenon. The short time-scale ($\sim 10^1$ seconds) enhancements in Q do not affect the long-time ($\sim 10^1 - 10^2$ minutes) decay behavior because of the continuous accumulation of biomass at the filtration zone.

To assess contamination of the permeate due to streamer breakage and filtration efficiency, we quantified the optical density at 600 nm (OD_{600}) of the permeate. Figure 5.5 a shows the change of OD_{600} of the permeate as a function of time for two different applied pressures. As can be seen, the optical density of permeate increases for about 60 minutes, after which it shows a decreasing trend. This initial increase is likely due to the streamer breakage events, which generate biomass debris and subsequently contaminates the permeate. Biswas et al. [105] have reported such failure events, which occur due to the creep response of the bacterial soft matter. After the initial increase, the flow rate decreases substantially, which should result in a corresponding decrease of streamer breakage events (as shear forces decrease).

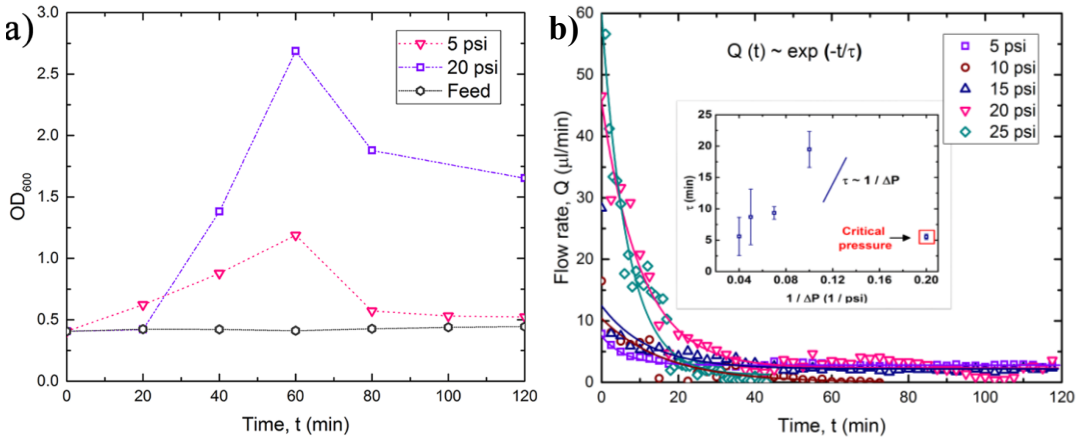

Figure 5.5: a) Optical Density (OD_{600}) of feed solution and permeate plotted at two different pressure differences (ΔP) of 5 psi and 20 psi. b) Change of flow rate (Q) with t at different ΔP. The markers represent experimental data, whereas the lines represent exponential curve fits. (Inset) The time-scale (τ) obtained from the regression fit is plotted against ΔP. With the exception of τ corresponding to $\Delta P = 5$ psi, τ shows a linear scaling with $\frac{1}{\Delta P}$.

This should result in a decrease of OD, which is also observed in the latter half of the experiment (Fig. 5.5 a). Such a decrease in OD can also be attributed to the common cake filtration in membrane process where the pore blockage and formation of a cake layer of foulant contribute itself to the separation of contaminants [126, 128]. Moreover, it is clear that the permeate is substantially more contaminated at a higher operating pressure difference. Figure 5.5a also shows the change the of OD_{600} of the feeding sample for 2 hours. However, the change of OD_{600} was insignificant compared to the permeate OD_{600} as can be seen in Fig. 5.5 a. Therefore, the effect of room temperature in growing these bacteria was neglected. To further explore the role of the operating pressure difference (ΔP), we conducted filtration experiments for a range of applied pressure differences. Applied transmembrane

pressure for a typical microfiltration process is in the range of 1.5 psi - 29 psi [116, 129]. Hence, in the present work, the performance of microfluidc membrane system is investigated from 5 psi to 25 psi pressure. The resulting temporal variation of flow rates for these ΔP values is plotted in Fig. 5.5 b. The long-time scale behaviour of the flow rates obeys an exponential decaying trend, i.e,. $Q\ (t) \sim Ae^{\left(\frac{-t}{\tau}\right)}$, where, A is a constant and τ is the decay time-scale, for different ΔP. Table 5.1 shows the exponential decay equation and corresponding values of the parameters that uses in Fig 5.5. This exponential decay behaviour was extremely repeatable (Fig. 5.6). The inset of Fig. 5.5 b depicts the change in the decay time-scale (τ) as a function of the applied pressure difference.

Table 5.1: The exponential decay equation and the corresponding values of the parameters for different pressure difference. The table corresponds to fits shown in Fig. 5.5 b.

$Q = Ae^{\left(\frac{t}{\tau}\right)} + A_0$				
ΔP (psi)	τ (min)	A	A_0	R^2 (Goodness of fit)
5	6.14	4.75	2.80	0.92
10	16.61	10.40	0.02	0.87
15	12.29	10.28	2.19	0.81
20	10.26	43.33	2.33	0.94
25	6.68	58.64	1.20	0.93

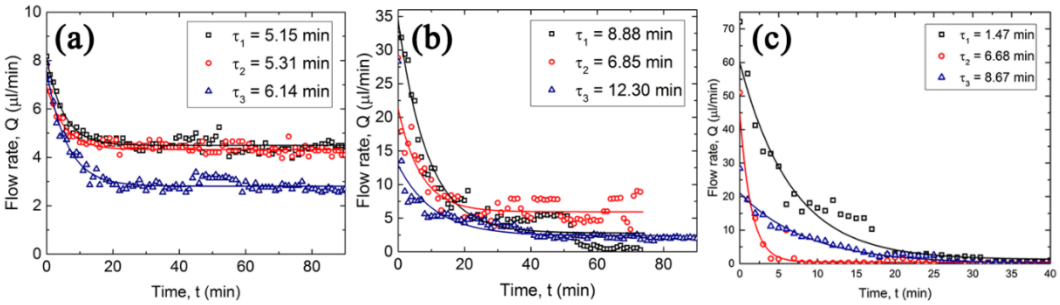

Figure 5.6: (a) Repeatability experiments for $\Delta P = 5$ psi (b) Repeatability experiments for $\Delta P = 15$ psi. and (c) Repeatability experiments for $\Delta P = 25$ psi.

Interestingly, the decay time-scale has a linear relation with the inverse of applied pressure difference, i.e., $\tau \sim \frac{1}{\Delta P}$, with the exception of data for $\Delta P = 5$ psi. This trend agrees well with the theoretical models for streamer based clogging proposed by Drescher et al. [70] and Das and Kumar [81]. Thus, $\Delta P = 5$ psi can also be treated as a critical pressure difference below which streamer based clogging is not dominant. For pressure differences greater than 10 psi, streamer based clogging dominates the system. In membrane studies, the critical flux is defined as the permeate flux above which an irreversible foiling occurs. In general, operation at sub-critical region (below the critical flux) is desired as no fouling occurs and the membrane functions in an entirely clean regime [130, 131]. The critical flux in our microfluidic membrane-mimic system is calculated by using $(Q/(W \times h))$, where, Q is flow rate ~ 5 µl/min, W, width of the channel, is 364 µm and h, height of the pillars, is 10 µm. The approximate critical flux for this system is $\sim 8.2 \times 10^4$ L/m^{2}hr (or LMH). This observation provides a valuable insight into the proper operating pressure for microfiltration membranes with ~ 2 µm pores size when applied to removal of bacteria and bacterial biomass. Higher initial flux does not necessarily result in

optimum production as it leads to more frequent cleaning. Hence, it is important to not exceed $\sim 8.2 \times 10^4$ LMH as this is counter-productive and increases overall cost in long term. In filtration systems, pH of the feed is an important experimental variable, as it can strongly affect deposition on membranes, fouling potential, and performance of membranes [116, 120, 132].

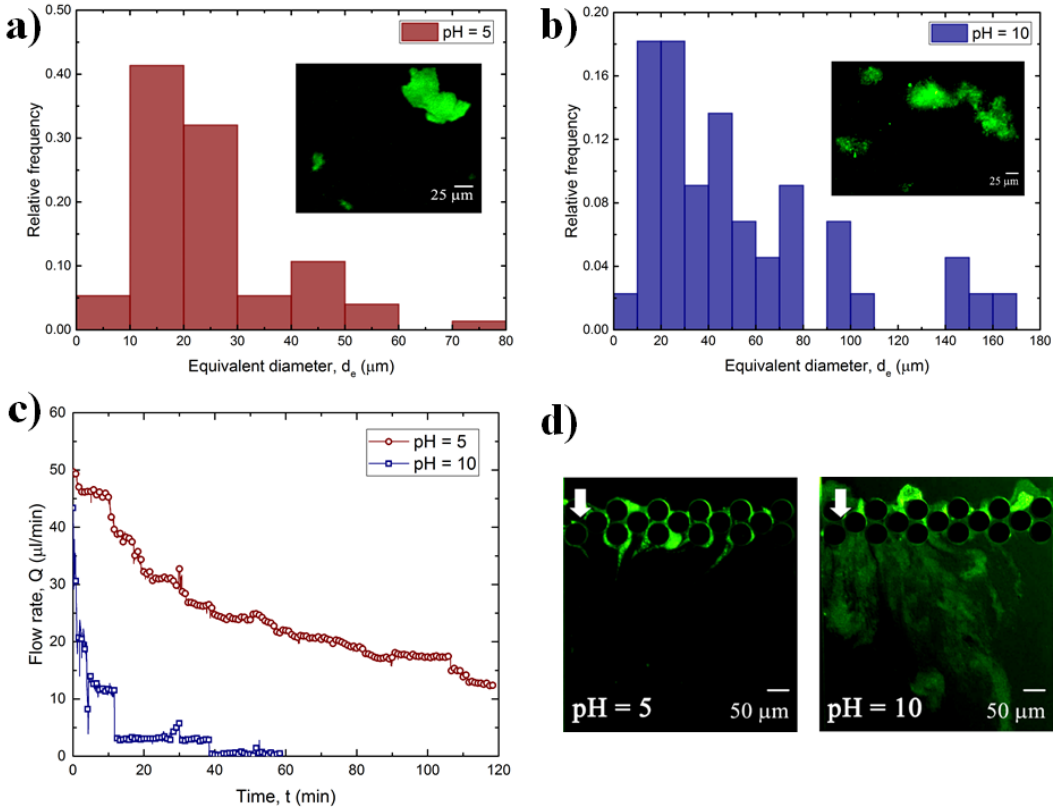

Figure 5.7: Histograms for the equivalent diameter (d_e) of flocs at a) pH $=$ 5 and b) pH $=$ 10. The total number of flocs considered are 60 and 46 and the medians are 21 μm and 41 μm at pH $=$ 5 and pH $=$ 10 respectively. Inset images show two sample flocs imaged using optical microscopy. c) Comparison of the flow rate (Q) with time (t) at different pH conditions under constant $\Delta P = 20$ psi. d) Fouling at the filtration zone for the two different pH conditions at time 50 minute. The white arrow show that the flow direction is from top to bottom.

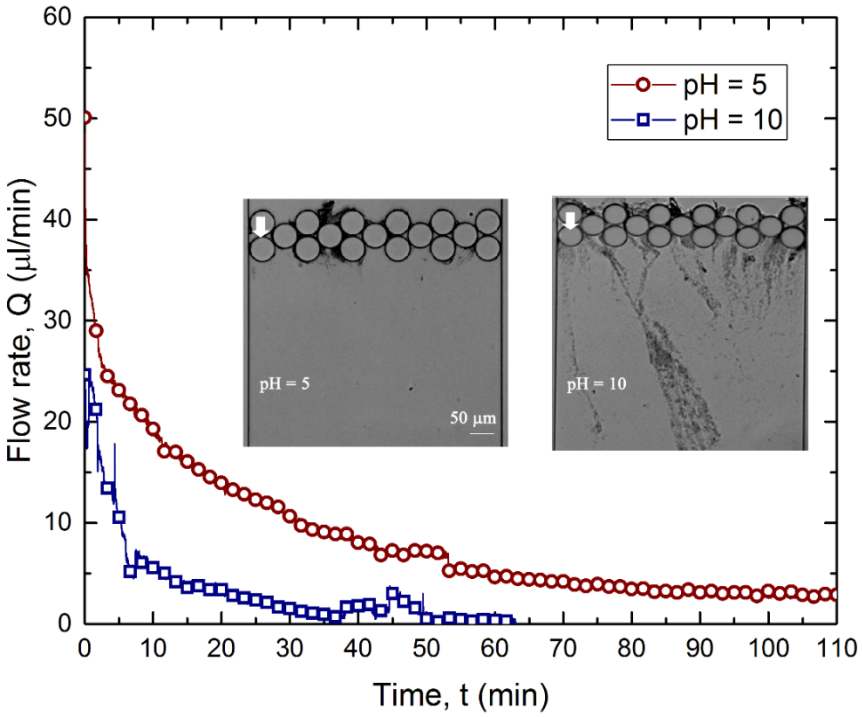

Figure 5.8: Comparison of the flow rate (Q) with time (t) at different pH conditions under constant $\Delta P = 20$ psi using *P. aeruginosa* bacteria. Inset images show fouling at the filtration zone for the two different pH conditions after 50 minutes of initiation of the experiment. The white arrows show the flow direction (top to bottom).

In order to assess the impact of pH, we carried out further experiments by changing the pH of the feed media. Prior to the microfluidic experiments, the effect of pH on floc size was assessed. Fig. 5.7 a, b depict the *P. fluorescens* floc diameter histograms for the acidic (pH = 5) and alkaline (pH = 10) environments, respectively. For pH = 5, the average floc diameter was found to be approximately 21 µm, whereas for the alkaline environment (pH = 10), it was found to be 42 µm. Hence, we can see that pH clearly affects bacterial behaviour, and we can expect pH to affect biofouling of the membranes. Fig. 5.7 c shows the temporal change in Q at two different pH values under constant applied pressure difference of 20 psi. For the highly alkaline feed solution (pH

= 10), the membrane becomes almost completely clogged and the flow rate decreases to practically zero after approximately 60 minutes of operation. However, for the acidic feed (pH = 5), membrane continues to operate well beyond 120 minutes from the initiation of the experiment.

This observation is also corroborated by visualization of the filtration section (Fig. 5.7d), which compares the filtration zone for two different pH conditions. The similar behaviour was observed when we used *P. aeruginosa* bacteria in the feed solution (Fig 5.8). Compared to the highly alkaline feed, the acidic feed causes significantly less biofouling. This significant variation in biofouling under different pH conditions likely occurs due to higher EPS secretion under alkaline conditions [133, 134]. Based on these findings, in a membrane application, the pH of the feed solution must be adjusted to acidic condition before treatment. This pre-treatment of feed water significantly reduces the risk of abrupt membrane clogging and thus replacement of membranes.

The exact mechanism by which pH affects the bacterial floc size is not known. However, it is well known that the EPS matrix is composed of biopolymers such as polymeric sugars, nuclear acids, proteins and lipid [135]. Literature suggests that EPS of gram-negative bacteria often contain charged carboxylate groups [135]. It is likely, that at low pH these carboxylate groups are neutralized through protonation, which can cause the contraction of floc/ biofilm and reduction the thickness. It has also been observed that the increase of pH can swell up the EPS [136] and lead to a higher biofilm/ floc formation [137]. Perhaps, future studies can focus on this aspect.

5.3 Conclusion

In conclusion, our work shows that the post-formation dynamics of bacterial streamers can affect filtration efficiency in a microfluidic membrane-mimic system. We investigated the effect of de-clogging of the pore-space and the streamer failure on the quality of the permeate. Partially-detached biomasses result in new streamer formation in the device, while fully de-clogged biomass is transported into the permeate. Streamer formation and clogging dynamics were strongly dependent on the applied pressure difference. We found that when streamer based clogging dominates, then the permeate flux exponentially decreases with time. A critical pressure difference was also found below which streamer-based clogging did not dominate. We also found that the pH of the feed can affect bacterial biomass and can affect biofouling of the membrane. We observed that acidic feed can increase the permeate flux compared to the highly alkaline feed, thus the biofouling under the acidic condition is lesser. Thus, the post-formation dynamics of bacterial streamer being a very complex process, can be affected by many factors and yet to be understood.

Chapter 6

Conclusion and future work

6.1 Conclusion

The formation and post-formation dynamics of bacterial streamer have a severe impact on the microfluidic filtration system. In this dissertation, a microfluidic device has been proposed to observe and analyse the post-formation dynamics of bacterial streamers and also this device can mimic the microfiltration membrane. The deformation and failure of bacterial streamers has been observed at constant background flow velocity and pressure gradient.

In Chapter 3, the deformation and failure behaviour of bacterial streamers for two separate bacterial strains, under low Reynolds number flow, have been studied and discovered highly localized failure of the bacterial streamers. Three distinct phases were observed. In the first phase, the streamer formed soon after the experiments start. The streamer then takes time to get a full shape by accruing biomass from the system. After passing through a quiescent period, the formed streamers slowly goes into a complex creep like deformation regimes with their characteristic time scales despite stable background flow conditions. In the final stage, the significant deformation occurs due to high strains over relatively small time scales. Moreover, streamer recoil observed after the flow was stopped at the onset of instability which confirmed residual elasticity. More interestingly, different streamers at different flow conditions broadly showed the distinct deformation regimes and the failure behaviour of the streamers. It has also been observed that this behaviour was typical between streamers of two separate bacterial strains. This mode of failure occurs far from the wall of the system. A simplified nonlinear mechanical model has been developed for the failure behaviour assuming necking failure of the

streamers. This model matches remarkably well against the rupture scaling obtained from the experiments.

In Chapter 4, a different type of failure mode of bacterial streamer has been discovered that shows a void/ crack formation inside the streamer material and goes to considerable deformation. This failure was observed to co-exist with other previously reported failure modes in streamers. The void/crack extension behaviour was quantified and concluded that the crack is through the thickness of the streamer and its propagation is marked by three different zones of propagation. Short and longer time scales for occurring the breaking events were characterized. The crack/void propagation went through several cycles of propagation and arrest ultimately leading to a catastrophic disintegration of the streamer. This mode of streamer failure occurs near the wall of the system. This type of failure can have significant implications in spreading of biomass downstream in filtration systems, porous media, and biomedical devices.

In Chapter 5, the post-formation dynamics of bacterial streamers has been studied in a microfluidic filtration system. A microfluidic device was designed with 2 µm pore size to mimic the microfiltration membrane. A pressure-driven dead-end filtration set-up was utilized to analyse the biofouling behaviour in the filtration system. It was discovered that the bacterial streamer has great impact on the biofouling during filtration. The effect of de-clogging of the pore-space and the streamer failure on the quality of the permeate have been identified. Partially detached biomasses result in new streamer formation in the device, while fully de-clogged biomass is transported into the permeate. It was also found that streamer formation and clogging dynamics were strongly

dependent on the applied pressure difference. Due to streamer based clogging, the permeate flux exponentially decreases with time. A critical pressure difference was also found below which streamer-based clogging did not dominate. The pH of the feed can affect bacterial biomass and biofouling of the membrane. The acidic feed can increase the permeate flux compared to the highly alkaline feed. Thus the biofouling under acidic condition is lesser. Thus, the post-formation dynamics of bacterial streamer being a very complicated process can be affected by many factors and remains to be understood.

6.2 Future work

The studies in chapter 3 and 4 can be extended to explore the effect of pH on the input bacterial solution. As mentioned earlier the EPS matrix is composed of biopolymers such as polymeric sugars, nuclear acids, proteins and lipid. Literature suggests that EPS of gram-negative bacteria often contain charged carboxylate groups. It is likely that at low pH these carboxylate groups are neutralized through protonation, which can cause the contraction of floc/ biofilm and reduce the thickness. It has also been observed that the increase of pH can swell up the EPS and lead to a higher biofilm/ floc formation. If the formation dynamics of bacterial streamers alters because of the EPS nature, it can impact the post-formation dynamics. Figure 6.1 shows a preliminary results that have been observed by changing pH of the input solution. *P. fluorescens* bacteria solution was mixed with 200 nm polystyrene beads. At pH= 5, there was no noticeable floc formation were observed (Fig 6.1a) and at higher pH, 10, the system was clogged (Fig 6.1b).

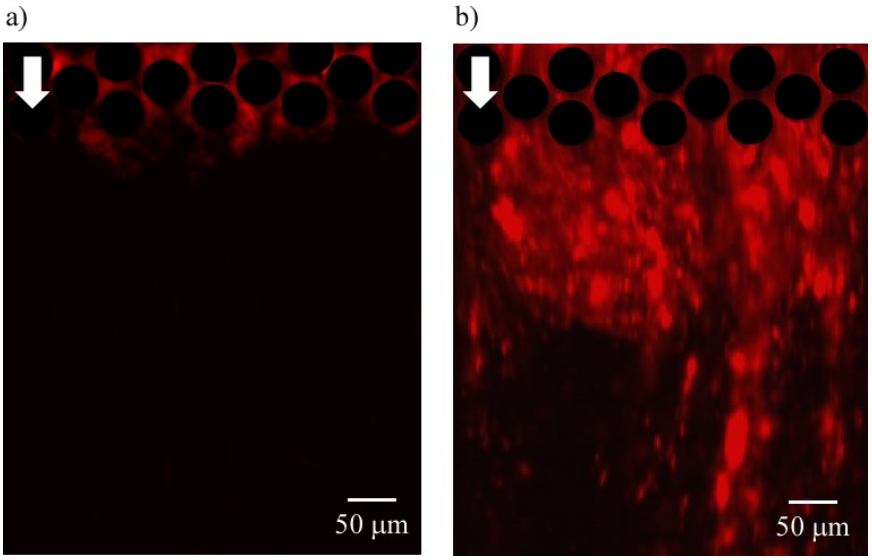

Figure 6.1: Streamer formation at (a) pH = 5 and (b) pH = 10. The white arrows show the flow direction in the channel.

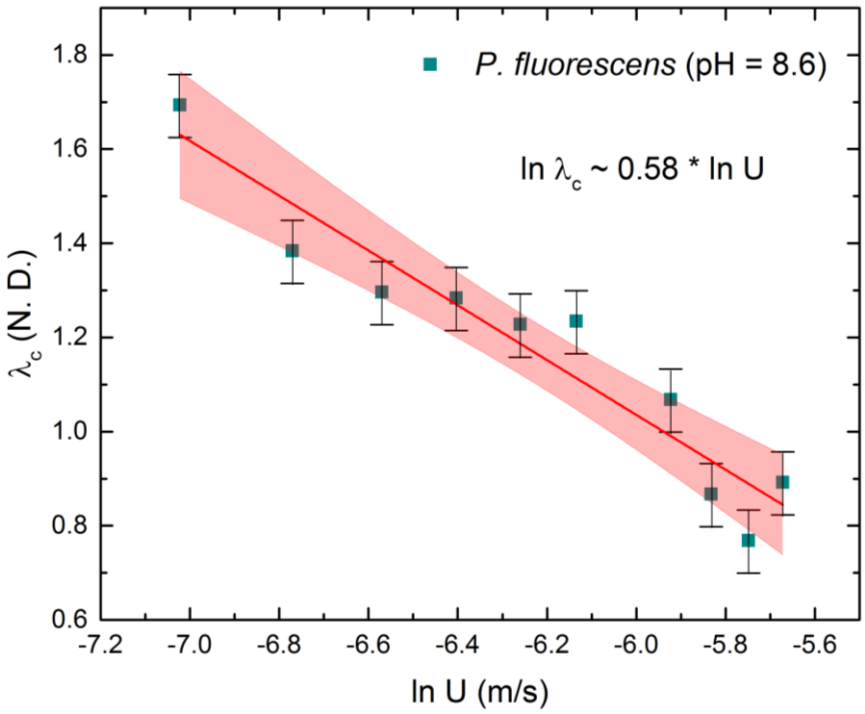

Figure 6.2: $\ln \lambda_C$ for different flow rates for for *P. fluorescens* streamers show a similar scaling with $\ln U$. The brown squares represent experimental data and the red line represents a linear regression fit.

Figure 6.2 shows a preliminary result for the relation of critical stretch ratio and flow velocity at pH = 8.6. By changing the pH we were able to recover a similar power law, $\lambda_C \sim U^{\alpha}$ with $\alpha = -0.58$, that have been discussed in Chapter 3. However, more experimental data points at different pH are needed to draw a conclusion. Future studies can focus on this aspect.

Floc or Biofilm formation itself is also affected by the fluid properties i. e., ionic strength. Investigation of breaking of streamer by changing the ionic strength of the fluid could be another study. On the other hand, the failure of bacterial streamers in creeping flows can be hard to analyze because their growth are hard to control. The breaking phenomenon can be analyzed with abiotic streamers, which forms due to the aggregation of colloidal particles and polymers in a creeping flow regime [138].

The studies in chapter 5 can be extended, by altering the physicochemical properties of the surface of PDMS, e.g., hydrophilicity and charge. The work was inspired to see the impact of streamer failure in membrane filtration system. The PDMS microfluidic device was fabricated to mimic the microfiltration membrane. The change of surface property of the PDMS could change the morphology and dynamic behaviour of streamers in the system. The use of other types of polymer such as PMMA, polyamide, and polycarbonate instead of PDMS can be used to make the microfluidic device. These polymers are commonly used to fabricate the membrane.

Another study could be focused on the change of pore size of the microfluidic device. In the current study, photolithography was used to fabricate the microfluidic device. Due to the limitations of photolithography only a 2µm minimum pore size could be fabricated. However, there are other

fabrication techniques i. e. electron beam lithography and ion beam lithography to pattern nanochannels and pores for smaller sizes if further studies require it.

6.3 List of contributions

The outcomes of this research are submitted, published and presented in the following book chapter, journals and conferences:

6.3.1 Book chapter

1. Ishita Biswas, Aloke Kumar & Mohtada Sadrzadeh, Microfluidic membrane filtration systems to study biofouling", in the book "Microfluidics and Nanofluidics", Intech open science. ISBN 987-953-51-5997-1 (in press)

6.3.2 Journal papers

1. Ishita Biswas, Ranajay Ghosh, Mohtada Sadrzadeh & Aloke Kumar, Nonlinear deformation and localized failure of bacterial streamers in creeping flows". Scientific Reports, 2016. 6: p. 32204.
2. Ishita Biswas, Ranajay Ghosh, Mohtada Sadrzadeh & Aloke Kumar, Near wall void growth leads to disintegration of colloidal bacterial streamer, Journal of Colloid and Interface Science, 2018. 522: p. 249-255.

3. Ishita Biswas, Mohtada Sadrzadeh & Aloke Kumar, Impact of bacterial streamers on biofouling of microfluidic filtration systems, Biomicrofluidics, 2018 (Under review)

6.3.3 Conference presentations

1. Ishita Biswas, Ranajay Ghosh, Mohtada Sadrzadeh and Aloke Kumar, nonlinear deformation and localized failure of bacterial streamers in creeping flows, XXIV ICTAM, 21-26 August 2016, Montreal, Canada
2. Ishita Biswas, Ranajay Ghosh, Mohtada Sadrzadeh and Aloke Kumar, Failure of bacterial streamer in creeping flows, American Physical Society Division of Fluid Dynamics, 69th Annual Meeting November 20-22, 2016 Portland, Oregon, USA

References

1. H.-C. Flemming, et al., *Springer Series on Biofilms.* 2009. **4**.

2. Komlenic, R., *Rethinking the causes of membrane biofouling.* Filtration & Separation, 2010. **47**(5): p. 26-28.

3. Bixler, G.D. and B. Bhushan, *Biofouling: lessons from nature.* Philos Trans A Math Phys Eng Sci, 2012. **370**(1967): p. 2381-417.

4. Stoodley, P., et al., *Biofilms as complex differentiated communities.* Annu Rev Microbiol, 2002. **56**: p. 187-209.

5. Karimi, A., et al., *Interplay of physical mechanisms and biofilm processes: review of microfluidic methods.* Lab Chip, 2015. **15**(1): p. 23-42.

6. Valiei, A., et al., *A web of streamers: biofilm formation in a porous microfluidic device.* Lab Chip, 2012. **12**(24): p. 5133-5137.

7. Hall-Stoodley, L., J.W. Costerton, and P. Stoodley, *Bacterial biofilms: from the natural environment to infectious diseases.* Nat Rev Microbiol, 2004. **2**(2): p. 95-108.

8. Shaw, T., et al., *Commonality of elastic relaxation times in biofilms.* Phys Rev Lett, 2004. **93**(9): p. 098102.

9. Greener, J., et al., *A microfluidic method and custom model for continuous, non-intrusive biofilm viscosity measurements under different nutrient conditions.* Biomicrofluidics, 2016. **10**: p. 064107.

10. Paquet-Mercier, F., et al., *Through thick and thin: a microfluidic approach for continuous measurements of biofilm viscosity and the effect of ionic strength.* Lab Chip, 2016. **16**(24): p. 4710-4717.

11. Klapper, I., et al., *Viscoelastic fluid description of bacterial biofilm material properties.* Biotechnology and bioengineering, 2002. **80**(3): p. 289-296.

12. Di Stefano, A., et al., *Viscoelastic properties of Staphylococcus aureus and Staphylococcus epidermidis mono-microbial biofilms.* Microb Biotechnol, 2009. **2**(6): p. 634-41.

13. Cense, A.W., et al., *Mechanical properties and failure of Streptococcus mutans biofilms, studied using a microindentation device.* J Microbiol Methods, 2006. **67**(3): p. 463-72.

14. Elodie Lahaye, et al., *Does Water Activity Rule P. mirabilis Periodic Swarming? II. Viscoelasticity and Water Balance during Swarming.* Biomacromolecules, 2007. **8**: p. 1228-1235.

15. Stoodley, P., et al., *Biofilm material properties as related to shear-induced deformation and detachment phenomena.* J Ind Microbiol Biotechnol, 2002. **29**(6): p. 361-7.

16. Peña, N., et al., *Evaluating impact of fouling on reverse osmosis membranes performance.* Desalination and Water Treatment, 2013. **51**(4-6): p. 958-968.

17. Nguyen, T., F.A. Roddick, and L. Fan, *Biofouling of water treatment membranes: a review of the underlying causes, monitoring techniques and control measures.* Membranes (Basel), 2012. **2**(4): p. 804-40.

18. H.-C. Flemming, et al., *Biofouling—the Achilles heel of membrane processes.* Desalination, 1997. **113**(2): p. 215-255.

19. Kerchove, A.J.D. and M. Elimelech, *Bacterial swimming motility enhances cell deposition and surface coverage.* Environ. Sci. Technol., 2008. **42**(12): p. 4371–4377.

20. Loosdrecht, M.C.v., et al., *The role of bacterial cell wall hydrophobicity in adhesion.* Appl. Environ. Microbiol., 1987. **53**(8): p. 1893–1897.

21. Jewett, D., et al., *Bacterial transport in laboratory columns and filters: influence of ionic strength and pH on collision efficiency.* Water Res., 1995. **29**(7): p. 1673–1680.

22. Torkzaban, S., et al., *Transport and fate of bacteria in porous media: Coupled effects of chemical conditions and pore space geometry.* Water Resources Research, 2008. **44**(4).

23. Bereschenko, L.A., et al., *Molecular characterization of the bacterial communities in the different compartments of a full-scale reverse-*

osmosis water purification plant. Appl Environ Microbiol, 2008. **74**(17): p. 5297-304.

24. Mayer, C., et al., *The role of intermolecular interactions: studies on model systems for bacterial biofilm.* Int.J.Biol.Macromol., 1999. **26**(1): p. 3-16.

25. Flemming, H.C., *Biofouling in water systems--cases, causes and countermeasures.* Appl Microbiol Biotechnol, 2002. **59**(6): p. 629-40.

26. Park, N., et al., *Biofouling potential of various NF membranes with respect to bacteria and their soluble microbial products (SMP): Characterizations, flux decline, and transport parameters.* Journal of Membrane Science, 2005. **258**(1-2): p. 43-54.

27. Herzberg, M. and M. Elimelech, *Biofouling of reverse osmosis membranes: Role of biofilm-enhanced osmotic pressure.* Journal of Membrane Science, 2007. **295**(1-2): p. 11-20.

28. Herzberg, M., S. Kang, and M. Elimelech, *Role of extracellular polymeric substances (EPS) in biofouling of reverse osmosis membranes.* Environ. Sci. Technol., 2009. **43**(12): p. 4393–4398.

29. Miura, Y., Y. Watanabe, and S. Okabe, *Membrane biofouling in pilot-scale membrane bioreactors (MBRs) treating municipal wastewater: Impact of biofilm formation.* Environ. Sci. Technol., 2007. **41**(2): p. 632–638.

30. Huang, L.N., H.D. Wever, and L. Diels, *Diverse and distinct bacterial communities induced biofilm fouling in membrane bioreactors operated under different conditions.* Environ. Sci. Technol., 2008. **42**(22): p. 8360–8366.

31. Barnes, R.J., et al., *Nitric oxide treatment for the control of reverse osmosis membrane biofouling.* Appl Environ Microbiol, 2015. **81**(7): p. 2515-24.

32. Matin, A., et al., *Biofouling in reverse osmosis membranes for seawater desalination: Phenomena and prevention.* Desalination, 2011. **281**: p. 1-16.

33. Heyderman, L.J., et al., *High volume fabrication of customised nanopore membrane chips.* Microelectronic Engineering, 2003. **67-68**: p. 208-213.

34. Srijanto, B.R., et al., *Nanostructured silicon membranes for control of molecular transport.* J Vac Sci Technol B Nanotechnol Microelectron, 2010. **28**(6): p. C6PC6P48-C6PC6P52.

35. Hassanpourfard, M., et al., *Bacterial floc mediated rapid streamer formation in creeping flows.* Sci Rep, 2015. **5**: p. 13070.

36. Das, S. and A. Kumar, *Formation and post-formation dynamics of bacterial biofilm streamers as highly viscous liquid jets.* Sci Rep, 2014. **4**: p. 7126.

37. Valiei, A., et al., *A web of streamers: biofilm formation in a porous microfluidic device.* Lab on a Chip, 2012. **12**(24): p. 5133.

38. Marty, A., et al., *Impact of tortuous flow on bacteria streamer development in microfluidic system during filtration.* Biomicrofluidics, 2014. **8**(1): p. 014105.

39. Marty, A., et al., *Formation of bacterial streamers during filtration in microfluidic systems.* Biofouling, 2012. **28**(6): p. 551-62.

40. Drescher, K., et al., *Biofilm streamers cause catastrophic disruption of flow with consequences for environmental and medical systems.* Proc Natl Acad Sci U S A, 2013. **110**(11): p. 4345-50.

41. Rusconi, R., et al., *Laminar flow around corners triggers the formation of biofilm streamers.* J R Soc Interface, 2010. **7**(50): p. 1293-9.

42. Rusconi, R., et al., *Secondary flow as a mechanism for the formation of biofilm streamers.* Biophys J, 2011. **100**(6): p. 1392-9.

43. Gashti, M.P., et al., *Live-streaming: Time-lapse video evidence of novel streamer formation mechanism and varying viscosity.* Biomicrofluidics, 2015. **9**(041101).

44. Mulder, M., *Basic Principles of Membrane Technology.* Springer, 2007. **Second edition**.

45. L. Vogelaar, J.N.B., C. J. M. van Rijn, W. Nijdam, and M. Wessling, *Phase Separation Micromolding—PSμM**.* Adv. Mater., 2003. **15**(16): p. 1385-1389.

46. Lalia, B.S., et al., *A review on membrane fabrication: Structure, properties and performance relationship.* Desalination, 2013. **326**: p. 77-95.

47. Freeman, A.S.a.B., *Fundamentals of Membranes for Water Treatment.* University of Texas at Austin: p. 1-17.

48. J. C. Mcdonald, D.C.D., J. R. Anderson, D. T. Chiu, H. Wu, O. J. A. Schueller, and G. M. Whitesides, *Review General Fabrication of microfluidic systems in poly (dimethylsiloxane).* Electrophoresis, 2000. **21**: p. 27-40.

49. M. Cabodi, N.W.C., J. P. Gleghorn, C. S. D. Lee, L. J. Bonassar, and A. D. Stroock, *A microfluidic biomaterial.* J. Am. Chem. Soc., 2005. **127**(40): p. 13788–13789.

50. Yu-Chuan, S., L. Liwei, and A.P. Pisano, *A water-powered osmotic microactuator.* Journal of Microelectromechanical Systems, 2002. **11**(6): p. 736-742.

51. Greener, J., et al., *Rapid, cost-efficient fabrication of microfluidic reactors in thermoplastic polymers by combining photolithography and hot embossing.* Lab Chip, 2010. **10**(4): p. 522-4.

52. Debono, M., et al., *One-Step Fabrication of Microchannels with Integrated Three Dimensional Features by Hot Intrusion Embossing.* Sensors (Basel), 2016. **16**(12).

53. Russo, A.P., et al., *Direct Casting of Polymer Membranes into Microfluidic Devices.* Separation Science and Technology, 2004. **39**(11): p. 2515-2530.

54. Ismagilov, R.F., et al., *Microfluidic Arrays of Fluid-Fluid Diffusional Contacts as Detection Elements and Combinatorial Tools.* Anal. Chem., 2001. **73**: p. 5207-5213.

55. Srigunapalan, S., et al., *A microfluidic membrane device to mimic critical components of the vascular microenvironment.* Biomicrofluidics, 2011. **5**(1): p. 13409.

56. Song, J.W., et al., *Microfluidic endothelium for studying the intravascular adhesion of metastatic breast cancer cells.* PLoS One, 2009. **4**(6): p. e5756.

57. Huh, D., et al., *Acoustically detectable cellular-level lung injury induced by fluid mechanical stresses in microfluidic airway systems.* Proc Natl Acad Sci U S A, 2007. **104**(48): p. 18886-91.

58. Huh, D., et al., *Reconstituting organ-level lung functions on a chip.* Science, 2010. **328**(5986): p. 1662-8.

59. Battin, T.J., et al., *The ecology and biogeochemistry of stream biofilms.* Nat. Rev. Microbiol., 2016. **14**(4): p. 251-263.

60. E. W. K. Young, M.W.L.W., S. Srigunapalan, A. R. Wheeler, and C. A. Simmons, *Technique for Real-Time Measurements of Endothelial*

Permeability in a Microfluidic Membrane Chip Using Laser-Induced Fluorescence Detection. Anal. Chem., 2010. **82**(1): p. 808-8016.

61. Kaufman, Y., et al., *Microfluidic NF/RO separation: Cell design, performance and application.* Journal of Membrane Science, 2012. **396**: p. 67-73.

62. Karnik, S.V., M.K. Hatalis, and M.V. Kothare, *Towards a palladium micro-membrane for the water gas shift reaction: microfabrication approach and hydrogen purification results.* Journal of Microelectromechanical Systems, 2003. **12**(1): p. 93-100.

63. Ookawara, S., T. Ishikawa, and K. Ogawa, *Applicability of a Miniaturized Micro-Separator/Classifier to Oil-Water Separation.* Chemical Engineering & Technology, 2007. **30**(3): p. 316-321.

64. Dong, T., et al., *A smart fully integrated micromachined separator with soft magnetic micro-pillar arrays for cell isolation.* Journal of Micromechanics and Microengineering, 2010. **20**(11): p. 115021.

65. Ngene, I.S., et al., *A microfluidic membrane chip for in situ fouling characterization.* Journal of Membrane Science, 2010. **346**(1): p. 202-207.

66. Hassanpourfard, M., et al., *Protocol for biofilm streamer formation in a microfluidic device with micro-pillars.* J Vis Exp, 2014(90).

67. Bacchin, P., et al., *Colloidal surface interactions and membrane fouling: investigations at pore scale.* Adv Colloid Interface Sci, 2011. **164**(1-2): p. 2-11.

68. Derekx, Q., et al., *Numerical and Experimental Study of Fouling in Microfluidic Channels and Microfiltration Membranes.* Procedia Engineering, 2012. **44**: p. 54-56.

69. Chueh, B.-h., et al., *Leakage-Free Bonding of Porous Membranes into Layered Microfluidic Array Systems.* Anal. Chem., 2007. **79**: p. 3504-3508.

70. Drescher, K., et al., *Biofilm streamers cause catastrophic disruption of flow with consequences for environmental and medical systems.* P. Natl. Acad. Sci. USA, 2013. **110**(11): p. 4345-4350.

71. Hassanpourfard, M., et al., *Bacterial floc mediated rapid streamer formation in creeping flows.* Sci. Rep., 2015. **5**: p. 13070.

72. J. Cooper McDonald and G.M. Whitesides, *Poly(dimethylsiloxane) as a material for fabricating microfluidic devices.* Accounts of Chemical Research, 2002. **35**(7): p. 491-499.

73. Liu, M., et al., *Thickness-dependent mechanical properties of polydimethylsiloxane membranes.* Journal of Micromechanics and Microengineering, 2009. **19**(3): p. 035028.

74. Workentine, M.L., et al., *Spatial distributions of Pseudomonas fluorescens colony variants in mixed-culture biofilms.* BMC Microbiol., 2013. **13**(1): p. 1-7.

75. S. Zuber, F.C., C. Keel, A. Mattart, C. Blumer, G. Pessi, C. Gigot-Bonnefoy, U. Schnider-Keel, S. Heeb, C. Reimmann, and D. Haas, *GacS sensor domains pertinent to the regulation of exoproduct formation and to the biocontrol potential of Pseudomonas fluorescens CHA0.* Mol. Plant. Microbe. Interact., 2003. **16**(7): p. 634-644.

76. Stoodley, P., et al., *Oscillation characteristics of biofilm streamers in turbulent flowing water as related to drag and pressure drop.* Biotechnol. Bioeng., 1998. **57**(5): p. 536-544.

77. Rusconi, R., et al., *Laminar flow around corners triggers the formation of biofilm streamers.* J. Roy. Soc. Interface, 2010. **7**(50): p. 1293-1299.

78. Houari, A., et al., *Rheology of biofilms formed at the surface of NF membranes in a drinking water production unit.* Biofouling, 2008. **24**(4): p. 235-240.

79. Kim, M.K., et al., *Filaments in curved streamlines: rapid formation of Staphylococcus aureus biofilm streamers.* New J. Phys., 2014. **16**.

80. Weaver, W.M., et al., *Fluid Flow Induces Biofilm Formation in Staphylococcus epidermidis Polysaccharide Intracellular Adhesin-Positive Clinical Isolates.* Appl. Environ. Microbiol., 2012. **78**(16): p. 5890-5896.

81. Das, S. and A. Kumar, *Formation and post-formation dynamics of bacterial biofilm streamers as highly viscous liquid jets.* Sci. Rep., 2014. **4**: p. 7126.

82. Gashti, M.P., et al., *Live-streaming: Time-lapse video evidence of novel streamer formation mechanism and varying viscosity.* Biomicrofluidics, 2015. **9**(4): p. 041101.

83. Rubinstein, M. and A.V. Dobrynin, *Solutions of associative polymers.* Trends Polym. Sci., 1997. **5**(6): p. 181-186.

84. Wilking, J.N., et al., *Biofilms as complex fluids.* MRS Bull., 2011. **36**(5): p. 385-391.

85. Tuson, H.H., et al., *Measuring the stiffness of bacterial cells from growth rates in hydrogels of tunable elasticity.* Mol. Microbiol., 2012. **84**(5): p. 874-891.

86. Tan, S., R.L. Sherman, and W.T. Ford, *Nanoscale compression of polymer microspheres by atomic force microscopy.* Langmuir, 2004. **20**(17): p. 7015-7020.

87. Gurtin, M.E., E. Fried, and L. Anand, *The Mechanics and Thermodynamics of Continua*. illustrated, reprint ed. 2010, New York: Cambridge University Press.

88. Shaw, T., et al., *Commonality of elastic relaxation times in biofilms.* Phys. Rev. Lett., 2004. **93**(9).

89. Drazin, P.G. and W.H. Reid, *Hydrodynamic stability*. 2004: Cambridge University Press.

90. Lubliner, J., *Plasticity Theory*. 1990, New York: Macmillan. 544.

91. Boyce, M.C. and E.M. Arruda, *Constitutive models of rubber elasticity: A review.* Rubber Chem. Technol., 2000. **73**(3): p. 504-523.

92. Horgan, C.O. and G. Saccomandi, *Constitutive modelling of rubber-like and biological materials with limiting chain extensibility.* Math. Mech. Solids, 2002. **7**(4): p. 353-371.

93. Horgan, C.O. and G. Saccomandi, *Phenomenological hyperelastic strain-stiffening constitutive models for rubber.* Rubber Chem. Technol., 2006. **79**(1): p. 152-169.

94. Hutchinson, J. and K. Neale, *Influence of strain-rate sensitivity on necking under uniaxial tension.* Acta Metall., 1977. **25**(8): p. 839-846.

95. Hutchinson, J. and H. Obrecht, *Tensile instabilities in strain-rate dependent materials.* Fracture, 1977. **1**: p. 101-116.

96. Love, A.E.H., *A Treatise on the Mathematical Theory of Elasticity*. Vol. 1. 2013: Cambridge University Press.

97. Nemat-Nasser, S., *Plasticity*. 2004, Cambridge: Cambridge University Press.

98. Hill, R., *The Mathematical Theory of Plasticity*. Vol. 11. 1998: Oxford University Press.

99. Maugin, G.A., *The Thermomechanics of Nonlinear Irreversible Behaviors*. 1999: World Scientific.

100. Maugin, G.A. and W. Muschik, *Thermodynamics with internal variables. Part I. General concepts.* J. Non-Equilib. Thermodyn., 1994. **19**: p. 217-249.

101. Batchelor, G., *Slender-body theory for particles of arbitrary cross-section in Stokes flow.* J. Fluid Mech., 1970. **44**(03): p. 419-440.

102. Holzapfel, G., *Nonlinear Solid Mechanics. A Continuum Approach for Engineering*. 2000: Wiley.

103. Gent, A.N., *A new constitutive relation for rubber.* Rubber Chemistry and Technology, 1996. **69**(1): p. 59-61.

104. Kilian, H.G., *Equation of State of Real Networks.* Polymer, 1981. **22**(2): p. 209-217.

105. Biswas, I., et al., *Nonlinear deformation and localized failure of bacterial streamers in creeping flows.* Sci Rep, 2016. **6**: p. 32204.

106. Hassanpourfard, M., et al., *Dynamics of bacterial streamers induced clogging in microfluidic devices.* Lab Chip, 2016. **16**(21): p. 4091-4096.

107. Rusconi, R., et al., *Secondary flow as a mechanism for the formation of biofilm streamers.* Biophys. J., 2011. **100**(6): p. 1392-1399.

108. Zhu, X.-K., *Review of fracture toughness test methods for ductile materials in low-constraint conditions.* International Journal of Pressure Vessels and Piping, 2016. **139-140**: p. 173-183.

109. Gaggar, S.K. and L.J. Broutman, *Strength and fracture properties of random fibre Polyester composites.* Fibre Science and Technology, 1976. **9**: p. 205-223.

110. Alves, L.M., *Fractal geometry concerned with stable and dynamic fracture mechanics.* Theoretical and Applied Fracture Mechanics, 2005. **44**(1): p. 44-57.

111. Gong, J.P., *Why are double network hydrogels so tough?* Soft Matter, 2010. **6**(12): p. 2583.

112. Haque, M.A., et al., *Lamellar Bilayers as Reversible Sacrificial Bonds To Toughen Hydrogel: Hysteresis, Self-Recovery, Fatigue Resistance, and Crack Blunting.* Macromolecules, 2011. **44**(22): p. 8916-8924.

113. Barai, P., A. Kumar, and P.P. Mukherjee, *Modeling of Mesoscale Variability in Biofilm Shear Behavior.* PLoS One, 2016. **11**(11): p. e0165593.

114. Nguyen, T., F.A. Roddick, and L. Fan, *Biofouling of water treatment membranes: a review of the underlying causes, monitoring techniques and control measures.* Membranes 2012. **2**(4): p. 804-840.

115. Baker, J.S. and L.Y. Dudley, *Biofouling in membrane systems - A review.* Desalination, 1998. **118**: p. 81-90.

116. Mulder, M., *Basic Principles of Membrane Technology.* Basic Principles of Membrane Technology, 1998. **72**(3): p. 564.

117. Flemming, H.C. and J. Wingender, *The biofilm matrix.* Nature Reviews Microbiology, 2010. **8**(9): p. 623-633.

118. Flemming, H.C., T.R. Neu, and D.J. Wozniak, *The EPS matrix: The "House of Biofilm cells".* Journal of Bacteriology, 2007. **189**(22): p. 7945-7947.

119. Y. Miura, Y.W., and S. Okabe, *Membrane biofouling in pilot-scale membrane bioreactors (MBRs) treating municipal wastewater: Impact of biofilm formation.* Environ. Sci. Technol., 2007. **41**(2): p. 632-638.

120. Guo, W., H.H. Ngo, and J. Li, *A mini-review on membrane fouling.* Bioresour Technol, 2012. **122**: p. 27-34.

121. de Jong, J., R.G. Lammertink, and M. Wessling, *Membranes and microfluidics: a review.* Lab Chip, 2006. **6**(9): p. 1125-39.

122. Roelofs, S.H., A. van den Berg, and M. Odijk, *Microfluidic desalination techniques and their potential applications.* Lab Chip, 2015. **15**(17): p. 3428-38.

123. Shao, G., et al., *Fabrication of elastomeric high-aspect-ratio microstructures using polydimethylsiloxane (PDMS) double casting technique.* Sensors and Actuators A: Physical, 2012. **178**: p. 230-236.

124. Perl, A., D.N. Reinhoudt, and J. Huskens, *Microcontact Printing: Limitations and Achievements.* Advanced Materials, 2009. **21**(22): p. 2257-2268.

125. Kung, Y.C., et al., *Fabrication of 3D high aspect ratio PDMS microfluidic networks with a hybrid stamp.* Lab Chip, 2015. **15**(8): p. 1861-8.

126. Babel, S. and S. Takizawa, *Microfiltration membrane fouling and cake behavior during algal filtration.* Desalination, 2010. **261**(1-2): p. 46-51.

127. Ho, C.C. and A.L. Zydney, *A Combined Pore Blockage and Cake Filtration Model for Protein Fouling during Microfiltration.* J Colloid Interface Sci, 2000. **232**(2): p. 389-399.

128. Hayatbakhsh, M., et al., *Treatment of anin situoil sands produced water by polymeric membranes.* Desalination and Water Treatment, 2015. **57**(32): p. 14869-14887.

129. Bart Van der Bruggen, et al., *A review of pressure-driven membrane processes in wastewater treatment and drinking water production.* Environmental Progress, 2003. **22**(1): p. 46-56.

130. Wang, Z., et al., *Membrane fouling in a submerged membrane bioreactor (MBR) under sub-critical flux operation: Membrane foulant and gel layer characterization.* Journal of Membrane Science, 2008. **325**(1): p. 238-244.

131. He, Z., et al., *The effect of permeate flux on membrane fouling during microfiltration of oily water.* Journal of Membrane Science, 2017. **525**: p. 25-34.

132. Khorshidi, B., et al., *Thermally resistant and electrically conductive PES/ITO nanocomposite membrane.* Journal of Membrane Science, 2016. **500**: p. 151-160.

133. Lijie Zhou. Siqing Xia, Z.Z., Biao Ye, Xiaoyin Xu, Zaoli Gu, and Xin Wang, *Effects of pH, Temperature and Salinity on Extracellular Polymeric Substances of Pseudomonasaeruginosa Biofilm with N-(3-Oxooxtanoyl)-L-Homoserine Lactone Addition* Journal of Water Sustainability, 2014. **4**(2): p. 90-100.

134. Xia, S., et al., *Influence and mechanism of N-(3-oxooxtanoyl)-L-homoserine lactone (C8-oxo-HSL) on biofilm behaviors at early stage.* Journal of Environmental Sciences, 2012. **24**(12): p. 2035-2040.

135. Stoodley, P., D. Debeer, and H.M. Lappin-Scott, *Influence of Electric Fields and pH on Biofilm Structure as Related to the Bioelectric Effect.* Antimicrobial Agents and Chemotheraphy, 1997. **41**(9): p. 1876-1879.

136. Dogsa, I., et al., *Structure of bacterial extracellular polymeric substances at different pH values as determined by SAXS.* Biophys J, 2005. **89**(4): p. 2711-20.

137. A. Hostacka, I. Čiznar, and M. Štefkovicova, *Temperature and pH affect the production of bacterial biofilm.* Folia Microbiol, 2010. **55**(1): p. 75-78.

138. Debnath, N., et al., *Abiotic streamers in a microfluidic system.* Soft Matter, 2017. **13**(46): p. 8698-8705.